CIENCIAS DEL MAR

PROGRAMA DE ESPECIALIZACIÓN
Y DOCTORADO

TESIS DOCTORAL

TITULO

Start of Sediment Motion and Resuspension in Turbulent Flows: Applications of Zero-Mean Flow Grid Stirred Turbulence on Sediment Studies.

AUTOR

Oc. Pablo Medina Enríquez

DIRECTOR

Dr. José Manuel Redondo

FECHA

17 de julio de 2002

TABLE OF CONTENTS

LIST OF FIGURES

LIST OF TABLES

Chapter 1

INTRODUCTION

Much work has been done in sediment transport processes during the past decades. However, the ability to predict the amount of sediment that is being transported in a certain time span at a given place is still very poor, this is especially true in the coastal areas. There are many parameters involved, and there is a complex interaction at the coastline between different sources of turbulence such as shear waves, tides and long shore currents. This is a very dynamic zone where atmosphere, sea and land processes, not to mention human activities, come together making it a very complex system.

There are problems even for the simplest, tidally dominated conditions, where predictions of sediment transport rates are found to differ by almost two orders of magnitude (Jones S.E., Jago C.F. and Simpson J.H., (1996), Redondo J.M., Sánchez M.A. and Castilla R. (1995), Sánchez and Redondo (1998)). Authors such as Dally and Dean (1984) feel this is the result of attempting to describe a very complex problem too simplistically, without first acquiring at least a qualitative understanding of all transport mechanisms involved. This statement made by Dally and Dean seems very reasonable, not only in this field, but in general. To study each of the mechanisms involved separately we undoubtedly require some abstraction and, also, to forget for a moment the real situation and go for a simple manageable mathematical model or for simple experimental approaches. This seems reasonable even admitting that it is often impossible to study one particular mechanism in isolation. Experimental data has to be related to field data, but all laboratory experiments whose purpose is to have a better understanding of one particular effect, have to deal sooner or later with how the experimental data explain the real complex problem.

An important mechanism involved in sediment transport is turbulence, perhaps one of the most important ones, but definitely the most complex one. Relations between turbulence and sediment characteristics are not well known. And, of course, the lack of

knowledge on how turbulent flows affect the overall sediment transport rate is of great concern. Other authors working with suspended particulate matter (SPM) (Jones, Jago and Simpson, 1996), used a best-fitting model output in their models to parameterize the entrainment from the seabed. They recognized the lack of knowledge that makes it impossible to incorporate the detailed mechanisms that control the entrainment in the model because both their qualitative and quantitative parameterization remains poorly understood.

Dynamical processes associated with the initial lift-off of sediments from the sea bottom in the benthic layer and the ways in which turbulence maintains the sediment in suspension are also poorly understood due to their complexity.

There are several possible experimental configurations to study the behaviour of sediment transport under the influence of a laminar flow that produces shear on the sediment layer surface, which in turn generates a turbulent layer near the sediment surface. Still, there are no experimental configurations where sediment transport could be studied under the influence of a fully developed turbulent flow with zero-mean flow. Well-known experimental configurations, designed to study stratified fluids under the action of a turbulent flow, have been used since 1955 (Rouse and Dodu). These configurations deserve a comprehensive study in order to analyse the possibilities of using them in the study of sediment transport, and to find out what aspects involved in this phenomena could be explored from this new perspective. This approach to the study of sediment motion, combined with techniques such as image analysis, will most likely set forth remarkable results that will end in an enhanced understanding of this complex phenomena.

The objectives of the thesis were, on the one hand, to test the possibilities of a well-known experimental configuration, used to study stratified fluids in turbulent flows with zero-mean flow, on the study of sediment transport, and to find out what aspects involved in this phenomena could be explored from this new perspective. We used this configuration because in many practical situations such as wave stirred sediments or benthic boundary layers the mean flow near the sediment layers is zero. On the other hand, we also wanted to compare a well-established criteria such as Shields parameter

with the local turbulent energy $k = \left(\frac{1}{2}\overline{u_{ii}'^2}\right)$ or the r.m.s. velocity[•] (u'), which is an appealing physically relevant parameter, as well as to compare the differences between zero-mean and sheared induced lift-off.

Since this application is not restricted to either coastal or benthic sediment transport, real sediments in the size range of clays to sands were used to test the possibilities of the experimental configuration under study.

Grid-stirred turbulence has been used since Rouse and Dodu (1955) to investigate stratified flows. But it was not until the late 80's that Tsai and Lick (1986) and Xuequan and Hopfinger (1987) first used grid-stirred turbulence to investigate sediment resuspension. Following the results obtained by these authors, Crespo and Redondo (1989) and Noh and Fernado (1991) investigated different aspects of sediment transport. The former modelled the head of a gravity current as a strong stirrer (grid) near the bottom of a tank, which maintains a near uniform concentration of sediments in suspension. They did this based on key experiments on sediment transport and turbidity currents performed by Middleton (1966), as well as experiments carried out by Xuequan and Hopfinger (1987) on a grid stirred sediment bed. The latter investigated the upward dispersion of heavy particles in suspension in a turbulent flow, and the formation of a suspension layer of depth *D*, with a well-defined lutocline separating the turbulent and nonturbulent layers, as set forth in the experiments of Xuequan and Hopfinger (1987). Lutoclines of this nature are often found in very turbid waters, such as shallow estuarine or coastal waters with un-consolidated mud at the bottom (Silvester and Hsu (1993)).

An intense and systematic calibration of the flow properties under different experimental configurations is lacking in all pervious works dealing with zero-mean grid-stirred turbulence and sediment transport, mainly between the source of energy input (oscillating grid) and the solid boundary (sediment bed). All of these experiments take for granted that the results obtained by other authors, who's main interest was to investigate the behaviour of a density front in a stratified fluid under the influence of a turbulent flow, could be directly applied to their experimental configurations. Therefore,

---

[•] Note: $u' = \sqrt{\frac{2}{3}k}$ in isotropic flows

we checked other aspects which were never dealt with before, such as: a) Measurements of the critical u' needed to initiate sediment motion or to start sediment lift-off; b) Comparison of classical measurements such as the Shields parameter with the critical u'; c) Comparative measurements of the sediment bed behaviour under the influence of a shear flow and under the influence of a zero-men turbulent flow; d) Estimates of the sediment flux and the sediment size (by means of the deposition speed), combining a grid-stirred experimental configuration with image analysis; e) Research regarding the sediment properties that play a major role in hampering sediment erosion. All of these are considered in the present work.

Much work has been done during the past decades in search of a qualitative and quantitative understanding of all transport mechanisms involved in the sediment transport phenomena. Many authors such as Zhixian (1997), Dally and Dean (1984) and Nielsen (1992), among others, agree on the fact that one of the basic impediments to a clear understanding of a variety of fundamental problems in the context of sediment transport has been the lack of a well-grounded formulation of bed sediment entrainment. They also agree that progress has been slower in the area of quantitative morphodynamic modelling. The reason is that the quantitative link between the main flow and the rate of morphological change has been missing. The required link consists of efficient models of the boundary layer flow and of the resulting sediment transport, which in turn requires a full understanding of all transport mechanisms. The research line presented in this work opens a new perspective in the sediment transport research field and, hopefully, will shed some light to those unsolved fundamental problems that hamper progress in different areas, such as quantitative morphodynamic modelling, as it is going to be set forth further on in this work.

The present work is divided in 7 chapters. After this first introductory chapter, comes a presentation, in Chapter 2, we present some general concepts of turbulence and sediment transport. The goal of this chapter is to give the reader a broad view of both areas not to be a fully contained course in these areas of knowledge, the idea is to allow specialists in one of these areas to have a general view of the other since this work deals simultaneously with two areas of knowledge. The objective of the present work is stated in Chapter 3, as well as the methods and techniques used. Chapter 4 presents detailed experimental configurations as well as experiments performed in order to acquire a

complete knowledge of the flow characteristics within the mixing boxes used. The results obtained are set forth as well. Once the flow in the different mixing boxes was well known, some experiments dealing with sediments were carried out to analyze the possibilities of the use of this method in the study of sediment motion initiation and lift-off (resuspension) as well as in the estimation of sediment flux. All experiments set forth here as well as the results obtained are given in detail in Chapter 5. Another experiment was designed to compare sediment transport under a shear flow and under a zero-mean flow. This experiment, and its corresponding results, is presented in Chapter 6. The conclusions of the present work are given in Chapter 7.

Chapter 2

GENERAL CONCEPTS

The goal of this chapter is not to be a fully contained course in these areas of knowledge, namely sediment transport and turbulence structure. Instead, it gives the reader a broad view of both areas. The idea of this is to allow specialists in one of this areas to have a general view of the other, since this work deals simultaneously with two areas of knowledge. This chapter is based on general as on specific texts such as Kundu (1990), Tennekes and Lumly (1990), Fernando (1989), Sánchez and Redondo (1998), Nielsen (1992), Linden (1972) and Thomson and Turner (1975) among others. The former are not explicitly cited in the text.

2.1 Sediment Transport

For the purpose of sediment transport modeling, three basic types of forces which govern the behaviour of cohesionless sediment particles must be consider whether they are resting at the bed or moving around in a slurry or a thin suspension. These are: the gravity force $F_g = M\,g$, intergranular forces related to collisions or continuous contact; and the fluid forces which may be due to surface drag or fluid pressures.

The intergranular forces are well understood as far as resting (non-shearing) grains are concerned. The static angle of repose φ_s for resting grains is determined by the frictional coefficient, i.e. the ratio between the effective normal stress s_e and the maximum sustainable shear stress t_{max} (Figure 2-1).

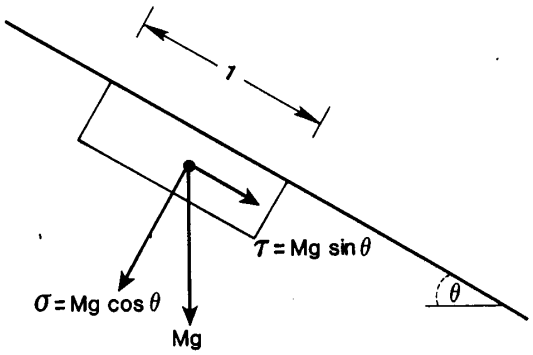

Figure 2-1.- The frictional coefficient $\left(t/s_e\right)_{\max}$ equals tan φ_s, where φ_s is the static angle of repose.

The angle φ_s applies to dry sand or to sand which is entirely under water. Sand which is wet but not saturated may stand at a much steeper angle because the negative pore water pressure increases the effective normal stress s_e.

For most sandy materials the static angle of repose is between 26 and 34 degrees, being greatest when the material is most densely packed. Regarding moving (shearing) materials of near maximum concentration, the frictional coefficient, hence the dynamical angle of repose, φ_d is of similar magnitude to φ_s. Hanes and Inman (1985) suggested a typical value of 31 degrees for beach sand.

When a horizontal sand bed is exposed to a fast, steady flow, a finite top layer of sand will start to move with the flow, partly a bed-load and partly in suspension. The fact that the moving layer is of finite thickness is significant although seemingly trivial, because it sets forth the fact that the moving sand has increased the strength of the sand below.

Since shear stress is not decreasing downward, the top layer of immobile sand is able to withstand shear stress which eroded the top layers when the flow was started. This is due to the fact that the moving sand is transferring at least part of its weight to the bed as effective stress and thereby increasing the effective normal stress in the bed. The effective normal stress transferred by the moving sand is generally referred to as dispersive stress.

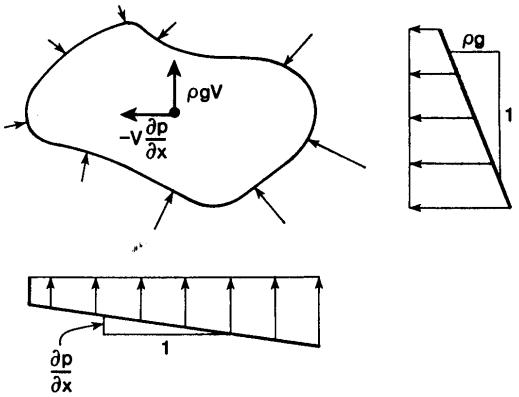

Figure 2-2.- The total pressure force is, by Green's theorem, equal to the volume times the pressure gradient when the pressure gradient can be considered constant over the body.

There are two kinds of fluid forces on sediment. Namely, surface drag forces and pressure forces resulting from pressure gradients in the fluid. The total pressure force which is determined as the surface integral of the pressure is, by Green's theorem, equal to minus the volume integral of the pressure gradient, $\nabla p = \left(\frac{\partial p}{\partial x}, \frac{\partial p}{\partial z} \right)$. Hence, for the situation in Figure 2-2 where the pressure along a vertical is hydrostatic and there is a constant horizontal pressure gradient, the total pressure force on the body is

$$F_p = \begin{pmatrix} -V\dfrac{\partial p}{\partial x} \\ -V\dfrac{\partial p}{\partial z} \end{pmatrix} = \begin{pmatrix} -V\dfrac{\partial p}{\partial x} \\ r\,gV \end{pmatrix} \tag{2-1}$$

where the vertical component is the familiar buoyancy force corresponding to $\partial p/\partial z = -r\,g$. V is the particle volume.

Drag forces occur in two varieties: skin friction and form drag. Skin friction contributes most of the drag on slender, streamlined bodies such as kayaks, while form drag is predominant on plump forms like spheres and most sediment grains. Drag force is normally given in the form

$$F_D = \frac{1}{2}\, r\, A C_D |u| u \tag{2-2}$$

where A ($\approx p\, d^2/4$) is the cross sectional area facing the flow, and C_D is the drag coefficient which depends on the sediment shape and on the Reynolds number, $d|u|/n$. When the flow becomes laminar the drag force is actually proportional to the flow velocity and, for small ($d|u|/n$ <1) spherical particles, the drag force is given by the Stokes' law

$$F_D = 3p\ r n\, d u \tag{2-3}$$

which corresponds to a drag coefficient of

$$C_D = \frac{24}{d|u|/n} \tag{2-4}$$

On average, a sand particle in a sand flat bed will have to carry a drag force of magnitude $t_0 d^2$ but the instantaneous force experienced by individual particles will be highly variable because no two particles will be equally exposed to the flow and because the flow at any point of the bed constantly changes with the formation of high velocity streaks and low velocity streaks.

A particle on the bed will also experience a lift force F_L due to the curvature of the stream lines of the flow over the top of it. Similarly to the forces on a stone on a string which is Mu^2/r , the lift force is also proportional to the square of the fluid velocity and inversely proportional to the orbit radius which in this case is of the order of d. Therefore, the force of the sediment particle with volume of the order d^3 is

$$F_L = r\ C_L \frac{u^2}{d} d^3 = r\ C_L u^2 d^2 \tag{2-5}$$

Sediment Mobility and Incipient Motion

The initiation of sediment motion under steady flows and under waves has attracted considerable interest in the past because it is a philosophically appealing concept. In practical terms, however, it is a very difficult concept to deal with. Firstly, because “initiation of motion” is difficult to define . Is it when one in a thousand grains moves or when one in a hundred moves? Secondly, because the complicating variables in a natural situation are very large. For example, the sand bed never remains perfectly smooth after a previous event. Relict bed forms will be present and initiation of motion will occur sooner near the crest of these bedforms due to local enhancement of the bed shear stress.

In addition, biological activity will also complicate the micro-topography and excretions from animals may tend to glue the sand particles together. Nevertheless, in what follows we shall consider a few classical approaches to the description of incipient sediment motion.

The Mobility Number

The mobility number Ψ, a simple, yet useful dimensionless measure of the fluid forces on a sediment particle under waves, will be defined.

For sand size particles (d~0.2 mm) under waves with typical semi-excursions, A, of the order 0.1 m - 2m, the Keulegan Carpenter number dlA is very small and hence the drag force will tend to dominate over the pressure force.

Hence, the total disturbing force on a sand particle at the bed is approximately proportional to the square of the velocity amplitude Aw, and the ratio between this disturbing force and the stabilizing force due to gravity is reasonably described by the mobility number

$$\Psi = \frac{(Aw)^2}{(s-1)gd} \tag{2-6}$$

The Shields Parameter

A different measure of the balance between disturbing and stabilizing forces on sand grains at the bed was suggested by Shields (1936) in a study on incipient sediment motion in steady flow,

$$q = \frac{t_{(0)}}{r\,(s-1)\,gd} = \frac{u_*^2}{(s-1)\,gd} \tag{2-7}$$

Accordingly, q is known as the Shields parameter.

It is particularly convenient to use this parameter in connection with steady flow because there, the steady bed shear stress, $\bar{t}_{(0)}$ and hence the friction velocity $\bar{u}_*$ are quantities which are easily measured, $\bar{t}_{(0)} = r\,gDI$, where D is the flow depth and I is the hydraulic gradient.

In connection with wave motion, the Shields parameter (corresponding to total stress) is generally defined in terms of the peak bed shear stress $\hat{t}$

$$q = \frac{\hat{t}}{r\,(s-1)\,g\,d} = \frac{\frac{1}{2}\,fw\,(Aw)^2}{(s-1)\,g\,d} = \frac{1}{2}\,fw\,\Psi \tag{2-8}$$

where fw is the wave friction factor.

Skin Friction

The total bed shear stress t may be seen as consisting of two contributions namely, the form drag t'' and the skin friction t'. The significance of each of these for sediment transport is quite different from that described by Engelund & Hansen (1972).

The form drag is generated by the difference in pressures between the upstream and the downstream sides of bedforms, and it does not directly affect the stability of individual surface sediment particles. The main disturbing influence to the surface

grains is generally considered to come from the skin friction t'. The corresponding skin friction Shields parameter,

$$q' = \frac{t'}{r\,(s-1)\,g\,d} \tag{2-9}$$

is therefore frequently used to predict initiation of motion and the magnitude of moving sediment concentrations.

Correspondingly, t' is often referred to as *effective stress* in connection with sediment transport. If the bed is flat, the form drag is absent, therefore, from that point of view, $t' = t$ and $q' = q$.

The Grain Roughness Shields Parameter

Flat beds of loose sand under waves as well as under steady flow may offer considerably more resistance to the flow than sand paper with the same grain size. This is a consequence of the momentum transfer by the moving sand from the flow to the bed.

It is, however, difficult to estimate this momentum transfer and the amount of related data is very limited. Therefore, a generally accepted method for calculating the skin friction on a bed of highly mobile sand under waves is not yet available.

On the other hand, the mobility number Ψ is not a totally adequate measure of the sediment mobility because it disregards the dependence on the radio *d/A* of the force exerted by waves on sediment particles.

Madsen & Grant (1976) therefore suggested that the sediment mobility be estimated in terms of grain roughness Shields parameter, and this approach has since been quite popular.

Following Engelund & Hansen (1972) and Nielsen (1979), we shall adopt the value $2.5d_{50}$ for the grain roughness of a flat bed of sand with median size d_{50}, and correspondingly operate with a grain roughness Shields parameter, $q_{2.5}$, defined by

$$q_{2.5} = \frac{\frac{1}{2} f_{2.5}\, r\,(Aw)^2}{r\,(s-1)\,g\,d} = \frac{1}{2} f_{2.5}\,\Psi \qquad (2\text{-}10)$$

where the special grain roughness friction factor, $f_{2.5}$ is based on Swart's (1974) formula and a roughness of $2.5d_{50}$

$$f_{2.5} = \exp\left[5.213\left(\frac{2.5d_{50}}{A}\right)^{0.194} - 5.977\right] \qquad (2\text{-}11)$$

The Critical Shields Parameter and the Shields Diagram

The *Critical Shields Parameter*, q_{cr}, is the effective Shields parameter (q') at which sediment movement starts. The value of q_{cr} is a function of the sediment size and density of the fluid density and viscosity, and of the flow structure. Typical q_{cr} values for sand in water are of the order 0.05. For sand in air, they are somewhat lower, usually in the range 0.01 <q_{cr} <0.02. In both air and water, q_{cr} becomes much larger in the silt range of grain sizes (d<0.OO3mm).

The effective shear stress t_{cr} which corresponds to q_{cr} [$t_{cr} = r\,(s-1)\,gdq_{cr}$] is called the *critical shear stress* for the particular sediment.

The Shields criterion, $q_{cr} = q_{cr}\left(u_* d/n\right)$, is but one of many criteria for the initiation of sediment motion. Many others have been suggested.

The Depth of Closure

A related concept to the initiation of motion is the depth of closure on a beach profile. The depth of closure is the depth beyond which sand level changes between seasonal surveys become unmeasurable or insignificant.

Practical estimates of the depth of closure are of the order 3.5 times the annual maximum significant wave height.

Total Sediment Load

The total load of moving sediment is generally seen as composed of three parts: the wash-load, the suspended load and the bed load.

The bed-load has been defined in different ways depending on the context. In relation to measurements, it is often defined as that part of the total load which travels below a certain level or (very pragmatically) as the part which gets caught in bed-load traps. However, for modeling purposes, it is more convenient to apply the definition of Bagnold (1956).

Bagnold defines the bed-load as that part of the total load which is supported by intergranular forces. The remaining loads, that is, the suspended load and the wash load, are supported by fluid drag.

Obviously a given grain may well be supported partly by intergranular forces and partly by fluid drag and hence contribute to both the suspended load and the bed-load. This makes the bed-load practically unmeasureable in situations where suspension is present as well, and this is, of course, of some concern.

The wash load is considered as part of the suspended load. It consists of the fine sediment which is not in equilibrium with sediment in the local bed because the capacity of the flow to entrain these fine particles exceeds their settling rate at the bed.

The Settling Velocity

By the sediment settling velocity, w_0, we understand the terminal velocity of a single sediment particle which settles through an extended, resting fluid. In that situation the fluid drag on the particle balances exactly the force of gravity. For a spherical particle with relative density, *s*, and diameter, *d*, this can be expressed by

$$\frac{1}{2} r \frac{p}{4} d^2 C_D w_0^2 = r (s-1) \frac{p}{6} d^3 g \tag{2-12}$$

which corresponds to

$$w_0 = \sqrt{\frac{4(s-1)gd}{3C_D}} \tag{2-13}$$

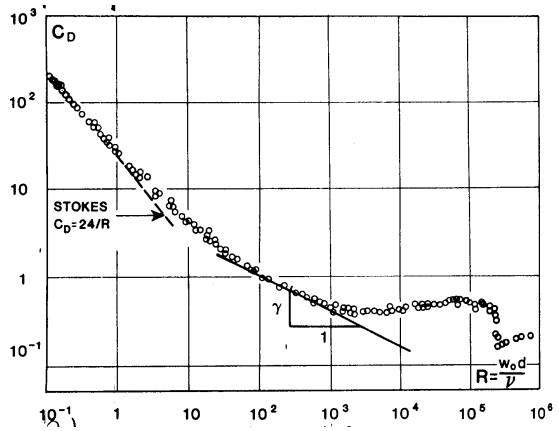

Figure 2-3.- Drag coefficients for spherical particles.

The drag coefficient C_D is a function of the particle Reynolds number $R = w_0 d/n$ and of the particle shape. The relationship for spherical particles is shown in Figure 2-3. The inclined asymptote

$$C_D = \frac{24}{w_0 d/n} \tag{2-14}$$

corresponds to the linear drag law, Stokes law

$$F_D = 3p\ r n\ d\ w_0 \tag{2-15}$$

which applies for very low Reynolds numbers.

Balancing the linear drag force given by equation (2-15) with gravity leads to the alternative expression

$$w_0 = \frac{(s-1)gd^2}{18n} \tag{2-16}$$

which is valid for very small ($R = w_0\, d/n$ <1) spherical particles.

Gibbs, Mathews and Link (1971) provided the following empirical formula for $w_0(d)$

$$w_0 = \frac{-3n + \sqrt{9n^2 + gd^2(s-1)(0.003869 + 0.02480d)}}{0.011607 + 0.07440d} \tag{2-17}$$

where w_o is measured in $^{cm}/_{s}$, d in cm, and the viscosity v in $^{cm^2}/_{s}$. This formula is applicable for spheres in water for the diameter range [0.0063cm; 1.0cm].

Natural sand particles are of course not spherical, but more or less angular or even disc shaped in the case of shell hash. For such natural grain shapes the formula (2-17) should represent the upper limit for the settling velocity as function of size.

Many particles which settle together in a thick suspension will settle somewhat slower than single particles if the suspension is homogeneous. This is due to the fact, that the downward motion of one sediment particle will generate a compensating upward flow elsewhere, which will delay the downward motion of the sediment particles.

On the other hand, a dense cloud of sediment in an otherwise clear fluid will settle faster than the typical settling velocity of the individual particles.

Equation of Motion for Suspended Particles

Consider a quasi-spherical particle with diameter *d* and relative density *s* which moves under the action of gravity and pressure gradients and drag from the surrounding fluid.

We neglect the history term of Basset (1888) which accounts for changes in the fluid drag due to changes in the flow structure around the particle, and neglect any effects of the particles rotation such as the Magnus effect (Magnus 1853).

With those simplifications applied, the equation of motion reads

$$\begin{aligned} \rho s \frac{\pi}{6} d^3 \frac{du_s}{dt} = \rho s \frac{\pi}{6} d^3 g - \frac{\pi}{6} \nabla p + \frac{1}{2} \rho \frac{\pi}{4} d^2 C_D' \left| u - u_s \right| (u - u_s) \\ + \frac{\pi}{6} \rho d^3 C_M \frac{d}{dt} (u - u_s) \end{aligned} \tag{2-18}$$

The variable drag coefficient C_D' is defined by

$$\frac{C_D'}{C_D} = \left(\frac{|u_s - u|}{w_0} \right)^{-g} \tag{2-19}$$

in accordance with the variation of C_D with changing particle Reynolds number (Figure 2-3).

From Figure 2-3, we see that $g = 1$ for small particles which move in accordance with Stokes Law, and $g = 0$ for large particles which settle under fully developed turbulent conditions.

The last term in equation (2-18) corresponds to fluid pressure on the added hydrodynamic mass, and the coefficient C_M may be assumed to have a value close to 0.5 which is the theoretical C_M-*value* for a sphere.

By introducing the pressure gradient vector in the form $\nabla p = r\,g - r\,du/dt$ and rearranging terms; writing equation in terms of the relative sediment particle velocity $u_r = u_s - u$ and with $a = (s-1)/(s + C_M)$ we get

$$\frac{du_r}{dt} + \frac{3}{4}\frac{C_D'}{d(s + C_M)} u_r \, \mathrm{u_r} = a\,g - a\,\frac{du}{dt} \tag{2-20}$$

Eliminating the drag coefficient C_D' from this equation, applying the definition of C_D equation (2-12), which gives

$$\frac{3}{4}\frac{C_D}{d} = \frac{(s-1)\,g}{w_0^2} \tag{2-21}$$

and the definition, equation (2-19), of C_D'. By inserting these into equation (2-20) we find that

$$\frac{du_r}{dt} + a\,g\left(\frac{u_r}{w_0}\right)^{1-g} \frac{u_r}{w_0} + u_r \bullet \nabla u = a\,g - a\,\frac{du}{dt} \tag{2-22}$$

The nature of the solutions is found to depend in a very important way on the third term $u_r \bullet \nabla u$, which, in essence, represents the effect of the small scale flow structure.

This term is negligible in a pure wave motion (for $w_0 T / L \ll 1$), and this is why a pure wave motion has very little effect on the sediment settling rate. On the other hand, the term $u_r \bullet \nabla u$ is very significant, for a sediment particle inside a vortex with diameter of the order of ten centimetres, and it provides the vortex trapping mechanism.

Equation (2-22) is linear for $g = 1$, and an exact analytical solution is therefore possible for small particles for which $g = 1$.

Particles Settling Through Turbulence

In order to understand sediment suspension in turbulent flows it is first necessary to analyse the influence of turbulence on a single particle which is settling through it.

Consider an ensemble of many identical particles which are dropped into a water filled jar where a certain level of turbulence is maintained by some kind of stirring (Figure 2-4).

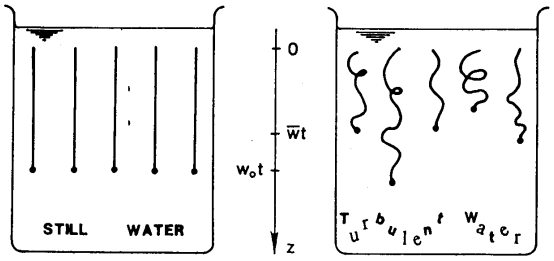

Figure 2-4.- Sediment particles settling through turbulent water will, on the average, settle more slowly than they would through still water.

The distances L_i, which the particles settle during the interval t, are measured and the corresponding time averaged velocities $w_i = L_i / t$ are calculated. It may then be observed that the ensemble average $\bar{w}_i$ is less than the still water settling velocity $\bar{w}_i < w_0$, and the variance $Var\{w_i\}$ is roughly proportional to: the turbulence intensity $\overline{w^2}$; to the Lagrangian integral scale of the turbulence T_L; and to l/t. That is

$$Var\{w_i\} \propto \overline{w^2}\, T_L / t \qquad \text{for} \quad t > T_L \tag{2-23}$$

The Loitering Effect

It is important to note that the settling delay described above does not require a specific, highly organized vortex structure. Trapping by vortices is just one manifestation of the general "Loitering Effect" which is illustrated in Figure 2-5.

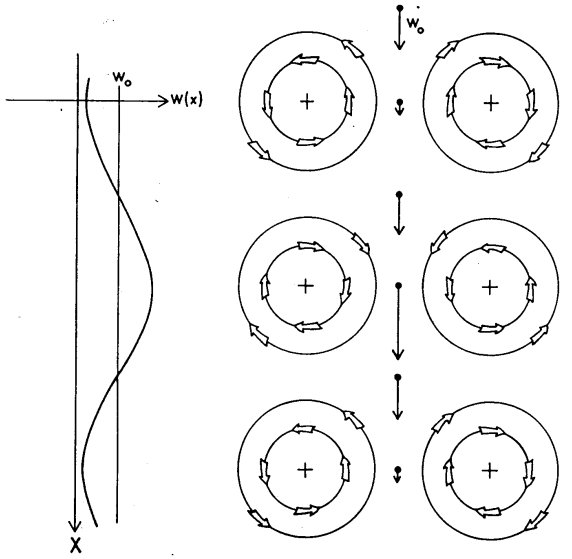

Figure 2-5.- A sediment particle which settles through this arrangement of vortices will experience a considerable delay compared with settling through still water because it spends more time in the upward moving parts of the fluid than in the downward moving parts.

The term "Loitering effect" refers to the fact that a settling or rising particle in a steady, non-uniform flow field will spend relatively more time (loiter) in those parts of the flow which move against their natural settling/rising velocity. By this mechanism, a non-uniform flow field with zero spatial mean velocity ($< u >= 0$) will delay the settling of sediment particles and the rising of air bubbles.

To quantify the effect, consider the special flow pattern in Figure 2-5. When the maximum upward water velocity along the symmetry line in Figure 2-5 exceeds w_0 there will be positions where $u + w_0 = 0$ at which the particle will stop and could be trapped forever.

In practice, the time limit for trapping is set by the typical lifetime of local flow structures T_E which is called the Eulerian time scale for turbulence.

2.2 Turbulence

Turbulence is a phenomenon that can be found anywhere, from the stirring of a coffee cup to the wind in the atmosphere. Most flows occurring in nature and in engineering applications are turbulent. The water currents below the surface of the oceans are turbulent; the Gulf Stream is a turbulent wall-jet kind of flow. The boundary layer in the earth's atmosphere is turbulent; jet streams in the upper troposphere are turbulent; cumulus clouds are in turbulent motion. Boundary layers growing on aircraft wings are turbulent. Most combustion processes involve turbulence and often even depend on it. The flow of water in rivers and canals is turbulent; the wakes of ships, cars, submarines and air crafts are in turbulent motion.

The study of turbulence clearly is an interdisciplinary activity, which has a very wide range of applications. In fluid dynamics laminar flow is the exception, not the rule: one must have small dimensions and high viscosities to encounter laminar flow. Turbulence is not a feature of fluids but of fluid flows. Most of the dynamics of turbulence is the same in all fluids, whether they are liquids or gases, if the Reynolds number of the turbulence is large enough; the mayor characteristics of turbulent flows are not controlled by the molecular properties of the fluid in which the turbulence occurred. It is very difficult to give a precise definition of turbulence. Usually, the question if a flow is turbulent is answered with the help of a few characteristics of turbulence, as described by Tennekes and Lumly (1990). These are:

Irregularity, or randomness: Turbulent flows seem irregular, chaotic and unpredictable. This makes a deterministic approach to turbulence problems impossible; instead one relies on statistical methods.

Nonlinearity: Turbulent flows are highly nonlinear.

Diffusivity: Due to the macroscopic mixing of fluid particles, turbulent flows are characterized by a rapid rate of diffusion of momentum, heat and mass transfer.

Vorticity: Turbulence is characterized by high levels of fluctuating vorticity. The identifiable structures in a turbulent flow are vaguely called eddies. A turbulence characteristic feature is the existence of an enormous range of eddy sizes. The large eddy has the size of order of the width of the region of turbulent flow; in a boundary

layer this is the thickness of the layer. The large eddy contains most of the energy. The energy is handed down from large to small eddies by nonlinear interactions, until it is dissipated by viscous diffusion in the smallest eddies, whose size is of the order of millimetres.

Dissipation: Turbulent flows are always dissipative. Viscous shear stresses perform work which increases the internal energy of the fluid at the expense of kinetic energy of the turbulence. Turbulence needs a continuous supply of energy to make up for this viscous loss. If no energy is supplied, turbulence decays rapidly. The mayor difference between random waves and turbulence is that waves are nondissipative (though they are often dispersive), while turbulence is essentially dissipative.

Reynolds Number

This dimensionless number is one of the principal parameters controlling the turbulence, and is given as

$$Re = \frac{L \cdot U}{n} \tag{2-24}$$

where n is the kinematic viscosity, L is the integral length-scale and U is the large-scale velocity. These last two properties are directly related to the geometry of the flow. Equation (2-24) states that if the velocity and size of the flow are large enough, the flow will be turbulent.

Turbulence has enjoyed an increasing interest the last few decades. This can be attributed to the fact that mathematics and physics of turbulence are as yet unsolved problems. Although the Navier-Stokes equations that govern turbulence are known, there are only n-1 equations to deal with n unknown quantities. Therefore a turbulence-model is needed, in order to introduce this last equation. There are many models that describe some types of turbulence very well, but there is no universal one. Furthermore, up until recently the complexity of turbulence made computation almost impossible at large Reynolds numbers. With the rapidly increasing power of computers however, the possibilities of turbulence computation are continuously rising. Together with

simulation, experimental research into the structure of turbulence is of fundamental importance. It offers the possibility to refine and verify the models used to describe turbulence.

The most famous theory for locally homogeneous, isotropic and stationary turbulence dates from 1941, when Kolmogorov introduced his K41 theory. This was based on the Richardson's idea of an energy cascade, represented graphically in Figure 2-6.

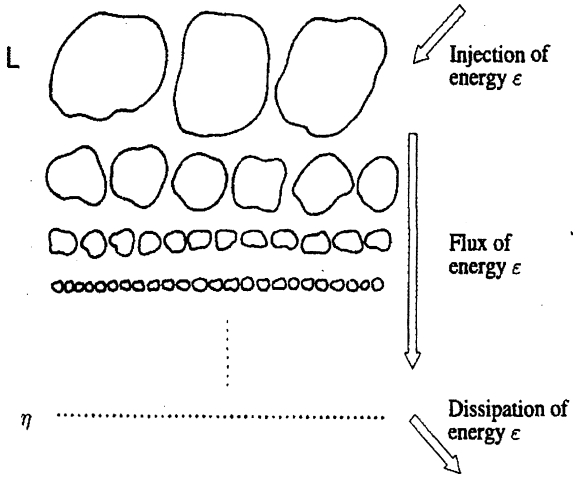

Figure 2-6.- Energy cascade process according to Richardson.

An energy cascade means that energy is injected into the large vortices. These large vortices break up into smaller ones, and thus the energy of the large scales is lost. This process continues until it reaches the very small scales, where the vortices can no longer brake up. At this smallest scale, the Kolmogorov scale (h), the energy is dissipated through viscosity.

Kolmogorov introduced the assumption that the small-scale structures, where the typical length-scale l is much smaller than the integral scale L, were isotropic and universal, and therefore only dependent on the dissipation $<e>$ and viscosity n. At the largest scales the typical values are the integral scale L and u', the root-mean-square velocity.

It can be demonstrated that, if these assumptions are correct, in the region where l is larger than the Kolmogorov scale h, but smaller than integral scale L, there must be a logarithmic profile. The density of turbulent energy per unit mass then follows the relation

$$E(l) = C_1 < e >^{2/3} l^{2/3} \tag{2-25}$$

and for its spectral equivalent

$$E(k) = C_2 < e >^{2/3} k^{-5/3} \tag{2-26}$$

Here C_1 and C_2 are universal constants, l is in the inertial sub-range and $k = 2\pi / l$ is the corresponding wave number. The constant C_2 has been measured over a wide range of Reynolds numbers to be 0.5 ± 0.05.

In flows that are originally laminar, turbulence arises from instabilities at large Reynolds numbers. Laminar pipe flow becomes turbulent at a Reynolds number (based on mean velocity and diameter) in the neighbourhood of 2,000 unless great care is taken to avoid creating small disturbances that might trigger transition from laminar to turbulent flow. Boundary layers in zero pressure gradients become unstable at a Reynolds number $Ud^*/n = 600$ approximately (d^* is the displacement thickness, U is the free-stream velocity, and v is the kinematic viscosity). Free shear flows, such as the flow in a mixing layer, become unstable at very low Reynolds numbers because of an inviscid instability mechanism that does not operate in boundary-layer and pipe flow. Early stages of transition can easily be seen in the smoke rising from a cigarette.

On the other hand, turbulence cannot maintain itself but depends on its environment to obtain energy. A common source of energy for turbulent velocity fluctuations is shear in the mean flow; other sources, such as buoyancy, exist too. Turbulent flows are generally shear flows. If turbulence arrives in an environment where there is no shear or other maintenance mechanism, it decays: the Reynolds number decreases and the flow tends to become laminar again. The classic example is turbulence produced by a grid in uniform flow in a wind tunnel.

Another way to make a turbulent flow laminar or to prevent a laminar flow from becoming turbulent is to provide for a mechanism that consumes turbulent kinetic energy. This situation prevails in turbulent flows with imposed magnetic fields at low magnetic Reynolds numbers and in atmospheric flows with a stable density stratification, to cite two examples.

Mathematically, the details of transition from laminar to turbulent flow are rather poorly understood. Much of the theory of instabilities in laminar flows is linearized theory, valid for very small disturbances; it cannot deal with the large fluctuation levels in turbulent flow. On the other hand, almost all of the theory of turbulent flow is asymptotic theory, fairly accurate at very high Reynolds numbers but inaccurate and incomplete for Reynolds numbers at which the turbulence cannot maintain itself. A noteworthy exception is the theory of the late stage of decay of wind-tunnel turbulence (Batchelor, 1953).

Experiments have shown that transition is commonly initiated by a primary instability mechanism, which in simple cases is two dimensional. The primary instability produces secondary motions, which are generally three-dimensional and become unstable themselves. A sequence of this nature generates intense localized three-dimensional disturbances (turbulent "spots"), which arise at random positions at random times. These spots grow rapidly and merge with each other when they become large and numerous to form a field of developed turbulent flow. In other cases, turbulence originates from an instability that causes vortices which subsequently become unstable. Many wake flows become turbulent in this way.

The Reynolds Decomposition and Equations

The velocity $\tilde{u}_i$ is decomposed in to a mean flow U_i and velocity fluctuations u_i (often described as u_i'), such that

$$\tilde{u}_i = U_i + u_i \tag{2-27}$$

U_i is interpreted as a time average, defined by

$$U_i = \lim_{T\to\infty} \frac{1}{t} \int_{t_0}^{t_0-T} \tilde{u}_i dt \tag{2-28}$$

Time averages (mean values) of fluctuations and of their derivatives, products and other combinations are denoted by an over bar. The mean values of a fluctuating quantity itself is zero by definition:

$$\overline{u_i} = \lim_{T\to\infty} \frac{1}{t} \int_{t_0}^{t_0+T} (\tilde{u}_i - U_i)\, dt \equiv 0 \tag{2-29}$$

The use of time averages corresponds to the typical laboratory situation, in which measurements are taken at fixed locations in a statistically steady, but often inhomogeneous, flow field. In an inhomogeneous flow, a time average like U_i is a function of position, so that the use of a spatial average would be inappropriate for most purposes. For a time average to make sense, the integrals in (2-28) and (2-29) have to be independent of t_0. In other words, the mean flow has to be steady:

$$\frac{\partial U_i}{\partial t} = 0 \tag{2-30}$$

Without this constraint (2-28) and (2-29) would be meaningless. The averaging time *T* needed to measure mean values depends on the accuracy desired.

The mean value of a spatial derivative of a variable is equal to the corresponding spatial derivative of the mean value of that variable; for example,

$$\frac{\partial \overline{\tilde{u}_i}}{\partial x_j} = \frac{\partial U_i}{\partial x_j} \quad , \quad \frac{\partial \overline{u_i}}{\partial x_j} = \frac{\partial}{\partial x_j} \overline{u_i} = 0 \tag{2-31}$$

These operations can be performed because averaging is carried out by integrating over a long period of time, which commutes with differentiation with respect to another independent variable.

The pressure $\tilde{p}$ and the stress $\tilde{s}_{ij}$ are also decomposed into mean and fluctuating components. Specifically,

$$\tilde{p} = P + p \quad , \quad \overline{p} \equiv 0 \tag{2-32}$$

$$\tilde{s}_{ij} = \Sigma_{ij} + s_{ij} \tag{2-33}$$

Like U_i, P and Σ_{ij} are independent of time. The mean stress tensor Σ_{ij} is given by

$$\Sigma_{ij} = -P\delta_{ij} + 2\mu S_{ij} \tag{2-34}$$

and the stress fluctuations s_{ij} are given by

$$s_{ij} = -p\delta_{ij} + 2\mu s_{ij} \tag{2-35}$$

Here, the mean strain rate S_{ij} and the strain-rate fluctuations s_{ij} are defined by

$$S_{ij} = \frac{1}{2}\left(\frac{\partial U_i}{\partial x_j} + \frac{\partial U_j}{\partial x_i} \right) \quad , \quad s_{ij} = \frac{1}{2}\left(\frac{\partial u_i}{\partial x_j} + \frac{\partial u_j}{\partial x_i} \right) \tag{2-36}$$

The commutation between averaging and spatial differentiation involved here is based on (2-31).

Averages of products are computed in the following way:

$$\begin{aligned}\overline{\tilde{u}_i\tilde{u}_j} &= \overline{(U_i+u_i)(U_j+u_j)} \\ &= U_iU_j + \overline{u_iu_j} + \overline{U_iu_j} + \overline{U_ju_i} \\ &= U_iU_j + \overline{u_iu_j}\end{aligned} \tag{2-37}$$

The terms consisting of a product of a mean value and a fluctuation vanish if they are averaged, because the mean value is a mere coefficient as far as the averaging is concerned, and the average of a fluctuating quantity is zero.

If $\overline{u_iu_j} \neq 0$, u_i and u_j are said to be *correlated*; if $\overline{u_iu_j} = 0$, the two are *uncorrelated*. Figure 2-7 illustrates the concept of correlated fluctuating variables. A measure for the degree of correlation between the two variables, u_i and u_j is obtained by dividing $\overline{u_iu_j}$ by the square root of the product of the *variances* $\overline{u_i^2}$ and $\overline{u_j^2}$ this gives a *correlation coefficient* c_{ij} which is defined by

$$c_{ij} \equiv \frac{\overline{u_iu_j}}{\left(\overline{u_i^2}\cdot\overline{u_j^2}\right)^{1/2}} \tag{2-38}$$

with the understanding that the summation convention does not apply in this case. If $c_{ij} = \pm 1$, the correlation is said to be *perfect.* Each variable, of course, is perfectly correlated with itself $(c_{aa} = 1 \quad \text{if} \quad i = j = a)$.

The square root of a variance is called a *standard deviation* or root-mean- square (rms) amplitude; it is denoted by a prime (for instance, $u_j' = \left(\overline{u_j^2}\right)^{1/2}$). A characteristic velocity, or “velocity scale” of turbulence at some down-stream position in a boundary layer might be defined as the mean r.m.s. velocity taken across the boundary layer at that position; in this way velocity scales used in dimensional analysis could be given a precise definition whenever desired.

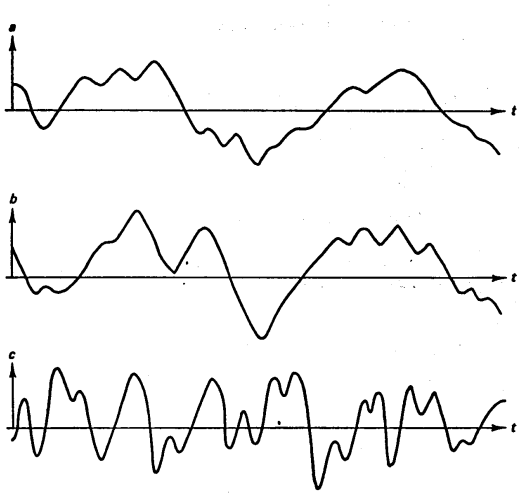

Figure 2-7.- Correlated and uncorrelated fluctuations. The fluctuating variable *a* has the same sign as the variable *b* for most of the time; this makes $\overline{ab} > 0$. The variable *c*, on the other hand, is uncorrelated with *a* and *b*, so that $\overline{ac} = 0$ and $\overline{cb} = 0$.

In turbulence, the description of the flow at all points in time and space is not feasible. Instead, following Reynolds (1895) equations governing mean quantities, such as the mean velocity have been developed. The equations of motion of an incompressible fluid are:

$$\frac{\partial \tilde{u}_i}{\partial t} + \tilde{u}_j \frac{\partial \tilde{u}_i}{\partial x_j} = \frac{1}{r} \frac{\partial}{\partial x_j} \tilde{s}_{ij} \tag{2-39}$$

$$\frac{\partial \tilde{u}_i}{\partial x_j} = 0 \tag{2-40}$$

Here, $\tilde{s}_{ij}$ is the *stress tensor*. Repeated indices in any term indicate a summation over all three values of the index; a tilde denotes the instantaneous value at (x_i, t) of a variable on which no Reynolds decomposition into a mean value and fluctuation has been performed.

If the fluid is Newtonian, the stress tensor $\tilde{s}_{ij}$ is given by

$$\tilde{s}_{ij} = -\tilde{p}d_{ij} + 2m\tilde{s}_{ij} \tag{2-41}$$

In (2-41), d_{ij} is the Kronecker delta, which is equal to one if $i = j$ and zero otherwise; $\tilde{p}$ is the hydrodynamic pressure and m is the dynamic viscosity (which is assumed to be constant). The *rate of strain* $\tilde{s}_{ij}$ is defined by

$$\tilde{s}_{ij} = \frac{1}{2}\left(\frac{\partial \tilde{u}_i}{\partial x_j} + \frac{\partial \tilde{u}_j}{\partial x_i} \right) \tag{2-42}$$

If (2-41) is substituted into (2-39) and if the continuity equation (2-40) is invoked, the Navier-Stokes equations are obtained:

$$\frac{\partial \tilde{u}_i}{\partial t} + \tilde{u}_j \frac{\partial \tilde{u}_i}{\partial t} = -\frac{1}{r}\frac{\partial \tilde{p}}{\partial x_i} + n \frac{\partial^2 \tilde{u}_i}{\partial x_j \partial x_j} \tag{2-43}$$

Here, n is the kinematic viscosity $(n = m/r)$.

If Reynolds decomposition procedure is applied to (2-43), we obtain the well known Reynolds equation that includes an extra term due to the correlation between velocity fluctuations

$$-\frac{\partial}{\partial x_j}\overline{u_i u_j} \tag{2-44}$$

Mixing Due to Shear-Free Turbulence

The interaction of turbulence and the density interface produces mixing and entrainment, and this interaction process is not well understood from a fundamental point of view. Here a description by Linden (1973) revised by Fernando (1989) is presented, this description of the local mixing process focuses on a sharp fluid interface. In the case we are studying in this thesis, the mixing takes place at the interface between a fluid an a sediment bed, following Sánchez and Redondo (1998) we could consider that the same type of processes take place. They stated that a close analogy between sediment charged fluids exist, noting that similarly to stratification, a sediment laden fluid extracts turbulent kinetic energy (TKE) from the flow. The main difference is that mixing in a stratified fluid is irreversible, but sediments are only maintained in suspension as long as there is enough turbulence to balance the falling down velocity of the solid particles. The latter is call “reversible mixing”.

When there is no interfacial mean velocity jump ($\bar{U} = 0$), there will be no TKE production near the interface, and thus entrainment can only occur by turbulence that is produced elsewhere and reaches the interface by turbulent diffusion. Linden (1973) studied mixing induced by impinging spherical vortex rings of characteristic length and velocity l and u, respectively, on a sharp density interface. An ensemble of such rings was assumed to be a good approximation of integral-scale eddies. Upon impact, both the interface and the rings distort, and when the maximum deflection is reached, the buoyancy forces cause the interface to recoil and splash heavy fluid in to the upper layer.

When the splashing mechanism is active, it is possible to assume that most of the kinetic energy of the impinging eddies is used to rise heavy fluid out of the interface, and thus the rate of change of potential energy can be considered to be proportional to the divergence of the kinetic energy flux.

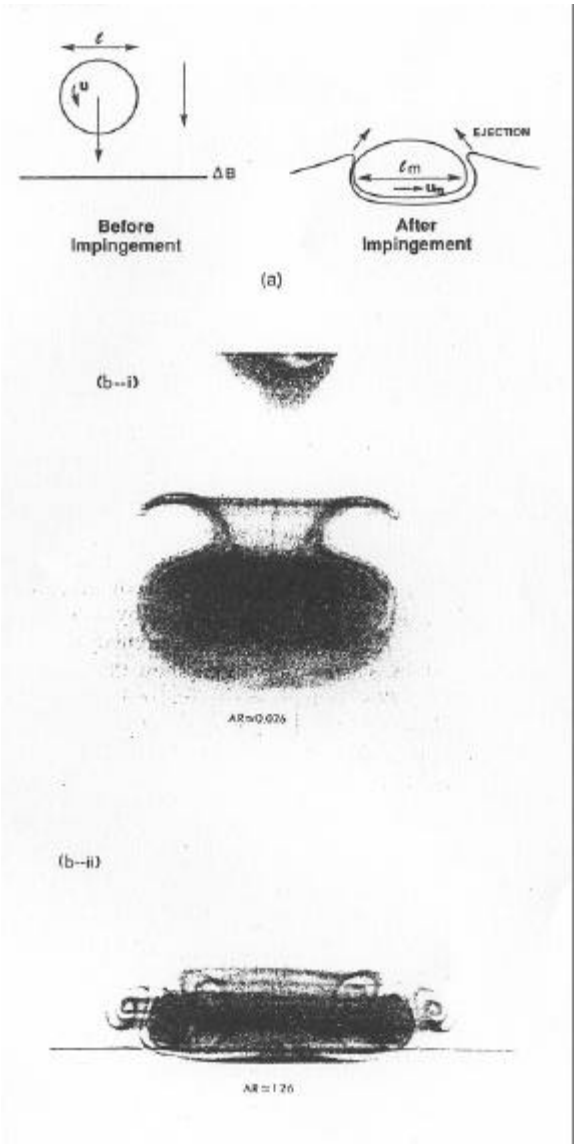

Figure 2-8.- (a)Interaction of a vortex ring with a density interface and subsequent evolution. (b) Photographs taken at different times.

2.3 Grid Stirred Turbulence

There are many situations in nature where turbulence generated at one position in a fluid causes mixing across a density interface some distance away. This could be reproduced in a mixing box with an oscillating grid which produces the so-called “Grid Stirred Turbulence”.

The flow produced by the oscillating grids can be discussed in terms of three consecutive processes:

1.- Very close to each grid bar, there is the generation of a quasi-steady jet flow. The form and intensity of the motion in this region depends on the cross-section of the bars and on the amplitude, and there may be an explicit dependence on viscosity.

2.- The jets interact, and break down to give turbulence which is advected by the jets.

3.- Turbulence decays with distance away from the grid.

In order to understand the mixing across an interface located some distance away from the oscillating grid, one needs to know the properties of the turbulence in the region of interest, i.e. near the interface. These can be measured directly as functions of distance from the stirrer centre of oscillation, but they will depend on all the above processes.

When a grid of crossed bars is oscillated vertically with a stroke (amplitude) comparable to the bar diameter it generates an array of jets whose centre-lines pass through the intersection points. Further away from the grid, the regularity is lost, for two reasons. Each individual jet breaks down and becomes turbulent, by a process of shear instability at its edges, and there is also an interaction between the jets. Using bars of circular cross-section, for instance, the presence of the individual jet flows is still detectable on streak photographs up to a distance of about twice the spacing, but beyond that they merge to form an irregular turbulent flow. Jet flows remain distinct for about two mesh lengths (M), then combine in a pattern which is determined by the shape of

the tank, and by small differences in the strength of the flow from different parts of the grid.

It is possible that the action of a stirring grid in a tank (in producing mixing across a density interface, for example) may depend essentially on the steady component of the flow as well as on the turbulence. If so, such measurements would be very specific to the particular apparatus, and not easily transferred to other situations. Fortunately, Thompson and Turner (1975) proved that the unsteady turbulent motions did make the dominant contribution to the measured velocities in the tank, and it is therefore reasonable to make more general deductions from particular measurements, provided that they are made not too close to or far away from the stirring grids.

In the specific case of grid stirred turbulence, there is no mean flow. The structure of the flow is therefore entirely determined by the velocity fluctuations induced by the grid. An empirical relation (2-45) for the root-mean-square velocity was proposed by Hopfinger & Toly (1976), using $M / d = 5$

$$u' = C_3 \, s^{3/2} \, M^{1/2} \, w \, z^{-1} \qquad (2\text{-}45)$$

Here s is the stroke (amplitude) of the grid, M is the mesh size of the grid (the distance between bar centrelines), w is the oscillation frequency (in hertz) of the grid, z is the distance to the grid, and d is the bar size. They determined C_3 to be close to 0.3 for their experimental set-up.

The dependence of the integral length-scale L on the distance z is given by $L = b\,z$. Literature agrees on the linear relation given by (2-45), but disagrees on the actual value of b. Some studies found b to depend on stroke s when $s/M \leq 0.8$, other studies found little difference between $s/M = 0.8$ and $s/M = 0.2$, where $b = 0.10$.

Assuming an Energy balance between the total input energy provided by the grid, the energy stored in the tank and the energy dissipated by the system, Sánchez and Redondo (1998) propose a simple 1-D model. They also obtained, experimentally, a

value for c_3 of 0.03 for an experimental configuration using $M=5$. And in Redondo and Sánchez (1997), a value for constant c_3 of 0.25 was found for a grid with $M=0.8$.

Chapter 3

OBJECTIVES AND METHODS

The overall objective is to test the possibilities of a well-known experimental configuration, used for the study of stratified fluids in a turbulent flow with zero-mean flow (oscillating grid mixing box), on the study of sediment transport, and to get to know what aspects involved in this phenomena could be explored from this new perspective.

To achieve this goal, some verification and adjustments to the parameterizations given in the bibliography for the r.m.s. turbulent velocity, u', generated by an oscillating grid had to be done to satisfy our necessities. This implied, as a first step, the calibration of the different mixing boxes and grids to be used through a series of experiments. This will give a clear view of the behaviour of the flow in all the mixing boxes. Among the flow parameters analyzed are the mean velocity, $\bar{u}$, the turbulent velocity as the r.m.s. velocity u', the turbulent length scales L, the turbulent energy q, the autocorrelations and energy spectrums, as well as the determinations of the different constants needed for a correct parameterization of the u' for each experimental configuration.

Traditionally, all experiments dealing with an oscillating grid mixing box measured the different flow properties in the region between the grid and the fluid free surface. In our interest of studying sediment transport, we needed to be able to know the flow properties in the region between the grid and the bottom (solid boundary). In order to do so, a special experimental configuration was designed and performed.

A second step needed to reach the goals of this research was to performe experiments with actual sediment. The experiments had to include sediments with different characteristics, for instance, different sediment sizes (from clay to medium sands) including samples made of single sediment size and samples extracted from the

seabed. The results obtained had to be compared with some classical results or methods. In this line, some assumptions were made and had to be studied, for example, the assumption that the estimated u' at the surface of the sediment bed is equal to the turbulent friction velocity u_* used in other experiments dealing with sediment transport. Following the line of comparing the obtained results with classical methods, an experiment to compare the sediment behaviour under a sheared flow (recirculation tank) and under a no-sheared flow (zero-mean flow oscillating grid mixing box) had to be designed and performed.

Among the different techniques used for all the experiments we were able to point out two, Acoustic Doppler Velocimetry (ADV) and Image Analysis through the facilities of Digimage software. These techniques have a great versatility of their own, and especially if they are used together in a combined form. With them we were able to measure, among others, the critical u' for sediment motion and for sediment lift off, sediment mass flux after lift off and sediment settling velocity.

The velocity measurement device used during the experiments is described next and some technical specifications are also given. The ADV is a high-precision instrument (Nortek, 2000) that measures all three flow velocity components. The ADV uses acoustic sensing techniques to measure flow in a remote (5.0 cm) sampling volume. The measure flow is practically undisturbed by the presence of the probe. The maximum sampling rate is 25 Hz.

The instrument consists of three modules: The measuring probe, the conditioning module and the processing module. The measuring probe is an acoustic sensor that consists of one transmit transducer and three receive transducers (Figure 3-1). The receive transducers are mounted on short arms around the transmit transducer at 120° azimuth intervals. The acoustic beams are oriented so that the receive beams intercept the transmit beam at a point located at 5.0 cm below the sensor. The interception of these four beams, together with the transmit pulse, define the sampling volume. This volume is 0.3-0.9 cm (user define) long and approximately 0.6 cm in diameter. All three receivers must be submerged to ensure correct velocity measurements.

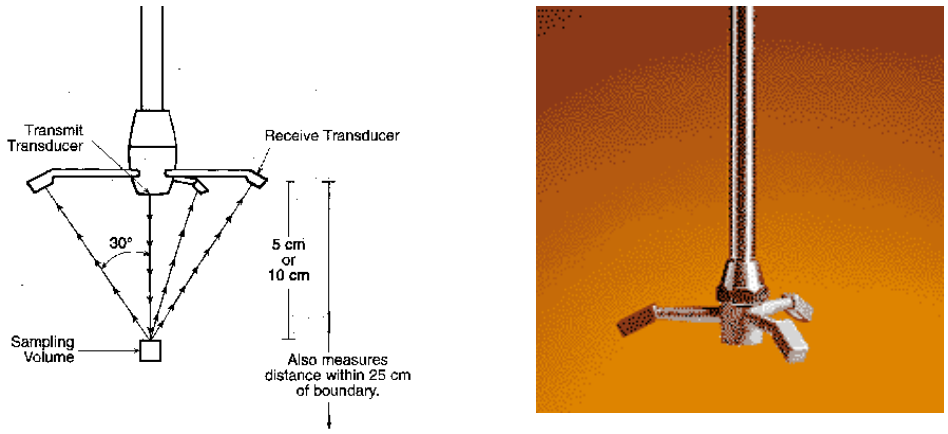

Figure 3-1.- ADV measuring probe. Transmit transducer and receive transducers are shown. (Images obtained from the Sontek Web Page)

ADV calibration factors are determined by the speed of sound and by the angles between the transmit and receive transducers. To ensure that the correct speed of sound is used, the water temperature and salinity must be entered in the data acquisition software. The calibration angles are measured at the factory and need only be changed when a new probe is installed. Maintenance calibration is not required unless the probe is physically damaged.

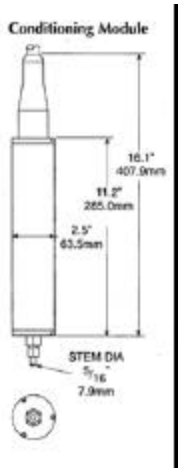

Figure 3-2.- ADV conditioning module. (Image obtained from the Sontek Web Page)

The processing module performs the digital signal processing required to measure Doppler shifts. This computationally intensive task is implemented on a PC-board. The data are recorded to disk in highly compressed binary files, which can be easily converted to ASCII format with the data conversion programs supplied with the system.

The water must have some suspended particles. In these experiments water was seeded with hollow spheres with a density close to that of water and size around 10 μm. The choice of size is motivated by the relatively strong echo that this particle generates per unit of concentration.

The liquid used to perform the experiments was fresh water at room temperature (23.0° ± 3.0°). It was plain tap water and no filtering was carried out, although, the amount of suspended particles was very low. This can become a problem if an acoustic device is going to be used to measure velocities in the fluid.

To prevent ADV velocity data from looking “noisy” due to a low concentration of scatterers in the water, some seeding material was added. It is recommended that clear basins, flumes or tanks are seeded with hollow spheres that have a density close to that of water and a size around 10 μm. Particles that are close to neutrally buoyant will remain in suspension without additional stirring and are ideal for low-flow experiments. The choice of size is motivated by a relatively strong echo generated by these particles per unit of concentration. Smaller particles (e.g. 1 μm particles used to seed Laser Doppler systems) are not recommended because the required concentration is quite high.

The seeding used during these experiments was obtained directly from Nortek AS Company. The particle size was 10 μm and the concentration used was between 10 and 50 grams per cubic meter.

Table 3-1.- Acoustic Doppler Velocimeter: Technical Specifications.

Acoustic Frequency:	10 MHz
Velocity Range:	±0.03, 0.10, 0.30, 1.0, or ±2.5 $^{m}/_{s}$
Velocity Resolution:	0.1 mm/s
Velocity Bias:	±1%, no measurable zero-offset in the horizontal direction
Random Noise:	Approximately 1% of velocity range at 25 Hz
Sampling Rate:	Programmable from 0.1 to 25 Hz
Sampling Volume:	Less than 0.25 cm^3
Minimum Water Depth:	20 mm for side-looking, 2-D probe, 60 mm for all 5 cm probes, and 120 mm for 10 cm probes
Minimum Distance from Sampling Volume to Boundary:	5 mm
Maximum Water Depth:	30 m
Probe Electronics:	Operating Temperature: 0 to 40°C Storage Temperature: -10 to 50°C
Power:	Power Supply.-110/220 Volt AC Voltage in the probe cables do not exceed ±12 VDC (50 mA) and 20 Vrms AC (100 mA)
Control and Communication Lines:	Analog u, v, and w: Optional (±5 V,±10 V) Analog Signal Strength: No Serial Communication: No Power Enable (Sleep mode): No TTL External Synch I/O: Yes

Chapter 4

GRID FLOW CALIBRATION EXPERIMENTS

In this chapter all experiments carried out to calibrate the zero mean flow turbulence tanks used are described, as well as the results obtained. All experiments were done at the Fluids Laboratory of the Applied Physics Department of the Catalonian University of Technology (Laboratorio de Fluidos, Departamento de Física Aplicada, Universidad Politécnica de Cataluña - UPC). The experiments performed during this part of the work are divided into two categories (Free Surface Experiments (FSE), Solid Boundary Experiments (SBE)). A final section is also included in which a description of the transition from jet flow to turbulence is shown.

In the first category (**FSE**), the experimental configuration is similar to those used by previous authors (Turner (1968), Thorpe (1966),Turner (1973), Thompson and Turner (1975), Hopfinger and Toly (1976), Xuequan and Hopfinger (1987), Tsai and Lick (1987), Noh and Fernando (1991), Huppert, Turner and Hallworth, (1995), Redondo, Sánchez, Castilla. (1995), Peters and Redondo (1997), Sánchez and Redondo, (1998), Redondo and Sánchez (1999), Mann, Ott and Andersen (1999), Ott and Mann (2000), Redondo and Sánchez (2000), Matas and Redondo (2000), Medina, Sánchez and Redondo (2001)). Two different grids and three different tanks were used and are described in detail further on as well as all measurements taken.

In the second category (**SBE**), the experimental configuration was modified in order to be able to measure the flow velocities near the wall under the grid (unlike the **FSE** where measurements were taken between the grid and the free surface) using the Acoustic Doppler Velocimeter (ADV). The specific configuration as well as the measurements taken are described further on. The difference between this configuration and the one used by Hunt and Graham (1978) is also mentioned.

A total of three different tanks were used for the **FSE**. Two of them were large enough to use a 5 mesh grid (**5MG**) like the one used by previous authors (mentioned before in this chapter). The difference between these two tanks was the size. The one used in the **5MG-FSE** was the smaller of the two. This one, unlike the one used for the **5MG-FSE-FFTA**, had the advantage that the experimental configuration could be easily modified for the experiments with a solid boundary (**SBE**). On the other hand, the tank used for **5MG-FSE-FFTA** had the advantage of allowing measuring with two ADVs simultaneously. Thus we were able to compare between to different configurations with the same type of grid and have the possibility of comparing between the **FSE** and the **SBE** experiments.

The third tank used during the **FSE** was much smaller than the previous two. The goal pursued by using this tank was to have a portable system where recently extracted seabed cores could be analyzed. This tank was used further with cores extracted from the Gulf of Lion and this is explained further on in this work (Chapter 6).

4.1 Free Surface Experiments (FSE)

The goal of this first group of experiments was to find out if the flow field driven by the grid, between the latter and the free surface, could be described using equation (4-1), and if so, find the proper constant c for each grid. Different kinds of experiments with different grids were performed in order to measure the turbulent velocity field and calibrate the equation for each experimental configuration .

$$u' = c\, s^{3/2} M^{1/2} w\, z^{-1} \qquad (4\text{-}1)$$

4.1.1 5.0 cm Mesh Grid (5MG- FSE) Experiments

4.1.1.1 Grid:

The grid used (Figure 4-1) was a 1.0 cm of square section plastic solid bars with 5.0 cm between centres (M = 5.0 cm (**5MG**)) and solidity $S = 0.36$ (Turner (1968),

Thorpe (1966),Turner (1973), Thompson and Turner (1975), Hopfinger and Toly (1976), Xuequan and Hopfinger (1987), Tsai and Lick (1987), Noh and Fernando (1991), Huppert, Turner and Hallworth, (1995), Redondo, Sánchez, Castilla. (1995), Peters and Redondo (1997), Sánchez and Redondo, (1998), Redondo and Sánchez (1999), Mann, Ott and Andersen (1999), Ott and Mann (2000), Redondo and Sánchez (2000), Matas and Redondo (2000), have all used the same type of reid of solidity $S = 0.36$). The approximate clearance between the grid and the tank walls was of 1.0 cm to avoid as much as possible the secondary flow that is produced by the grid (Mann, Ott and Andersen (1999) and Ott and Mann (2000)).

The grid was attached at the centre with a stainless steel rod attached at the other end to the motor eccentric drive (See Motor and Supporting Structure further on in this section). The lower end of the rod had 5 cm of screw thread. This thread allows to position the grid vertically at the exact distance from the bottom or sample. This particular characteristic is of importance in experiments dealing with a solid boundary or sediment samples where it is necessary to set a pre-established distance between the centre of oscillation and a given point (Z), as the wall under it or the sediment surface.

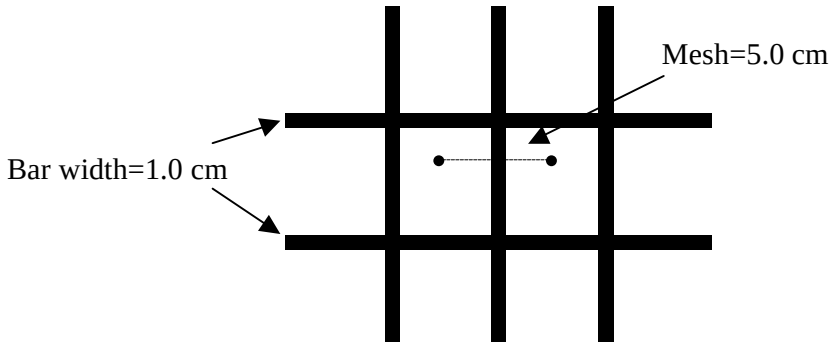

Figure 4-1.- Schematic drawing of the **5MG**.

4.1.1.2 Tank:

All experiments performed with the **5MG** were carried out in an open transparent Perspex tank of 27.0 cm square in internal cross-section, 50.0 cm height, and 0.9 cm thick walls (Figure 4-2). This tank is similar to the one used by Turner (1968), Thorpe (1966), Turner (1973), Thompson and Turner (1975), Hopfinger and Toly (1976), Xuequan and Hopfinger (1987) and others.

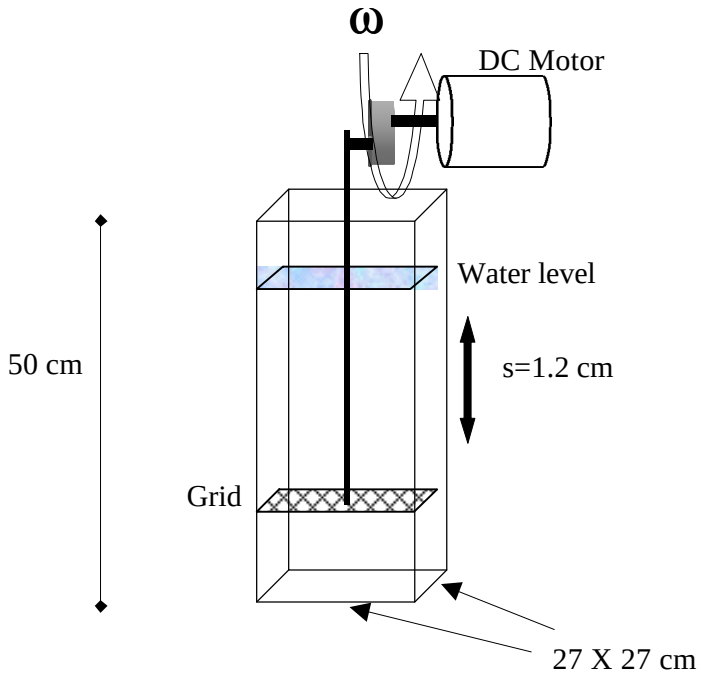

Figure 4-2.- Schematic drawing of the tank used for the experiments corresponding to the **5MG**.

4.1.1.3 Motor and Supporting Structure:

An electric DC motor (Mavilor-Dc Motor: Model 80, 150 Watt, 40 Volt, 5 Amp, 6000 – 10000 RPM) was used to move the grid up and down through an eccentric drive. The frequency of oscillation of the grid was controlled by limiting the voltage input to

the motor. This was done with a 5-15 V power supply unit (ATAIO: Model 152a), and the voltage input to the motor was measured using a multimeter (PHILIPS: Model PM 2517 X, Volt Accuracy 0.2 ± 0.05).

The motor was mounted on an aluminium structure for support (Figure 4-2). This structure was placed surrounding the Perspex tank. An important characteristic is that the aluminium structure must have no contact with the tank. This prevents most of the vibrations generated by the motor to interfere with the experiment.

The grid was attached to the eccentric drive by a stainless steel rod that ran through a tube attached to the supporting structure. Two Teflon O-rings inside the tube guided the rod parallel to the long axis of the supporting structure. At the end, where the grid was attached, the rod had 5.0 cm of screw thread. This thread enabled us to move the grid up and down to the desired position by using two nuts, above and under the grid, with the possibility of displacing the grid ± 2.5 cm. This characteristic is very useful when regulating the distance between the grid's centre of oscillation and the sediment samples or any other specific point in which we are interested (i.e. liquid interface, rigid boundary, sediment surface, etc.).

The stroke (s in equation **(4-1)**) could be adjusted by sliding the attaching screw of the eccentric drive to the driving shaft along the radius of the eccentric drive.

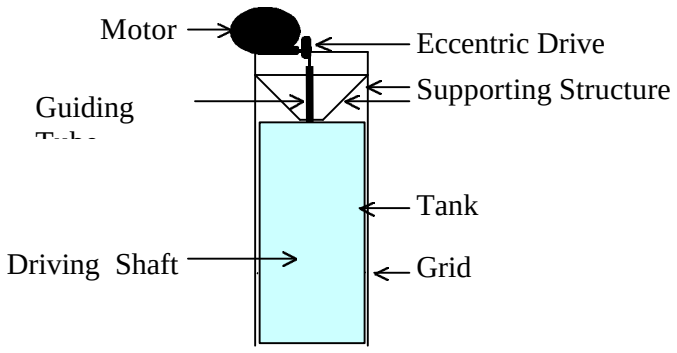

Figure 4-3.- Schematic drawing of supporting structure and relative position of the tank (**5MG-FSE**).

4.1.1.4 Acoustic Doppler Velocimeter (ADV) liquid and tracers (seeding):

The 3D ADV measurement device described in chapter 3 was employed (see chapter 3 for technical specifications). The liquid used to perform the experiments was fresh water at room temperature (23.0° ± 3.0°). To avoid ADV velocity data from looking "noisy", due to a low concentration of scatterers in the water, some seeding material was added. The seeding used during these experiments had a particle size of 10 μm and the concentration used was between 10 and 50 grams per cubic meter.

4.1.1.5 Configuration of 5MG-FSE :

The same general configuration used by different authors was used here (Turner (1968), Thorpe (1966),Turner (1973), Thompson and Turner (1975), Hopfinger and Toly (1976), Xuequan and Hopfinger (1987), Tsai and Lick (1987), Noh and Fernando (1991), Huppert, Turner and Hallworth, (1995), Redondo, Sánchez, Castilla. (1995), Peters and Redondo (1997), Sánchez and Redondo, (1998), Redondo and Sánchez (1999), Mann, Ott and Andersen (1999), Ott and Mann (2000), Redondo and Sánchez (2000), Matas and Redondo (2000), Medina, Sánchez and Redondo (2001)). The grid was placed horizontally at mid depth so it could oscillate vertically as far as possible from the bottom and the free surface. The water depth was of 40.0 cm. The stroke, s, (amplitude of oscillation) was fixed at 1.2 cm.

The tank was fitted into the engine support frame in a vertical position. The shaft was located at the centre of the tank. The ADV was positioned vertically in the tank parallel to the driving shaft at mid-point between the shaft and a corner of the tank. It was possible to vary the vertical position of the ADV by extending the ADV support structure.

4.1.1.6 Measurements:

Time series of velocity were taken with 3 different oscillating frequencies, w, (3.6, 4.88, and 6.16 Hz) at 9 positions above the grid's centre of oscillation (1.7, 3.7, 5.5, 7.8, 9.7, 11.7, 13.7,15.7 and 17.6 cm). Time series were taken during 5 minutes at the highest sampling frequency of the ADV (25 Hz). This made a total of 27 data sets

made up by 7500 data points each. After 5 minutes it was possible to detect a strong secondary flow, this was the reason for not doing longer series.

Three more time series were taken at 6.0 cm from the grid's centre of oscillation at w = 6.16 Hz. One directly above a grid bar, another one above the intersection of two bars, and the last one between two bars (Figure 4-8). These time series were measured in order to see the differences, if any, in the flux depending on the relative position between the sampling position and the grid. Near the grid there is the generation of a quasi-steady jet flow close to each grid bar (Thomson and Turner, 1975). After a certain distance, jets interact, and break to give turbulence which is advected by the jets.

4.1.1.7 Results: Free Surface, 5cm Mesh Grid (FSE-5MG):

In this section all FSE-5MG results are presented. It is important to bear in mind that all measurements were taken on top of the grid between it and the free surface.

4.1.1.7.1 Grid Frequency Calibration:

The parameter controlled during the experiments was the grid's frequency. This was done by controlling the voltage input to the driving motor. In order to get to know the frequency of oscillation corresponding to any voltage input value, some calibration voltage-hertz was carried out.

Some of the experiments were recorded on video tape and frequency was estimated from the recordings. Frequency of oscillation was estimated in real time for no recorded experiments. In both cases, the images were analyzed using a software package specially designed for fluid dynamic experiments (Digimage) (Dalziel, 1993). This software operates using a Data Translation Card DT-2861 on a P.C. computer.

The tank was lit from behind and experiments recorded using a compact PAL system VHS-C colour video camera (JVC, GR-AX200). The images were manipulated with the facilities provided by Digimage. The frequency of oscillation of the grid was measured directly from the digitized images. A typical image showing the grid's

movement in time is presented in Figure 4-4. This figure is a time series where time is in X-axis and distance (grid displacement) is in Y-axis. The oscillation of the grid is seen as an oscillatory uniform signal. The image is made up by 512 pixels in both directions (512 columns and 512 rows). Each column, 1 pixel width, is captured at a pre-specified time span (during these experiments the time interval was of 0.04s), and during a pre-establish acquisition time (Figure 4-4 a) 20s time series, b) 10s time series). Thus, a time series at a specific vertical position is created.

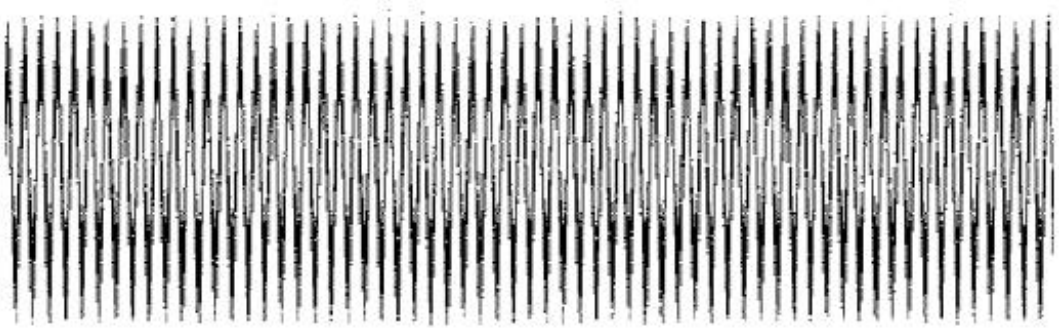

a)

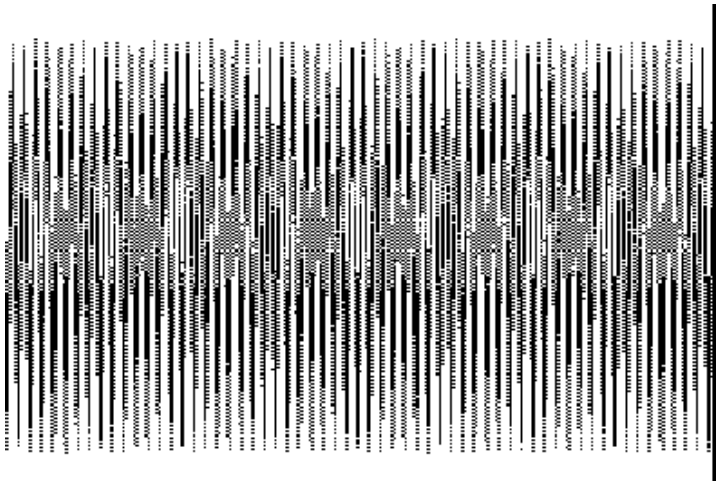

b)

Figure 4-4.- Time series of grid oscillation. a) a 20s series at 4.0v input to motor. b) a 10s series at 6.0v input to motor.

Once all the experiments were analyzed for frequency estimation, a linear adjustment was made to the data (volt-hertz). This enabled us to get to know the frequency of oscillation corresponding to value of voltage input at any given time

during further experiments. The result of this linear adjustment is presented in Figure 4-5.

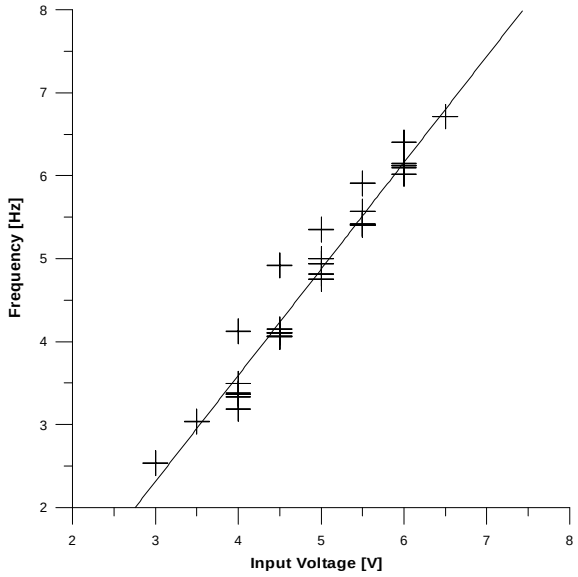

Figure 4-5.- Voltage input Vs. Frequency of Oscillation. FSE-5MG.

4.1.1.7.2 Mean velocity and Root Mean Square (r.m.s) Turbulent Velocity:

In Figure 4-6, the mean velocity $(\bar{u},\bar{v},\bar{w})$ and the r.m.s. turbulent velocity (u',v',w') estimated as

$$u' = \left(\overline{u^2} \right)^{1/2} \qquad \textbf{(4-2)}$$

are plotted for each sampling point and for the three different frequencies analyzed. In Figure 4-7, the mean velocity $(\bar{u},\bar{v},\bar{w})$ and the r.m.s. turbulent velocity (u',v',w') for each sampling point and for the three different frequencies analyzed, are

plotted in a non-dimensionalized form, using ωM as the relevant velocity scale near the grid. ωM

It is clearly seen, that the mean velocity is nearly zero except close to the grid. This was expected because, as mention before in this work, a quasi-steady jet flow generates close to each grid bar (Thomson and Turner, 1975). After a certain distance, jets interact, and break to give turbulence which is advected by the jets. It is also expected that after turbulence is generated, no mean flow, or at least no steady mean flow is present. Some analysis was made using a running average for estimating the r.m.s. turbulent velocity, u', and no difference was found after turbulence was fully developed. As a mater of fact, if u' using plain average and u' using running average are plotted together, there is a clear difference near the grid. As we go farther from the grid, both u' merge to about the same value (the former is shown further on at the end of this chapter).

It is from this point on, where the different u' merge, where turbulence is fully developed and starts to decay. This point corresponds, in Figure 4-6 and Figure 4-7, to the height where the three components of velocity, and u', merge together. For the mean velocity, some fluctuations are presented after this point, and differences between the components are seen, but remain almost constant with height. For the u' graphs, after this point, the values of the three components are very similar. This confirms that the generated turbulence is isotropic ($u' \cong v' \cong w'$), as stated by Hopfinger and Toly (1976)

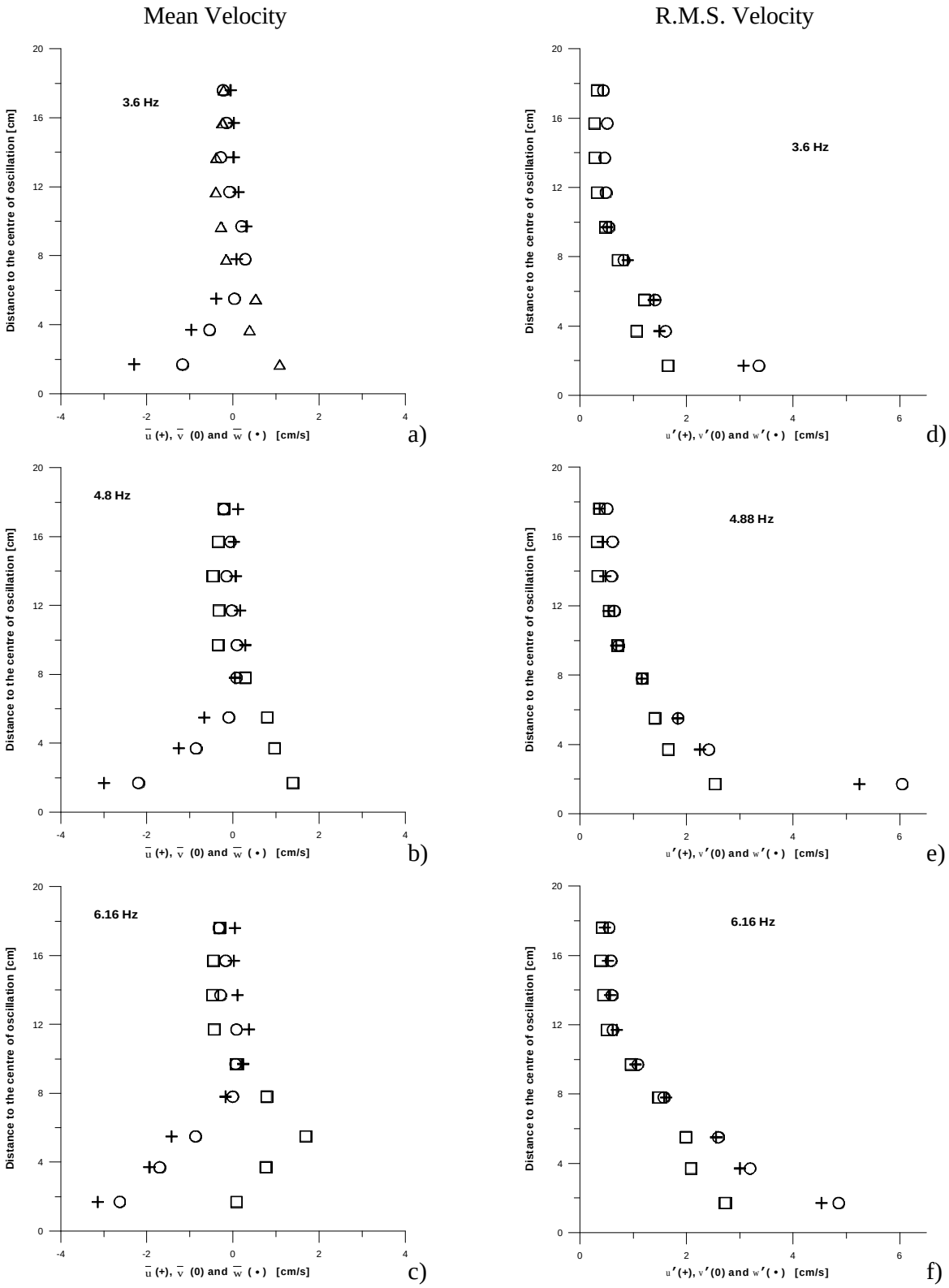

Figure 4-6.- Mean velocity and r.m.s. turbulent velocity. (FSE-5MG)

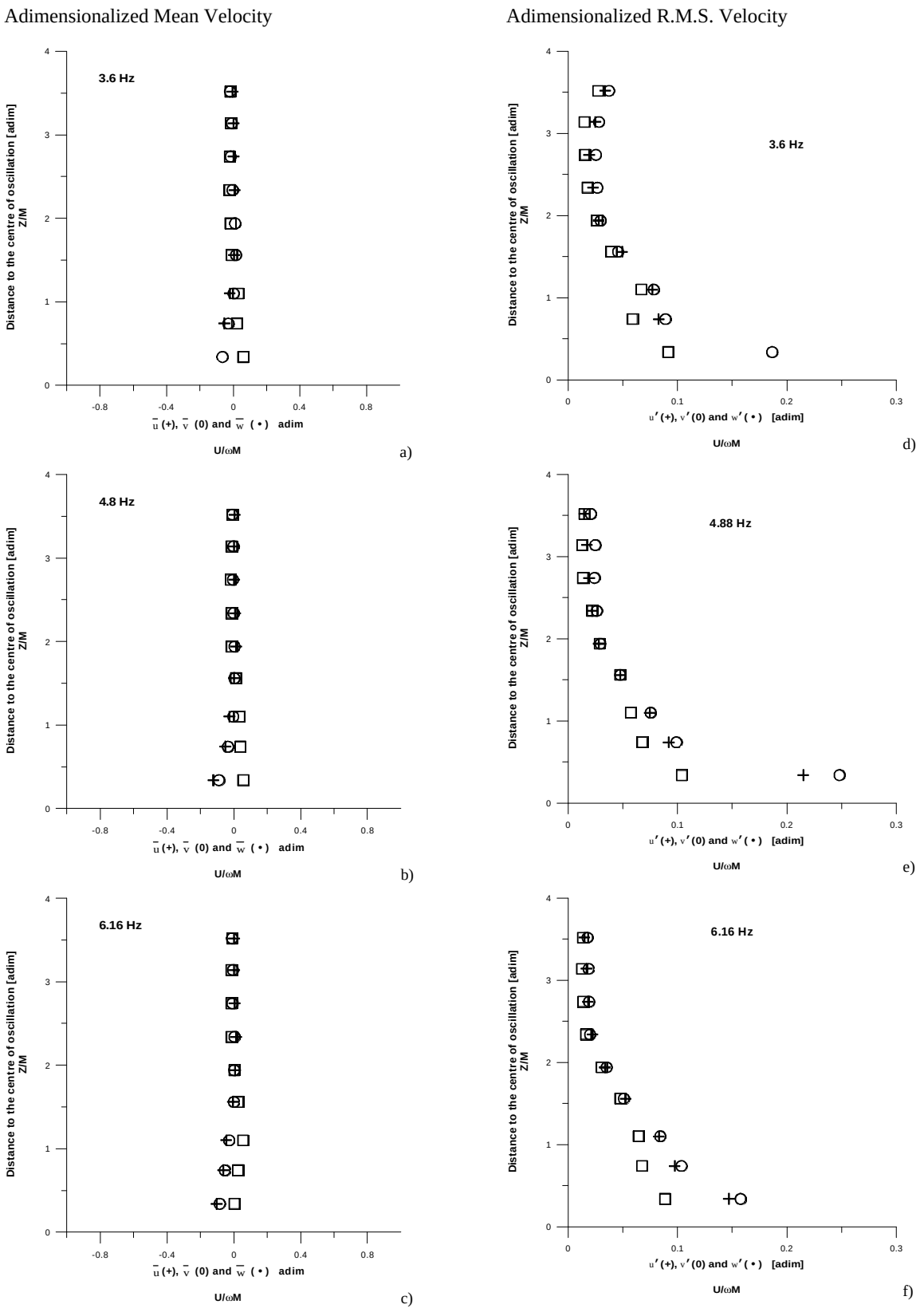

Figure 4-7.- Adimensionalized mean velocity and r.m.s. turbulent velocity. (**FSE-5MG**)

4.1.1.7.3 Time series at 6.0 cm from the grid:

Three more time series were taken at 6.0 cm from the grid's centre of oscillation at w = 6.16 Hz. One directly above a grid bar (Bar), another one above the intersection of two bars (Intersection), and the last one between two bars (Centre) (see Figure 4-8).

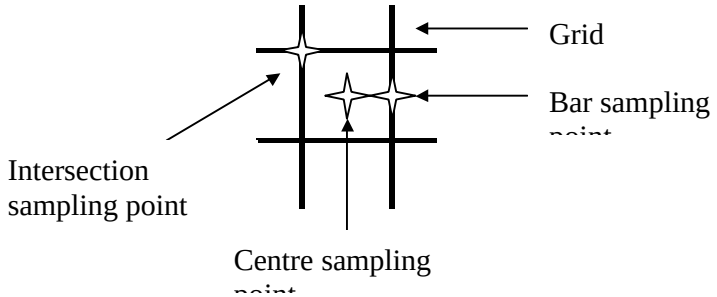

Figure 4-8.- Schematic drawing of the measuring points at 6.0 cm above the grid.

In Figure 4-9 and Figure 4-10, the corresponding values for the mean and r.m.s. velocities are plotted for the three velocity components. In Figure 4-9 a), the mean velocity is plotted and in b) the magnitude of the velocity is shown. At 6.0 cm from the grid's centre of oscillation, the system has not reached fully developed turbulence. This may be seen in the values of $\overline{w}$ in Figure 4-9 a), where the three values are positive, reflecting the presence of jet-like flows produced by the grid bars. It is also seen in Figure 4-10, where r.m.s. velocity is plotted. The values for $\overline{w}$ are always lower than for the other two components, meaning that in the Z direction there is a flow with less velocity fluctuations than in the horizontal plane. This could also be reflecting the jet-like flow in the vertical direction.

This effect is more intense directly above the grid bar. The former is seen in Figure 4-9 b) at the Bar point, where the higher difference between $\overline{w}$ and the other two velocity components may be found.

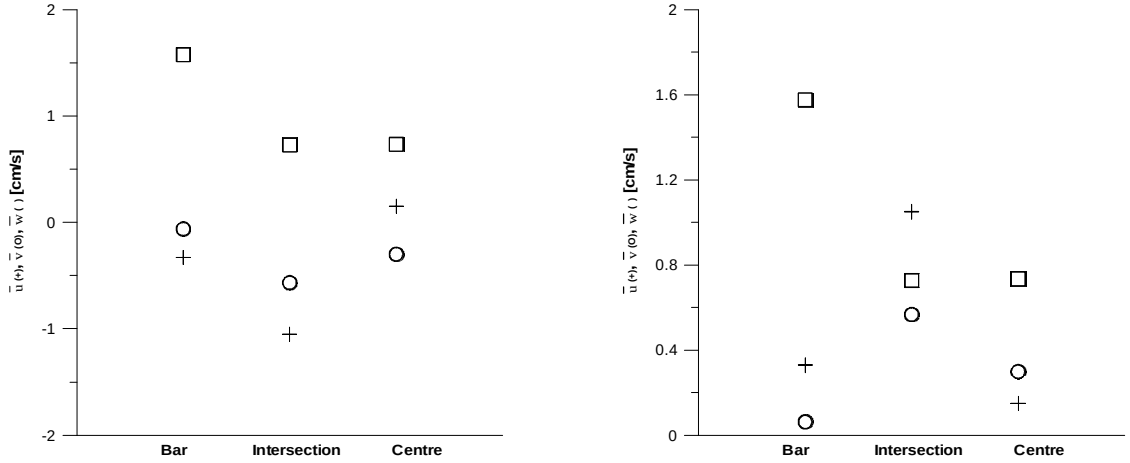

a) Mean velocity

b) Mean velocity-Absolute value

Figure 4-9.- Mean Velocity and the Absolute Value of the Mean Velocity at the three measuring points at 6.0 cm above the grid (u-(+), v-(O), w-( )).

In general, isotropy is fairly well developed in the horizontal plain, stated by the proximity of $\bar{u}$ and $\bar{v}$ values at the three points. The flow at the Centre point is the most isotropic of them all. This could be due to the fact that there is now a grid bar under it and therefore there is now vertical flow generation directly under it.

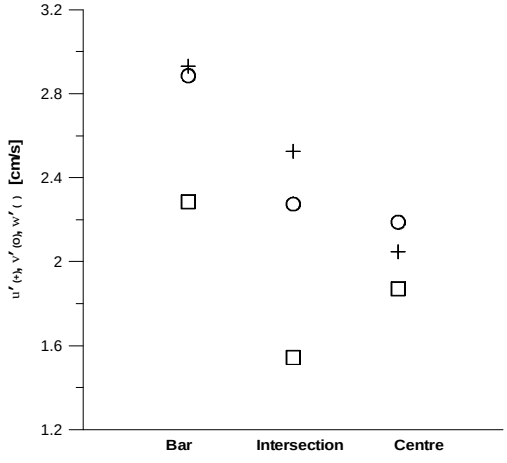

r.m.s. velocity

Figure 4-10.- Root Mean Velocity (r.m.s.) at the three measuring points at 6.0 cm above the grid.

4.1.1.7.4 Estimate of constant c :

A value of 0.5 for constant c was found to adjust well to the measured s_u. Because of the isotropic characteristic presented in the fully developed turbulence region, where the jet-like flows disappear, this c value adjusts also well to the s_v and s_w values in the turbulent region (Figure 4-11).

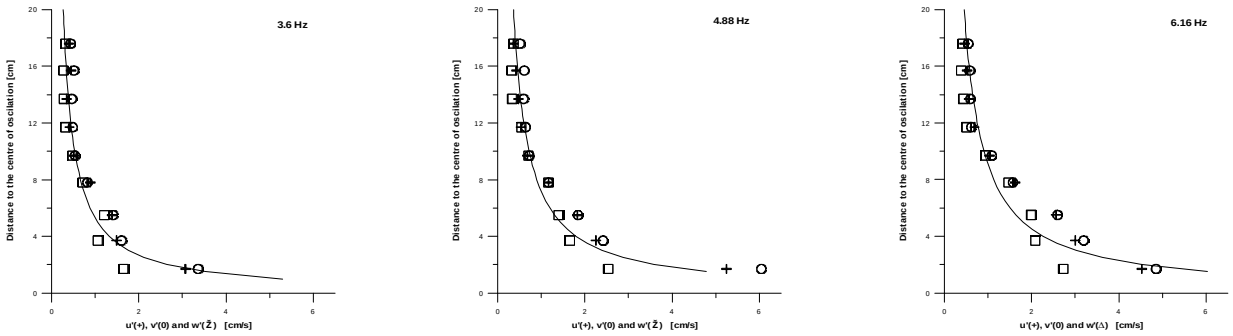

Figure 4-11.- The r.m.s. corresponding to **FSE-5MG** is plotted with the value obtained using equation **(4-1)** with $c = 0.5$

4.1.2 FFT and Autocorrelation Experiments (5MG-FSE-FFTA):

A new set of measurements was taken in a bigger tank where two ADV sensors could be measured simultaneously in order to estimate the FFT and the autocorrelations at different z above the grid. The grid had the same characteristics as the one used for the **5MG-FSE**.

4.1.2.1 Grid:

The grid used was a 1.0 cm of square section plastic solid bars with 5.0 cm between centres ($M = 5.0$ cm (**5MG**)) with solidity $S = 0.36$ as the one used in the **5MG-FSE**. The approximate clearance between the grid and the tank walls was of 1.0 cm to avoid as much as possible the secondary flow that is produced by the grid (Mann, Ott and Andersen (1999) and Ott and Mann (2000)).

The grid was attached at the centre with a stainless steel rod attached at the other end to the motor eccentric drive (See Motor and Supporting Structure further in this chapter).

4.1.2.2 Tank:

All experiments were performed in an open transparent Perspex tank 50.0 cm square in internal cross-section, 120.0 cm height, and 1.3 cm thick walls (Figure 4-12). This tank is similar to the one used by Turner (1968), Thorpe (1966), Turner (1973), Thompson and Turner (1975), Hopfinger and Toly (1976), Xuequan and Hopfinger (1987) and others.

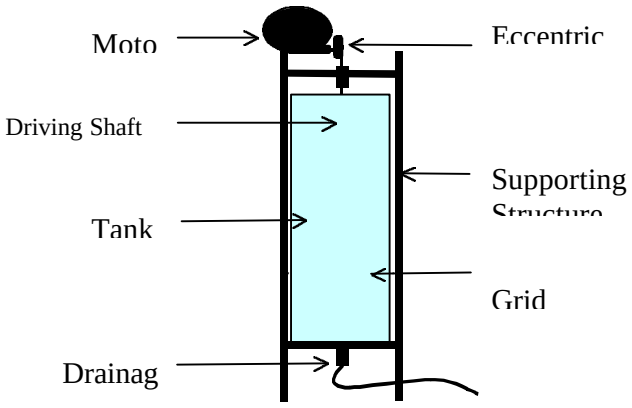

Figure 4-12.- Schematic drawing of the tank used for the experiments corresponding to the **5MG-FSE-FFTA**.

4.1.2.3 Motor and Supporting Structure:

An electric DC motor (Soprel-Dc Motor: 65 Volt, 3 Amp, 3000 RPM) was used to move the grid up and down through an eccentric drive. The frequency of oscillation of the grid was controlled by limiting the voltage input to the motor. This was done with a 5-15 V power supply unit (ATAIO: Model 152a), and the voltage input to the motor

was measured using a multimeter (PHILIPS: Model PM 2517 X, Volt Accuracy 0.2 ± 0.05).

The motor was mounted on a steel structure for support. This structure was placed surrounding the Perspex tank. The grid was attached to the eccentric drive by a stainless steel rod and the stroke was regulated in the same way as for the **5MG-FSE.** The stroke (s in equation **(4-1)**) was adjusted by sliding the attaching screw of the eccentric drive to the driving shaft along the radius of the eccentric drive.

4.1.2.4 Acoustic Doppler Velocimeter (ADV) liquid and tracers (seeding):

The same 3D ADV measurement device employed during the **5MG-FSE** was used (see chapter 3 for its technical specifications) plus a 2D ADV. This second device had the same technical specifications as the 3D ADV the only difference being that it only measured the two velocity components (u and v) parallel to the grid plane. This second ADV was used only to estimate the length scales by measuring the velocity correlations at different positions above the grid. All other results presented in this work are based on the 3D ADV measurements. Care was taken to avoid interference between the sensors and with the side walls.

The liquid used to perform the experiments was fresh water at room temperature (23.0° ± 3.0°). To avoid ADV velocity data from looking “noisy”, due to a low concentration of scatterers in the water, some seeding material was added. The seeding used during these experiments had a particle size of 10 μm and the concentration used was between 10 and 50 grams per cubic meter.

4.1.2.5 Configuration of 5MG-FSE-FFTA :

The same general configuration used in the **5MG-FSE** was employed. The grid was placed horizontally at mid depth with a water depth of 100.00 cm. The stroke, s, (amplitude of oscillation) was fixed at 1.2 cm. The tank was fitted into the engine

support frame in a vertical position (Figure 4-12). The shaft was located at the centre of the tank.

The ADVs where positioned vertically in the tank parallel to the driving shaft at mid-point between the shaft and a corner of the tank. It was possible to adjust the vertical position of the ADVs by extending the ADV support structure, as well as the horizontal distance between sampling points by sliding one or both ADVs in the supporting structure (Figure 4-12).

4.1.2.6 Measurements:

Time series of velocity were taken with 4 different oscillating frequencies, w, (2, 3, 5 and 6 Hz) at 6 positions above the grid's centre of oscillation (2, 6, 8, 10, 12 and 13 cm). Six time series were taken with each ADV simultaneously at different distances between each other (0.5, 1, 2, 3, 4 and 5 cm) in exactly the same plane at each of the five positions above the grid with the exception of the measuring point positioned 2 cm above the grid, where only one time series was taken with each ADV.

Time series were taken during 5 minutes at the highest sampling frequency of the ADVs (25 Hz). This made a total of 240 data sets composed of 7500 data points each (1.8×10^6 total data). After 5 minutes it was possible to detect a strong secondary flow at the upper part of the tank, therefore a longer series was not necessary. This secondary flow affects only the local mean velocity and it does not affects the r.m.s. velocity in the fully developed turbulence zone.

4.1.2.7 Results: FFT and Autocorrelation Experiments (5MG-FSE-FFTA):

In this section all **5MG-FSE-FFTA** results are presented. It is important to bear in mind that all measurements were taken above the grid between it and the free surface.

4.1.2.7.1 Grid Frequency Calibration:

As in the **5MG-FSE**, the parameter controlled during the experiments was the grid's frequency. This was done by controlling the voltage input to the driving motor. In order to get to know the frequency of oscillation corresponding to any voltage input value, some calibration voltage-hertz was done. The procedure was the same as in **5MG-FSE**. Frequency of oscillation was estimated in real time. Images were analyzed using Digimage software (Dalziel, 1993). Once all the experiments were analyzed for frequency estimation, a linear adjustment was made to the data (volt-hertz).

4.1.2.7.2 Mean velocity and Root Mean Square (r.m.s) Turbulent Velocity:

In Figure 4-13, the mean velocity $(\overline{u},\overline{v},\overline{w})$ and the r.m.s. turbulent velocity (u',v',w') estimated using (4-2), for each sampling point and for the three different frequencies analyzed, are plotted.

In Figure 4-14, the mean velocity $(\overline{u},\overline{v},\overline{w})$ and the r.m.s. turbulent velocity (u',v',w') for each sampling point and for the four different frequencies analyzed, are plotted in a non-dimensionalized form, using ωM as the relevant velocity scale near the grid.

Mean Velocity

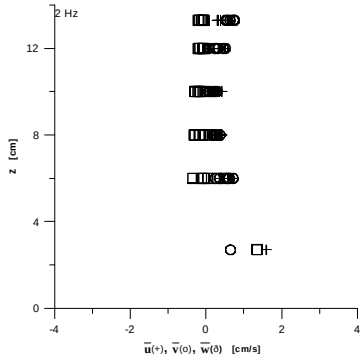

R.M.S. Velocity

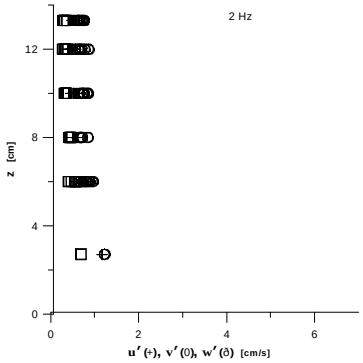

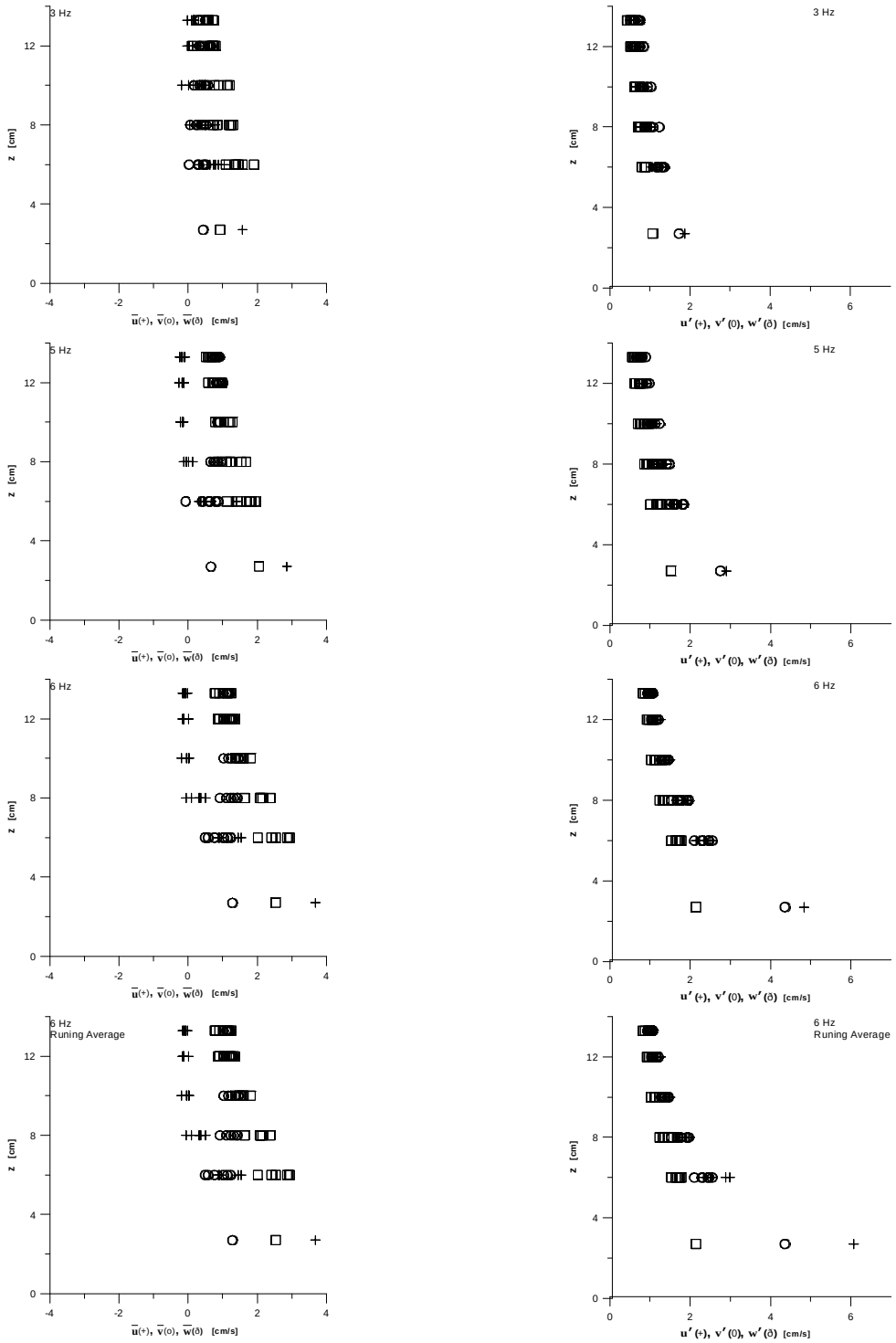

Figure 4-13.- Mean velocity and r.m.s. velocity of the FFT and autocorrelation experiments. (FSE-5MG-FFT)

Adimensionalized Mean Velocity

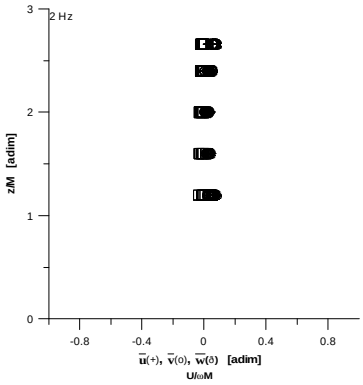

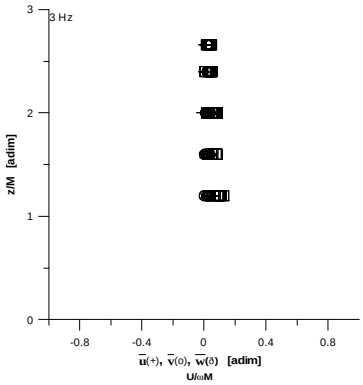

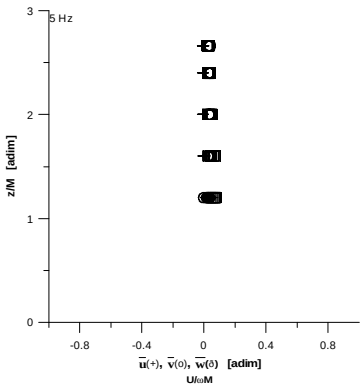

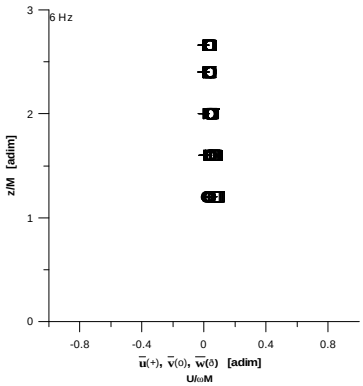

Adimensionalized R.M.S. Velocity

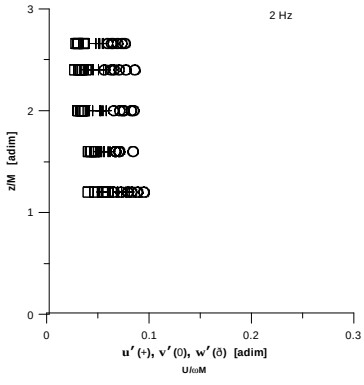

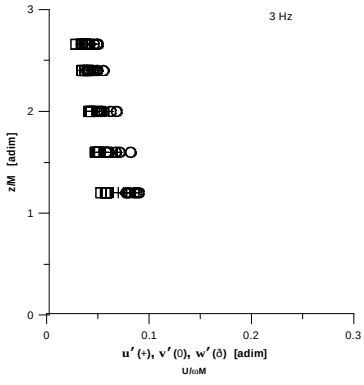

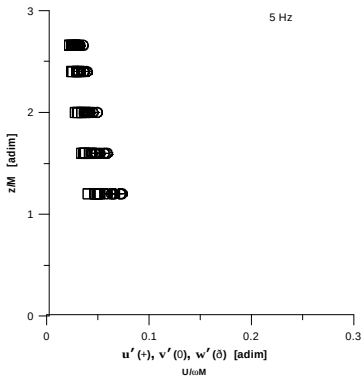

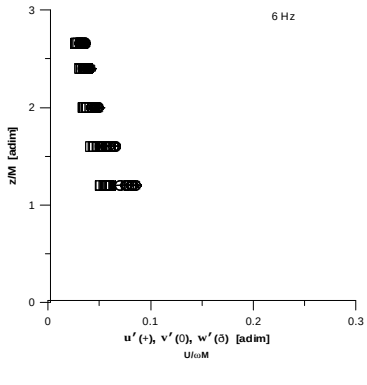

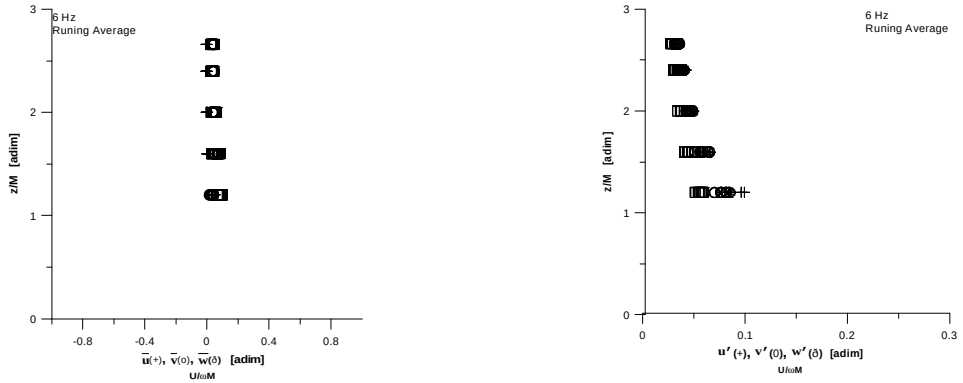

Figure 4-14.- Adimentionalized mean velocity of the FFT and autocorrelation experiments. (**FSE-5MG-FFT**)

The same observations made for Figure 4-6 and Figure 4-7 apply to Figure 4-13 and Figure 4-14, which was expected since both grids had de same characteristics. It is interesting to point out is that there is a higher dispersion of measured velocities in Figure 4-13 and Figure 4-14. This is especially true for the mean velocity, no such high dispersion is seen in the r.m.s. data. This difference between FSE-5MG and FSE-5MG-FFT could be due to the fact that the measurements taken during the FSE-5MG-FFT, unlike FSE-5MG, were taken in 5 different positions on the horizontal plane for each of the six different height sampling points. This could specially affect the mean velocity since there is no constant flow in any preferential direction. Locally, the mean flow varies constantly (see Figure 4-52 and Figure 4-53) and this is one of the most important characteristics of this experimental configuration . No constant mean flow (zero-mean-flow) is present at any point in the fully developed turbulence zone.

4.1.2.7.3 Estimation of constant c :

A value of 0.75 for constant c was found to adjust well to the measured s_u. Because of the isotropic characteristic presented in the fully developed turbulence region, where the jet-like flows disappear, this c value also adjusts to the s_v and s_w values in the turbulent region (Figure 4-15), but not so well as in the smaller tank due to the mean flow circulation both far away and close to the grid.

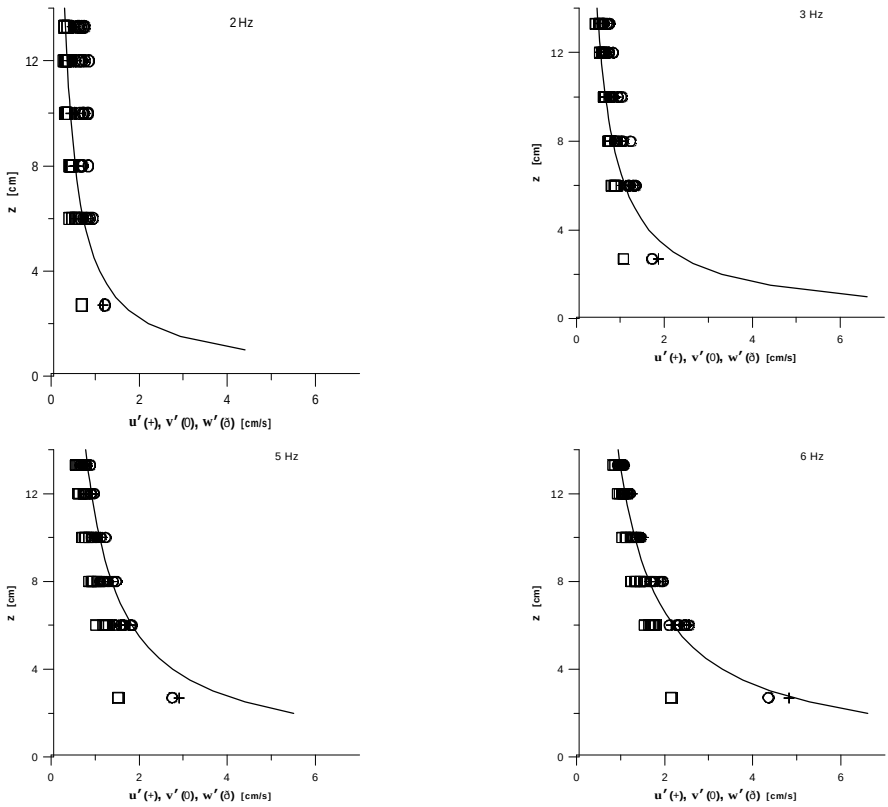

Figure 4-15.- The S_u corresponding to **FSE-5MG-FFT** is plotted with the value obtained using equation (4-1), with $c = 0.75$

4.1.2.7.4 FFT results:

The FFT results corresponding to the u component are presented next. The next four figures are the corresponding energy spectrums for each velocity measurement taken (see measurements above). As spectrums are measured farther from the grid, and as oscillating frequency increases, the energy and the slope of the inertial range increases too. This relation between Z, ω, energy and the inertial range slope remains constant until the fully developed turbulence zone is reached. After this zone, the energy decreases. The same behaviour is presented in the other two velocity components. The first spectrum in each figure is the closest one to the grid. Almost all the graphs present a peak in the lower part of the profile. This peak correspond to the frequency of the grid, that is strongly reflected near the grid in the periodic bursting jets and dipoles that further away decay and fill out the power spectra.

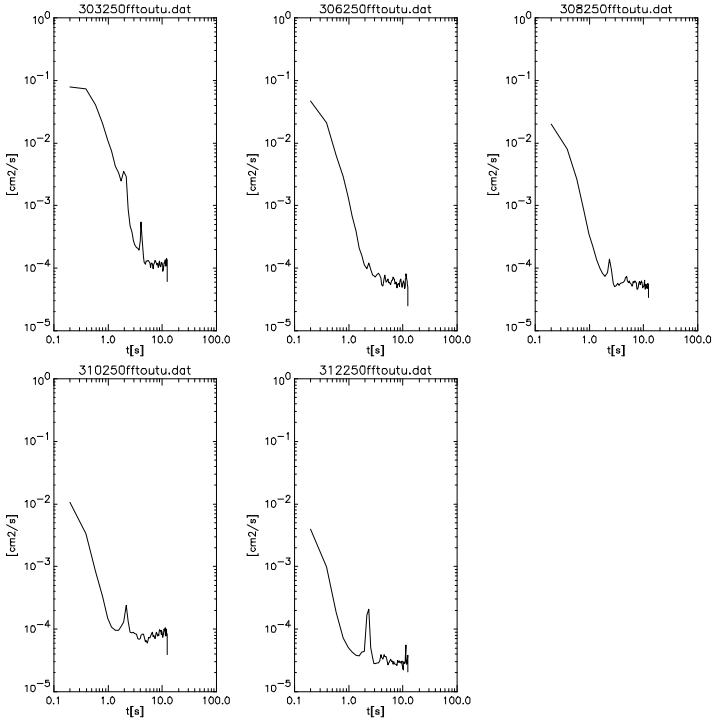

Figure 4-16.- Energy spectra for the u component at 2Hz. Measurements were taken at 2, 6, 8, 10, and 12 cm measured from the grid.

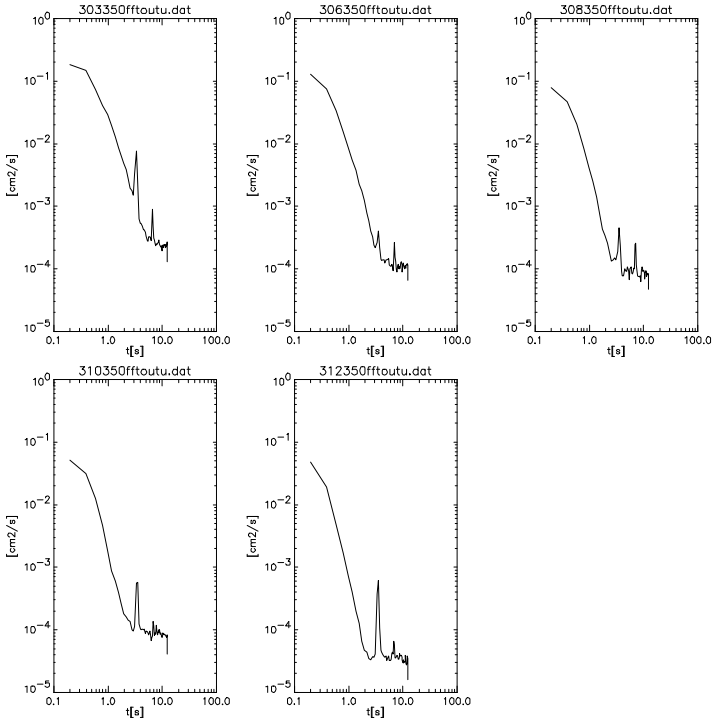

Figure 4-17.- Energy spectra for the u component at 3Hz. Measurements were taken at 2, 6, 8, 10, and 12 cm measured from the grid.

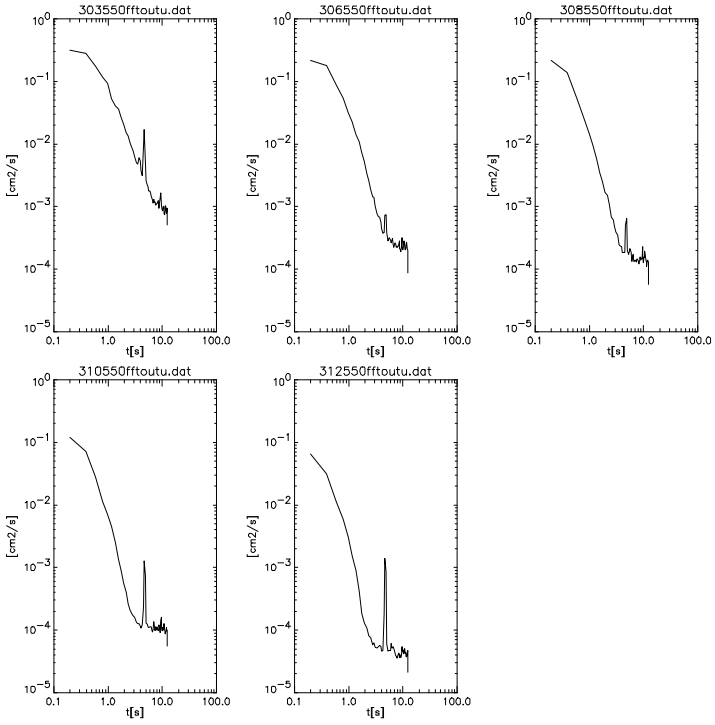

Figure 4-18.- Energy spectra for the u component at 5Hz. Measurements were taken at 2, 6, 8, 10, and 12 cm measured from the grid.

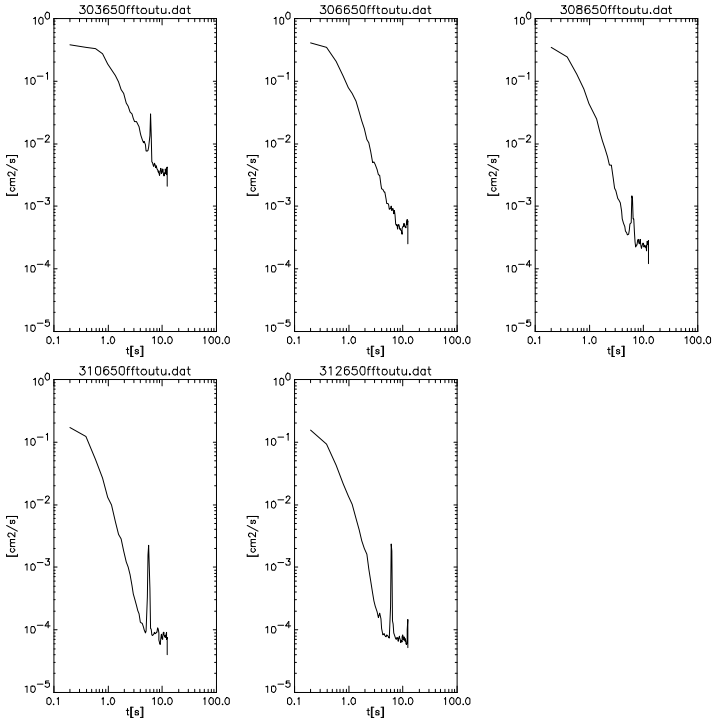

Figure 4-19.- Energy spectra for the u component at 6Hz. Measurements were taken at 2, 6, 8, 10, and 12 cm measured from the grid.

A sufficiently large (1-2 decades) spectral range is detected for the more energetic flows of grid frequencies (5-6 Hz) at more than 8.0 cm (1.6 *M*) from the grid in agreement with Hopfinger and Toly (1976).

4.1.2.7.5 Autocorrelation results:

The autocorrelation results corresponding to the u component are presented next.

The next four figures are the corresponding autocorrelation for each velocity measurement taken (see measurements above). The first autocorrelation in each figure is the closest one to the grid.

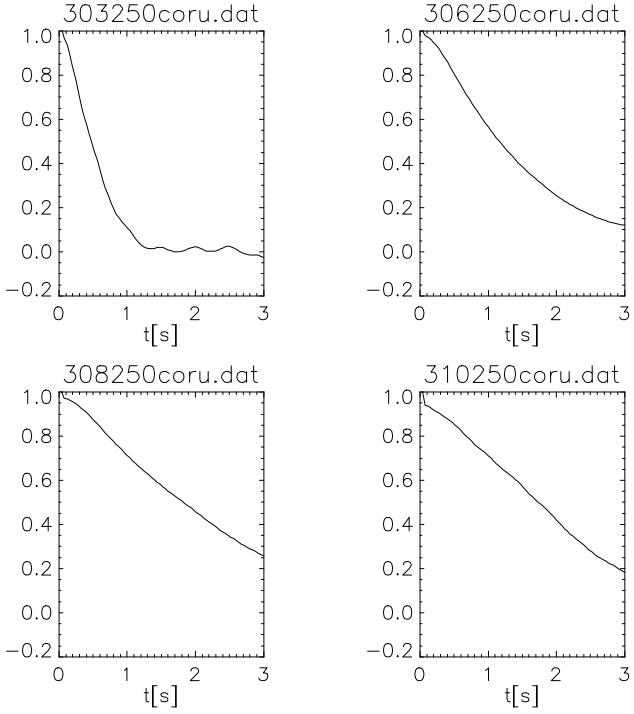

Figure 4-20.- Autocorrelation for the u component at 2Hz. Measurements were taken at 2, 6, 8, and 10 cm measured from the grid.

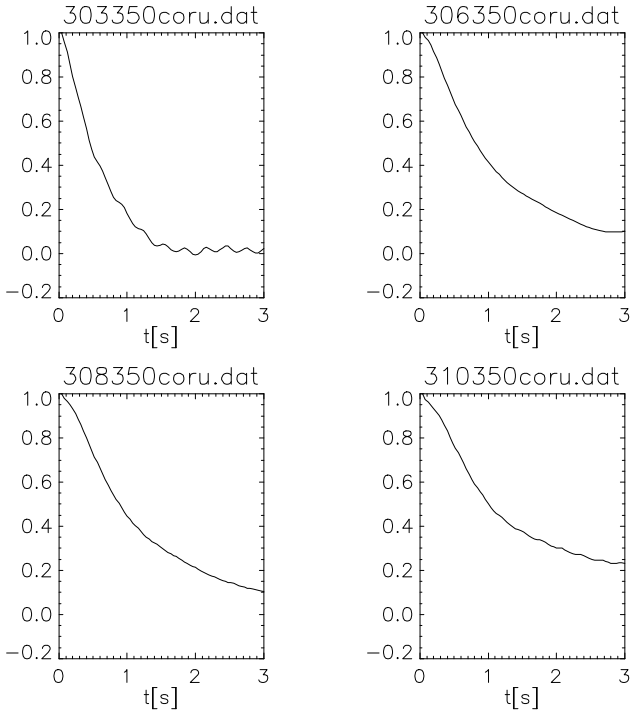

Figure 4-21.- Autocorrelation for the u component at 3Hz. Measurements were taken at 2, 6, 8, and 10 cm measured from the grid.

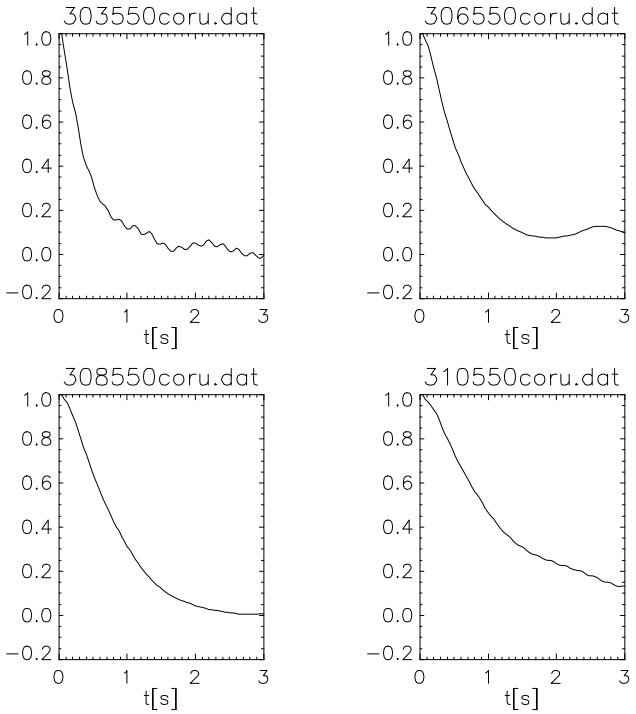

Figure 4-22.- Autocorrelation for the u component at 5Hz. Measurements were taken at 2, 6, 8, and 10 cm measured from the grid.

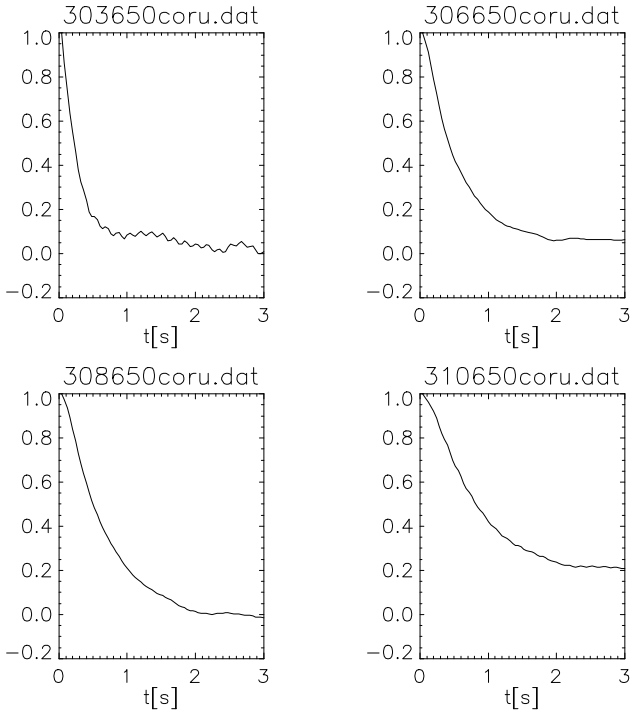

Figure 4-23.- Autocorrelation for the u component at 6Hz. Measurements were taken at 2, 6, 8, and 10 cm measured from the grid.

4.1.3 0.8 cm Mesh Grid (0.8MG) Experiments

These experiments were designed to get to know the flow near a grid of small mesh ($M = 0.8$). The idea was to design a portable configuration that could be used in the field or on board a research vessel with recently extracted cores, as described further on in this work in chapter 6 (Figure 4-24). The tank design for this purpose was a 10 x 10 x 35 cm transparent Perspex mixing box (Medina, Sánchez and Redondo, 2001). Since it was physically impossible to put the grid driving shaft and the ADV inside the small mixing box at the same time to measure the flow field as it was done both in the "5.0 cm Mesh Grid (**5MG**) Experiments" and the "FFT and Autocorrelation Experiments (**5MG-FSE-FFTA**)", a grid was mounted in the same tank used for the **5MG-FSE** so the flow could be measured using the ADV (Figure 4-3).

4.1.3.1 Grid:

The grid used was a 13.0 by 14.5 cm metal plate. The bars were 0.3 cm in horizontal section and 0.1 cm in vertical section, with 0.8 cm between centres (0.8 cm mesh (**0.8MG**)), with solidity $S = 0.61$. The grid was mounted on a chassis so it could cover one quadrant of the tank's inner section. The chassis was attached at the centre with a stainless steel rod attached at the other end to the motor eccentric drive.

4.1.3.2 Tank:

All the experiments performed with the **0.8MG** carried out in a 27.0 cm square internal cross-section, 50.0 cm height, and 0.9 cm thick walls open transparent Perspex tank (Figure 4-2).

4.1.3.3 Motor and Supporting Structure:

An electric DC motor (Mavilor-Dc Motor: Model 80, 150 Watt, 40 Volt, 5 Amp, 6000 – 10000 RPM) was used to move the grid up and down through an eccentric drive. The frequency of oscillation of the grid was controlled by limiting the voltage input to the motor. This was done with a 5-15 V power supply unit (ATAIO: Model 152a), and the voltage input to the motor was measured using a multimeter (PHILIPS: Model PM 2517 X, Volt Accuracy 0.2 ± 0.05).

The motor was mounted on an aluminium structure for support. This structure was placed surrounding the Perspex tank. The important characteristic maintained in all experiments is that the aluminium structure has no contact with the tank. This prevents most of the vibrations generated by the motor to interfere with the experiment.

The grid was attached to the eccentric drive by a stainless steel rod that ran trough a tube attached to the supporting structure. Two Teflon O-rings inside the tube guided the rod parallel to the long axis of the supporting structure. At the end, where the grid was attached, the rod had 5.0 cm of screw thread. This thread enabled us to move the grid up and down to the desired position by using two nuts, above and under the grid, allowing for the possibility of displacing the grid ± 2.5 cm. This characteristic is very useful when regulating the distance between the grid's centre of oscillation and the

sediment samples or any other specific point in which we may be interested (i.e. liquid interface, rigid boundary, sediment surface, etc.).

4.1.3.4 Acoustic Doppler Velocimeter (ADV) liquid and tracers (seeding):

The same 3D ADV measurement device used during the **5MG-FSE** was employed (see previous chapter for technical specifications). The liquid used to perform the experiments was fresh water at room temperature (23.0° ± 3.0°). To avoid ADV velocity data from looking "noisy", due to a low concentration of scatterers in the water, some seeding material was added. The seeding used during these experiments had a 10 μm particle size and the concentration used was between 10 and 50 grams per cubic meter.

4.1.3.5 Configuration of 0.8MG :

The same general configuration used by different authors like Turner (1968), Thorpe (1966), Turner (1973), Thompson and Turner (1975), Hopfinger and Toly (1976), Xuequan and Hopfinger (1987), Tsai and Lick (1987), Noh and Fernando (1991), Huppert, Turner, and Hallworth (1995), Redondo, Sánchez, Castilla (1995), Peters and Redondo (1997), Sánchez and Redondo (1998), Redondo and Sánchez (1999), Mann, Ott and Andersen (1999), Ott and Mann (2000), Redondo and Sánchez (2000), Matas and Redondo (2000), was employed. The grid was placed horizontally at mid depth so it could oscillate vertically as far as possible from the bottom and the free surface. The water depth was of 40.0 cm. The stroke s (amplitude of oscillation) was fixed at 1.2 cm.

The tank was fitted into the engine support frame in a vertical position. The ADV was placed vertically in the tank parallel to the driving shaft at the mid-point between the shaft and a corner of the tank. The shaft was placed at the centre of the tank. It was possible to change the vertical position of the ADV by extending the ADV support structure.

As mentioned above, the grid did not cover the whole inner cross section of the tank but only one quadrant, and it had to be mounted on a chassis to support it.

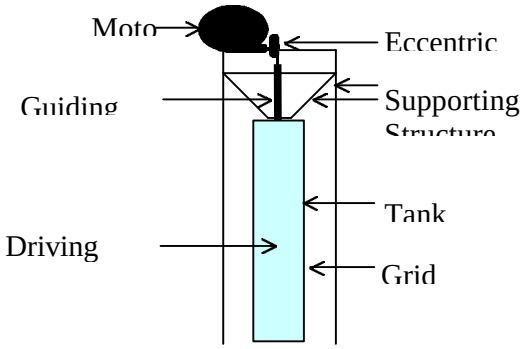

Figure 4-24.- Schematic drawing of the tank used for the **0.8MG-FSE**.

4.1.3.6 Measurements:

One set of measurements was carried out at 4.25 Hz. Measurements where taken at 15 sampling points, 14 of which where separated 0.5 cm in vertical, and the 15th sampling point was positioned at 2.95 cm from the grid's centre of oscillation. This last sampling point was selected because, as it is going to be seen later on in this work, some experiments dealing with sediment cores had this distance between the grid's centre of oscillation and the core surface.

4.1.3.7 Results: Free Surface, 0.8cm Mesh Grid (FSE-0.8MG)

In this section all of the FSE-0.8MG results are presented. It is important to bear in mind that all measurements were taken on top of the grid between it and the free surface. Care was taken to place the ADV sampling volume exactly above the centre of the grid to avoid as much as possible the effect of the chassis.

4.1.3.7.1 Grid Frequency Calibration:

The parameter controlled during the experiments was the grid's frequency. This was done by controlling the voltage input to the driving motor. In order to find out the frequency of oscillation corresponding to any voltage input value, some calibration voltage-hertz was done.

Some of the experiments were recorded in video tape and the frequency was estimated from the recordings. For non-recorded experiments, frequency of oscillation was estimated in real time. In both cases, the images were analyzed using a software package specially designed for fluid dynamic experiments (Digimage) (Dalziel, 1993). This software operates using a Data Translation Card DT-2861 on a P.C. computer.

The tank was lit from behind and the experiments recorded using a compact PAL system VHS-C colour video camera (JVC, GR-AX200). The images were manipulated with the facilities provided by Digimage. The frequency of oscillation of the grid is measured directly from the digitized images. A typical image showing the grid's movement in time is presented in Figure 4-4. This figure is a time series where time is in X-axis and distance (grid displacement) is in Y-axis. The oscillation of the grid is seen as an oscillatory uniform signal. Image is made up by 512 pixels in both directions (512 columns and 512 rows). Each column, 1 pixel width, is captured at a pre-specified time span (during these experiments the time interval was of 0.04s), and during a pre-establish acquisition time (Figure 4-4, the same kind of images were taken for the 0.8MG). Thus, a time series at a specific vertical position is created.

Once all the experiments were analyzed for frequency estimation, a linear adjustment was made to the data (volt-hertz). This enabled us to find out the frequency of oscillation corresponding to the voltage input at any time during further experiments.

Two different adjustments where made. The first one for the grid mentioned above and with which these experiments where done. The second one was using the same 0.8MG but inside the portable mixing box mentioned at the beginning of this section which was used in further experiments with actual sediment.

First adjustment result:

$$Hz = 0.9886V - 0.0634 \quad (4\text{-}3)$$

Second adjustment result (portable configuration):

$$Hz = 2.6279V - 6.8847 \quad (4\text{-}4)$$

For the second calibration, an important thing to mention is that after 6.37Hz, the grid reaches a constant frequency. This means that even if there is more voltage input to the motor the frequency of oscillation does not change. This is due to the grid's drag and the geometrical characteristics of the experimental configuration.

4.1.3.7.2 Mean velocity and Root Mean Square (r.m.s) Turbulent Velocity:

In Figure 4-25, the mean velocity $(\bar{u}, \bar{v}, \bar{w})$ and the r.m.s. turbulent velocity (u', v', w') for each sampling point and for the four different frequencies analyzed, are plotted.

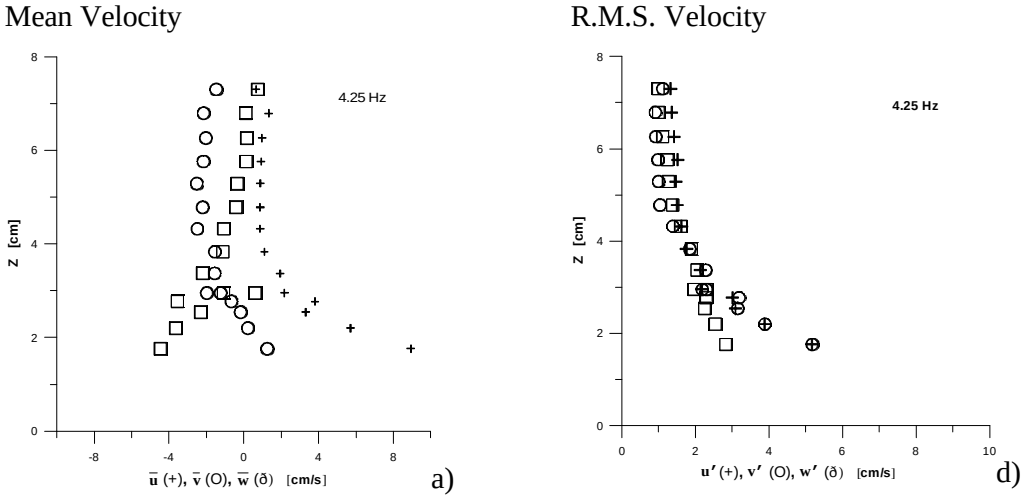

Figure 4-25.- Mean velocity and r.m.s. turbulent velocity. (FSE-0.8MG)

In Figure 4-26, the mean velocity $(\bar{u}, \bar{v}, \bar{w})$ and the r.m.s. turbulent velocity (u', v', w') for each sampling point and for the three different frequencies analyzed, are plotted in a non-dimensionalized form, using ωM as the relevant velocity scale near the grid.

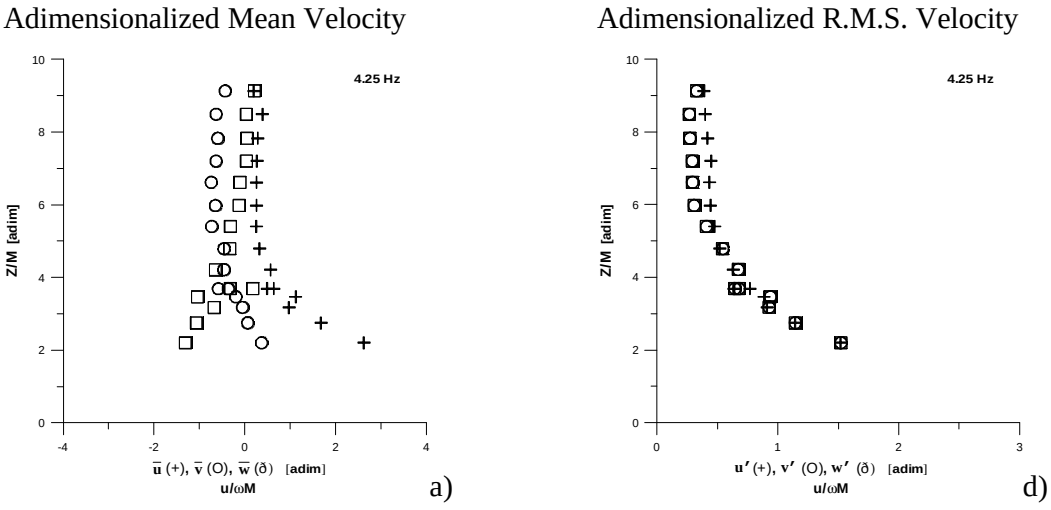

Figure 4-26.- Adimensionalized mean velocity and r.m.s. turbulent velocity. (FSE-0.8MG)

As seen, the mean velocity is nearly zero except close to the grid. This was to be expected, as mention before in this work, a quasi-steady jet-flow generates close to each grid bar (Thomson and Turner, 1975). After a certain distance, jets interact, and break to give turbulence which is advected by the jets. After turbulence is generated, no mean flow, or at least no steady mean flow is present, as expected (see section 4.4).

From a distance where the different $\bar{u}$ and u' merge, turbulence is fully developed and starts to decay. This point corresponds, in Figure 4-25 and Figure 4-26, to a distance of about 2.6 cm from the centre of oscillation or 3.3 meshes. For the u' graphs, after this point, the values of the three components are very similar. This confirms the isotropic ($u' \cong v' \cong w'$) characteristic of the generated turbulence.

4.1.3.7.3 Estimate of constant c :

A value of 0.6 for constant c was found to adjust well to the measured s_u. Because of the isotropic characteristic present in the fully developed turbulence region, where the jet-like flows disappear, this c value also adjusts well to the s_v and s_w values in the turbulent region (Figure 4-27).

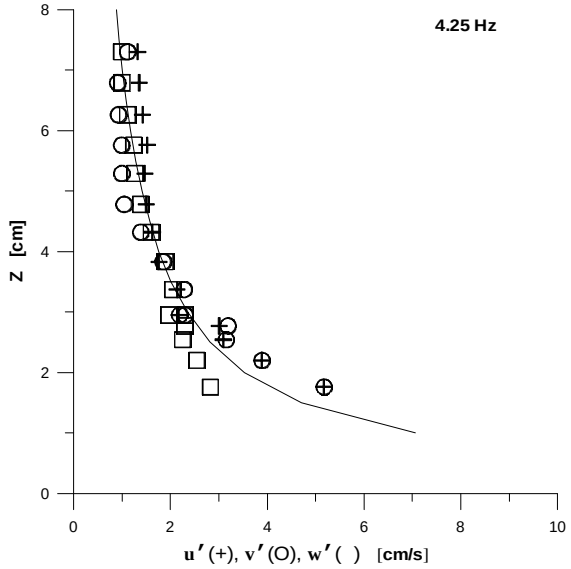

Figure 4-27.- The s_u corresponding to **FSE-0.8MG** is plotted with the value obtained using equation (4-1), with $c = 0.6$

4.2 Solid Boundary Experiments (SBE)

4.2.1 Flow characterization (SBFE)

This set of experiments was designed to measure the flow characteristics between the grid and a rigid boundary, as close as possible to the boundary (e.g. between the grid and the bottom of the tank), unlike that for the **FSE**. The general configuration that was used for the **FSE** had to be modified in order to be able to measure the flow with the ADV. Basically, the difference consisted in placing the grid in a vertical position instead of horizontally in order to introduce the ADV sensor between the grid and the boundary. Further explanations are given in this section.

4.2.1.1 Grid:

The grid used was a 1.0 cm of square section plastic solid bars with 5.0 cm between centres (M = 5.0 cm (**5MG**)) (Figure 4-1) like the one used in the **5MG-FSE**.

The grid was attached at the centre with a stainless steel rod attached at the other end to the motor eccentric drive (See Motor and Supporting Structure further in this

chapter). The lower end of the rod had 5 cm of screw thread. This thread allows to position the grid vertically at the required distance from the wall.

4.2.1.2 Tank:

All the **SBE** where carried out in a 27.0 cm square internal cross-section, 50.0 cm height, and 0.9 cm thick walls open transparent Perspex tank. This tank is the same used for the **5MG-FSE.** The difference between both experiments will be explained in the configuration section.

4.2.1.3 Motor and Supporting Structure:

An electric DC motor (Mavilor-Dc Motor: Model 80, 150 Watt, 40 Volt, 5 Amp, 6000 – 10000 RPM) was used to move the grid up and down through an eccentric drive. The frequency of oscillation of the grid was controlled by limiting the voltage input to the motor. This was done with a 5-15 V power supply unit (ATAIO: Model 152a), and the voltage input to the motor was measured using a multimeter (PHILIPS: Model PM 2517 X, Volt Accuracy 0.2 ± 0.05). The motor was mounted on a new aluminium structure built specially for this experiment.

The grid was attached to the eccentric drive by a stainless steel rod that ran through a tube fixed to the supporting structure. Two Teflon O-rings inside the tube guided the rod parallel to the long axis of the supporting structure. At the end, where the grid was attached, the rod had 5.0 cm of screw thread. This thread enabled us to move the grid up and down to the desired position by using two nuts, above and under the grid, allowing for the possibility of displacing the grid ± 2.5 cm. This characteristic is very useful when regulating the distance between the grid's centre of oscillation and the boundary where we are measuring.

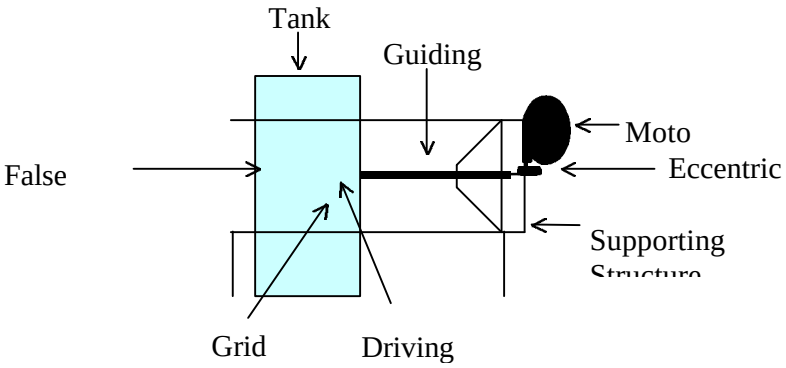

Figure 4-28.- Schematic drawing of supporting structure and relative position of the tank (**SBFE**).

4.2.1.4 Acoustic Doppler Velocimeter (ADV) liquid and tracers (seeding):

The velocity measurement device used during the experiments was the same 3D ADV used in all the **FSE** described above. The liquid used to perform the experiments was fresh water at room temperature (23.0° ± 3.0°). It was plain tap water and no filtering was carried out, although, the amount of suspended particles was very low. This can become a problem if an acoustic device is going to be used to measure velocities in the fluid.

The seeding used during these experiments was obtained directly from Nortek AS Company. The particle size was 10 μm and the concentration used was between 10 and 50 grams per cubic meter, see the general description at chapter 3.

4.2.1.5 Configuration of SBFE :

The grid was placed vertically at 13.3 cm from the boundary. The water depth was 40.0 cm. The stroke, s, (amplitude of oscillation), was fixed at 1.2 cm as in all previous experiments.

The tank was fitted into the engine support frame in a vertical position, but the supporting structure, unlike all the **FSE**, was placed horizontally. The driving shaft penetrates the tank through a perforation located at the centre of one of the tank walls. Unlike the previous cases described above, the ADV was positioned in the tank at an angle of 33° from vertical. This was done to ensure measuring as close as possible to the boundary. It was possible to vary the horizontal position of the ADV by sliding the ADV support structure over a guiding rod attached to the floor.

This new position of the ADV and the grid, made it necessary to rotate the values measured by the ADV to the vertical and horizontal reference planes. In addition to this, because the grid is in a vertical position and oscillates horizontally, the v and x measured components correspond to the u and w directions respectively (Figure 4-29) in the experimental configuration where the vertical direction is considered parallel to the grid's direction of oscillation.

4.2.1.6 Measurements:

Time series of velocity were taken with 4 different oscillating frequencies, w, (2.58, 3.96, 5.33, and 6.70 Hz), at 16 positions between the grid's centre of oscillation and the solid boundary (0.00, 0.20, 0.40, 0.60, 0.80, 1.00, 1.20, 1.40, 1.60, 1.80, 2.00, 2.50, 3.00, 3.50, 4.00 and 4.50 cm measured from the boundary to the grid; or 8.80, 9.30, 9.80, 10.30, 10.5, 10.80, 11.30, 11.50, 11.70, 11.90, 12.10, 12.30, 12.50, 12.70, 12.90, and 13.30 cm measured from the grid to the boundary). Time series were taken during a period of 5 minutes at the highest possible sampling frequency of the ADV (25 Hz). This gave a total of 64 data sets made up by of 7500 data points each.

It was necessary to rotate the data sets obtained, from the ADV's reference coordinates (displaced 33° from vertical), to the experimental configuration reference coordinates (Figure 4-29). Since the rotation was made using the component parallel to the boundary (and grid) plane as reference , v, the components that were rotated were the ADV measured u and w as:

$$u_{\text{experimental configuration}} = u_{\text{ADV measured}} \sin(-33) \quad (4\text{-}5)$$

$$w_{\text{experimental configuration}} = u_{\text{ADV measured}} \cos(-33) \quad (4\text{-}6)$$

and

$$v_{\text{experimental configuration}} = v_{\text{ADV measured}} \quad (4\text{-}7)$$

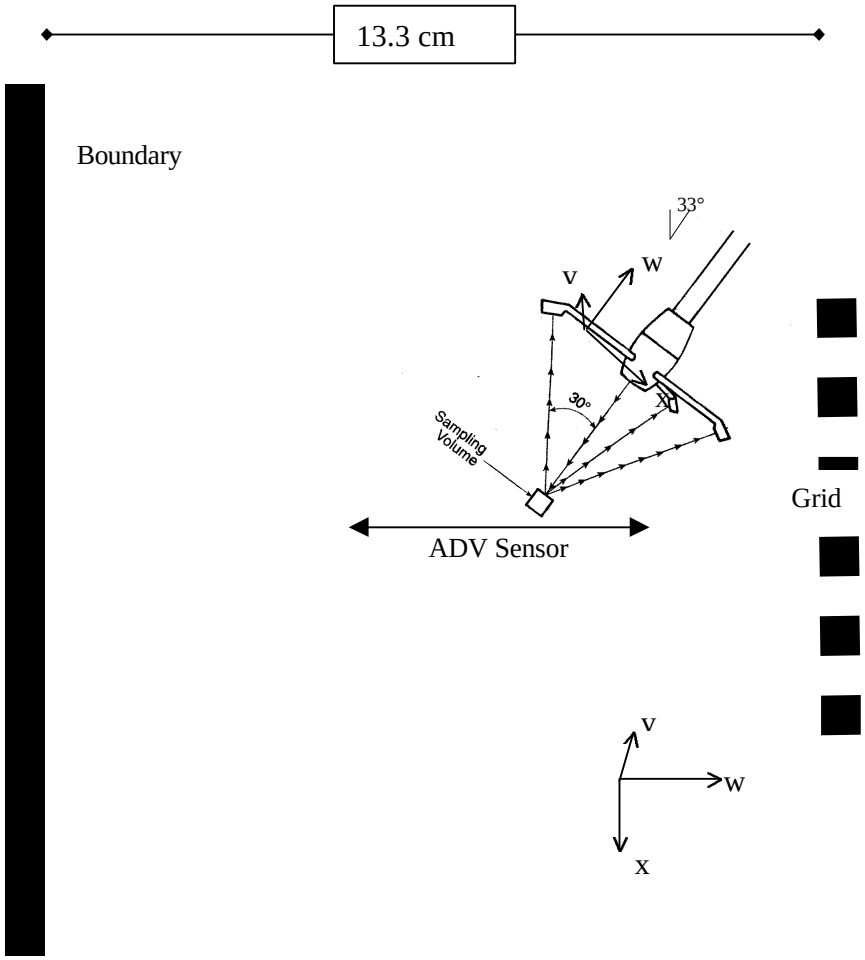

Figure 4-29.-Schematic drawing of the experimental configuration for the **SBFE.**

4.2.1.7 Results: Solid Boundary Flow Experiments (SBFE):

In this section all **SBFE** results are presented. It is important to bear in mind that all measurements were taken between the grid and the solid boundary, and that the wall at the other side of the grid was close to it (7 cm from centre of oscillation). This characteristic produced a strong secondary flow on this side of the grid, which passed through the grid to the other side. This represents an extra source of mean flow and turbulence that has to be taken into account when analysing the results.

4.2.1.7.1 Grid Frequency Calibration:

The parameter controlled during the experiments was the grid's frequency. This was done by controlling the voltage input into the driving motor. In order to get to know the frequency of oscillation corresponding to any voltage input value, some calibration voltage-hertz was done.

Frequency of oscillation was estimated in real time. Images were analyzed using Digimage software package specially designed for fluid dynamic experiments (Dalziel, 1993). This software operates using a Data Translation Card DT-2861 on a P.C. computer.

The tank was lit from behind and the experiments recorded using a compact PAL system VHS-C colour video camera (JVC, GR-AX200). The images were manipulated with the facilities provided by Digimage. The frequency of oscillation of the grid is measured directly from the digitized images. A typical image showing the grid's movement in time is presented in Figure 4-4. This figure is a time series where time is in X-axis and distance (grid displacement) is in Y-axis. The oscillation of the grid is seen as an oscillatory uniform signal. Image made up by 512 pixels in both directions (512 columns and 512 rows). Each column, 1 pixel width, is captured at a pre-specified time span (during these experiments the time interval was of 0.04s), and during a pre-establish acquisition time (Figure 4-4). Thus, a time series at a specific vertical position is created.

Once all the experiments were analyzed for frequency estimation, a linear adjustment was made to the data (volt-hertz). This enabled us to get to know the frequency of oscillation corresponding to the value of voltage input at any time during further experiments. The result of this linear adjustment is presented in Figure 4-30.

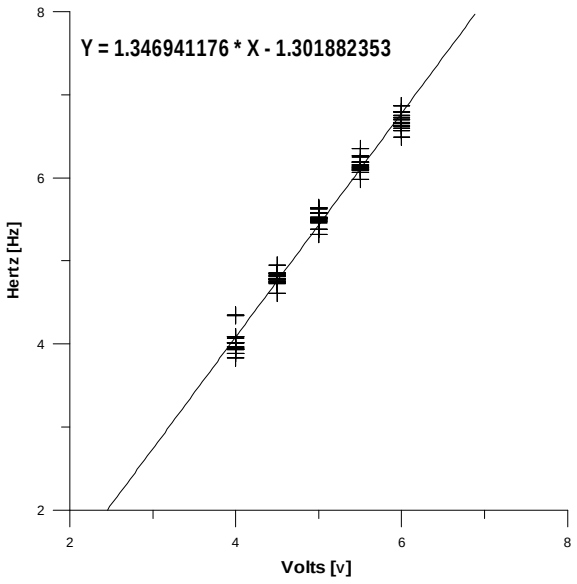

Figure 4-30.- Voltage input Vs. Frequency of Oscillation. **SBFE.**

4.2.1.7.2 Mean Velocity and Root Mean Square (r.m.s) Turbulent Velocity:

In Figure 4-31, the mean velocity $(\bar{u},\bar{v},\bar{w})$ and the r.m.s. turbulent velocity (u',v',w') estimated using **(4-2)** for each sampling point and for the four different frequencies analyzed, are plotted.

In Figure 4-32, the mean velocity $(\bar{u},\bar{v},\bar{w})$ and the r.m.s. turbulent velocity (u',v',w') for each sampling point and for the four different frequencies analyzed, are plotted in a non-dimensionalized form, using ωM as the relevant velocity scale near the

grid. In this figure, the Y axis represents an adimensionalized distance using as reference the position of the grid.

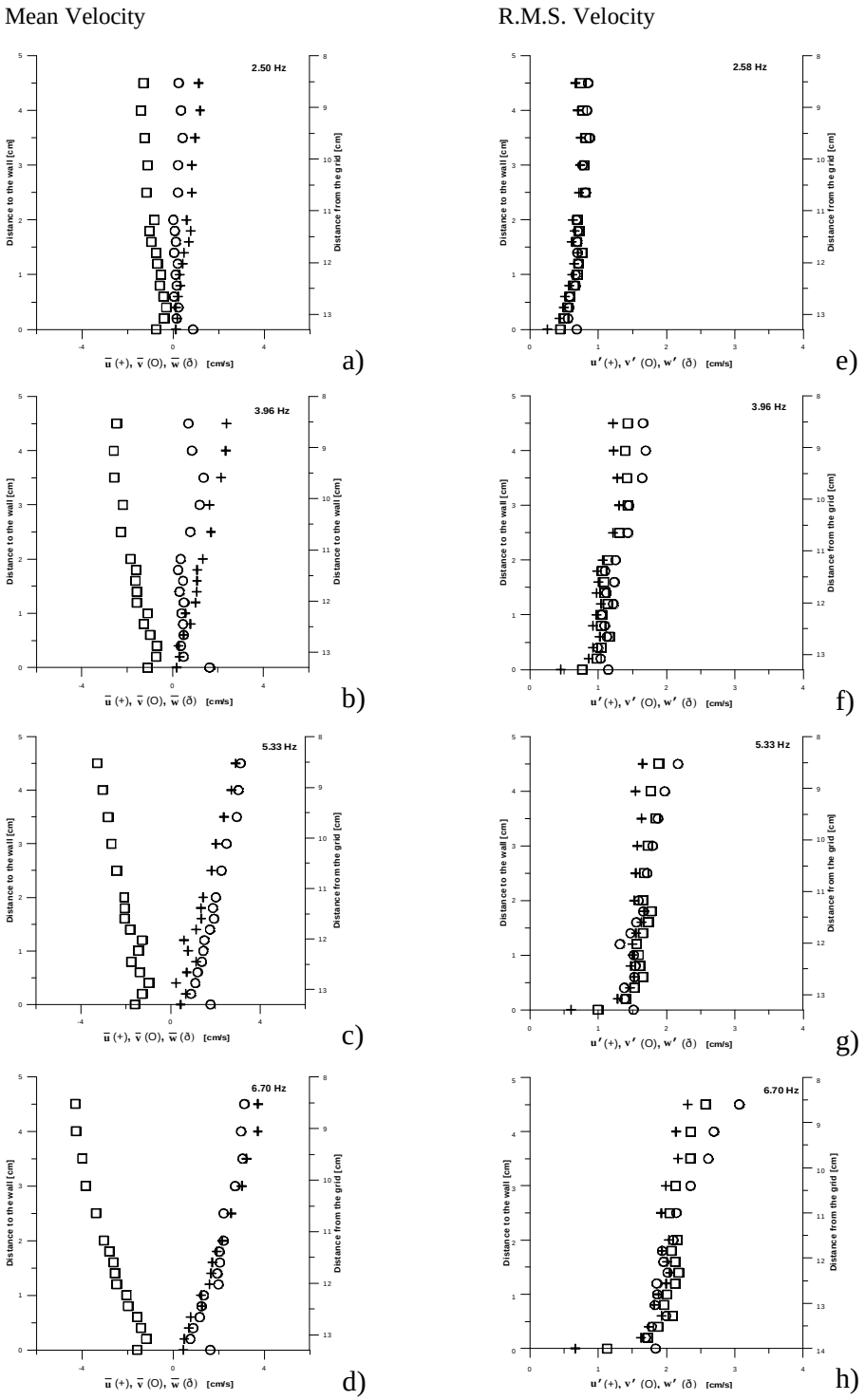

Figure 4-31.- Mean velocity and r.m.s. turbulent velocity. (**SBFE**)

In Figure 4-33, the mean velocity $(\bar{u},\bar{v},\bar{w})$ and the r.m.s. turbulent velocity (u',v',w') for each sampling point and for the four different frequencies analyzed, are plotted in a non-dimensionalized form, using ωM as the relevant velocity scale near the grid. In this figure, the Y axis represents an adimensionalized distance using as reference the position of the wall.

In Figure 4-31 (a, b, c, d), Figure 4-32 (a, b, c, d) and Figure 4-33 (a, b, c, d) we can see that the mean flow is stronger near the grid. This is a composed effect produced by the superposition of the flow generated at the other side of the grid due to the proximity of the wall as mention before, and the effect of the jet-like flow produced by the grid oscillation. This mean flow decreases with distance from the grid and has a tendency to a value near zero in close proximity to the solid boundary. The former is especially true for the module of components u and v but, for the w component, this value near the wall is greater as frequency of oscillation increases. In this case the mean flow increases and the value of the w component close to the solid boundary is each time greater, while the other two components remain at about the same value. This effect is generated by the increase of the secondary flow at the other side of the grid.

During the **FSE-5MG** we noticed that the mean flow was almost zero at about Z/M=1.6 (8 cm from the grid). In the **SBFE** a mean flow persists from this point on. As in the other experiments, the general tendency is to decrease with distance from the grid, reaching a value near zero close to the solid boundary.

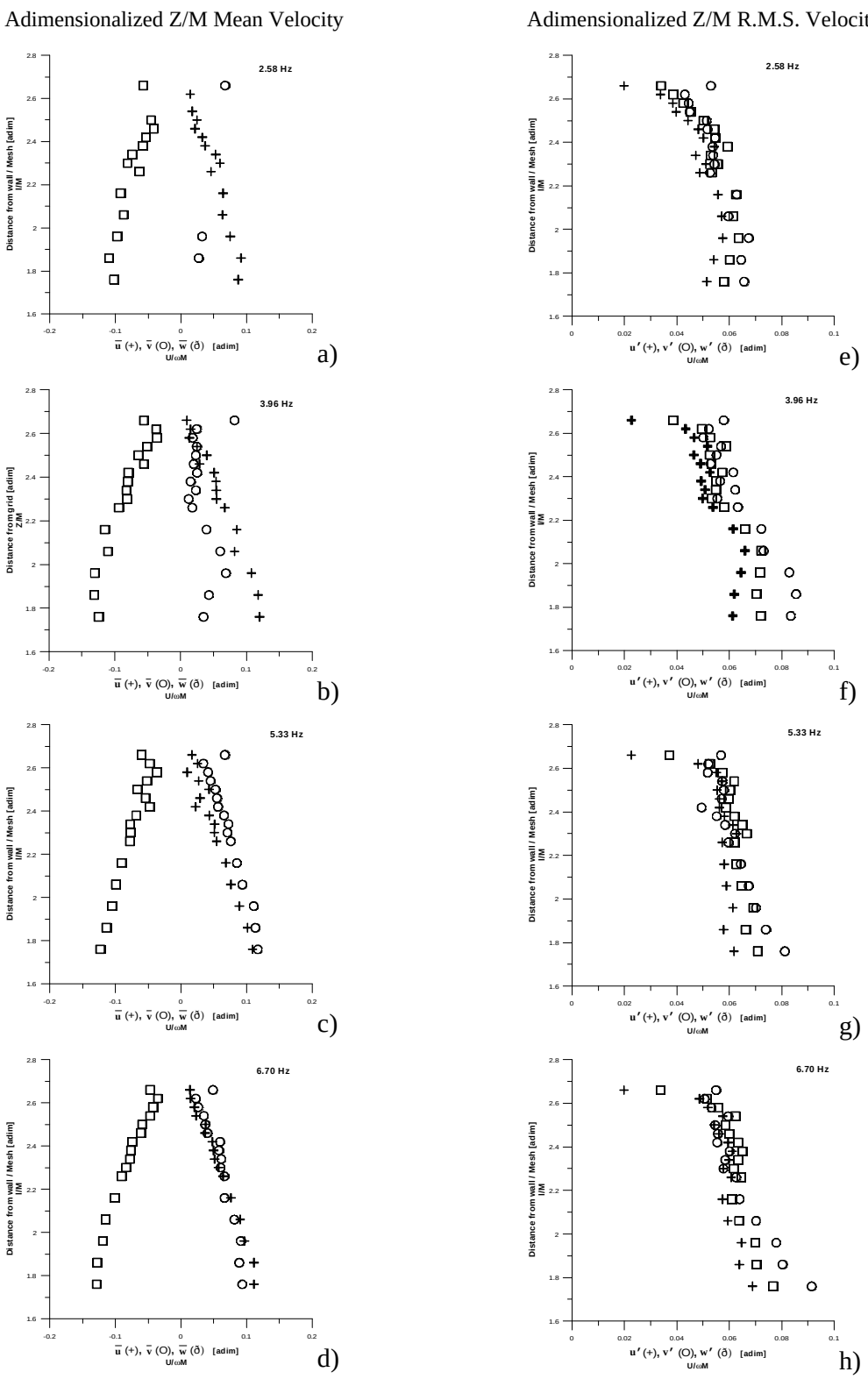

Figure 4-32.- Adimensionalized mean velocity and r.m.s. turbulent velocity. (**SBFE**)

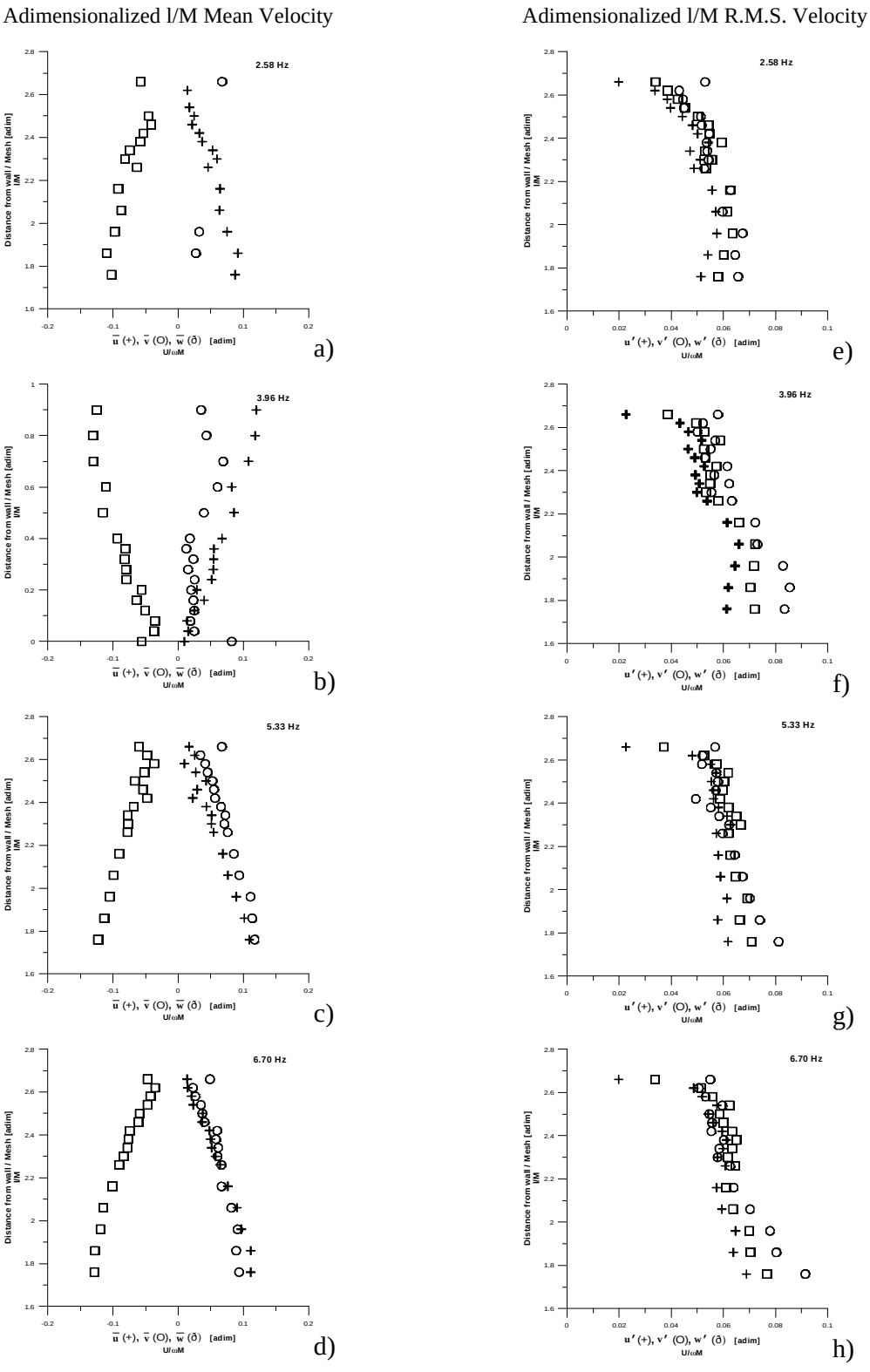

Figure 4-33.- Adimensionalized mean velocity and r.m.s. turbulent velocity. (**SBFE**)

All three components of velocity had about the same module value seen in the last three figures. Nevertheless, the $\overline{w}$ component has a negative value in all the measurements taken. This means there is a flow toward the solid boundary coming from the grid. This last statement and the fact that the value of this component near the solid boundary is always greater than the other two, are probably the most clear effects of the flow generated at the other side of the grid.

Probably the most relevant characteristic about the r.m.s. turbulent velocity in Figure 4-31 (e, f, g, h), Figure 4-32 (e, f, g, h) and Figure 4-33 (e, f, g, h) is that it behaves exactly the same way as in the **FSE-5MG**, and the flow at the other side of the grid seems not to have any relevant influence on the r.m.s. velocity. The only difference between the results of these experiments and of those obtained for the **FSE-5MG** is that the values of the three components do not merge at Z/M = 1.6 (8 cm from the grid), instead they merge at about Z/M = 2.2 (11 cm from the grid). This could be the only effect of the flow generated at the other side of the grid over the r.m.s. velocity.

4.2.1.7.3 Estimate of constant c :

A value of constant c was found to adjust well to the measured s_u close to the solid boundary. Because of the isotropic characteristic presented in the fully developed turbulence region, where the jet-like flow disappear, this c value adjusts as well for the s_v and s_w values in the turbulent region near the wall (Figure 4-34).

The difference found between these results and those corresponding to the **FSE-5MG** or the **FSE-0.8MG**, is that for these results the constant c is not constant for all grid frequencies (Ω) analyzed. Constant c increases as Ω increases. This is attributed, once again, to the secondary flow at the other side of the grid, which, when passing through the grid towards the solid boundary under study, generates another source of turbulence. This is stronger as the secondary flow grows stronger. From that point on, the general behaviour of the flow is the same as in all other experiments performed before. This is the reason why equation (4-1) gives a good fit near the wall where full developed turbulence is present.

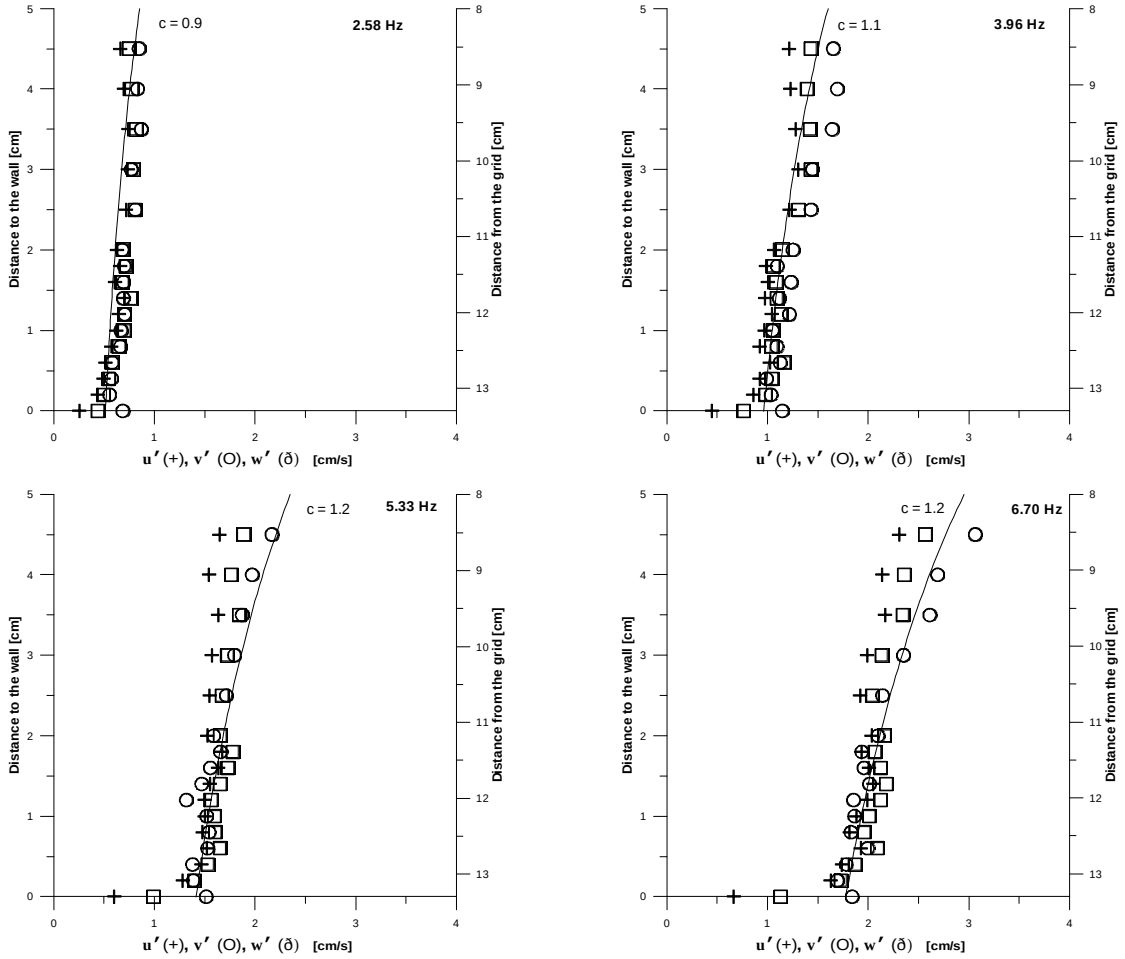

Figure 4-34.- The r.m.s. corresponding to **SBFE** is plotted with the value obtained using equation **(4-1)** with $C \propto \omega$. As ω increases c increases.

4.2.1.7.4 FFT results:

The FFT results for the u component are presented next. The same general observations made for the FFT results corresponding to the **5MG-FSE-FFTA** could be made to these results, meaning that above the grid (**5MG-FSE-FFTA**) and below it the behaviour of the energy spectrum remains the same. The next four figures are the corresponding spectrums for each velocity measurement taken (see measurements above). The first spectrum in each figure is the closest one to the boundary.

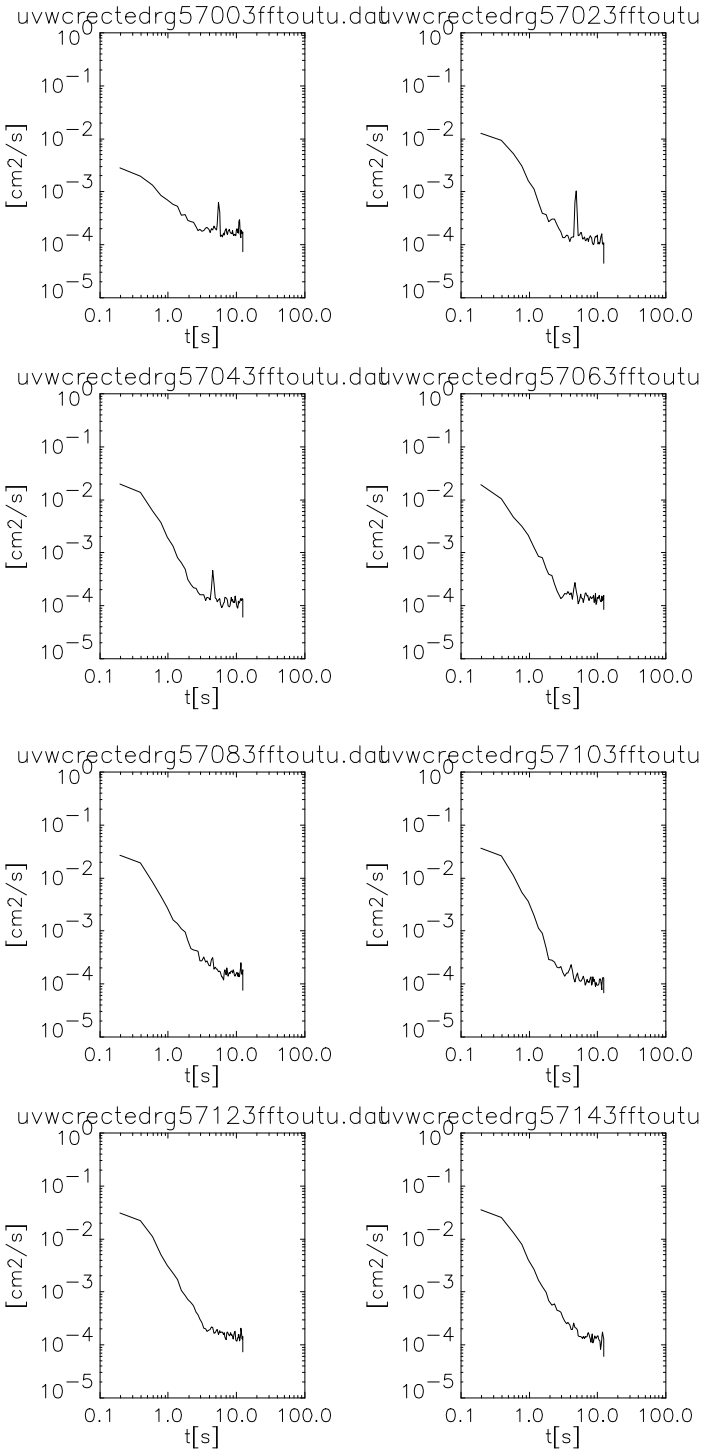
uvwcrectedrg57003fftoutu.dat
uvwcrectedrg57023fftoutu
uvwcrectedrg57043fftoutu.dat
uvwcrectedrg57063fftoutu
uvwcrectedrg57083fftoutu.dat
uvwcrectedrg57103fftoutu
uvwcrectedrg57123fftoutu.dat
uvwcrectedrg57143fftoutu
[cm2/s]
t[s]
0.1
1.0
10.0
100.0

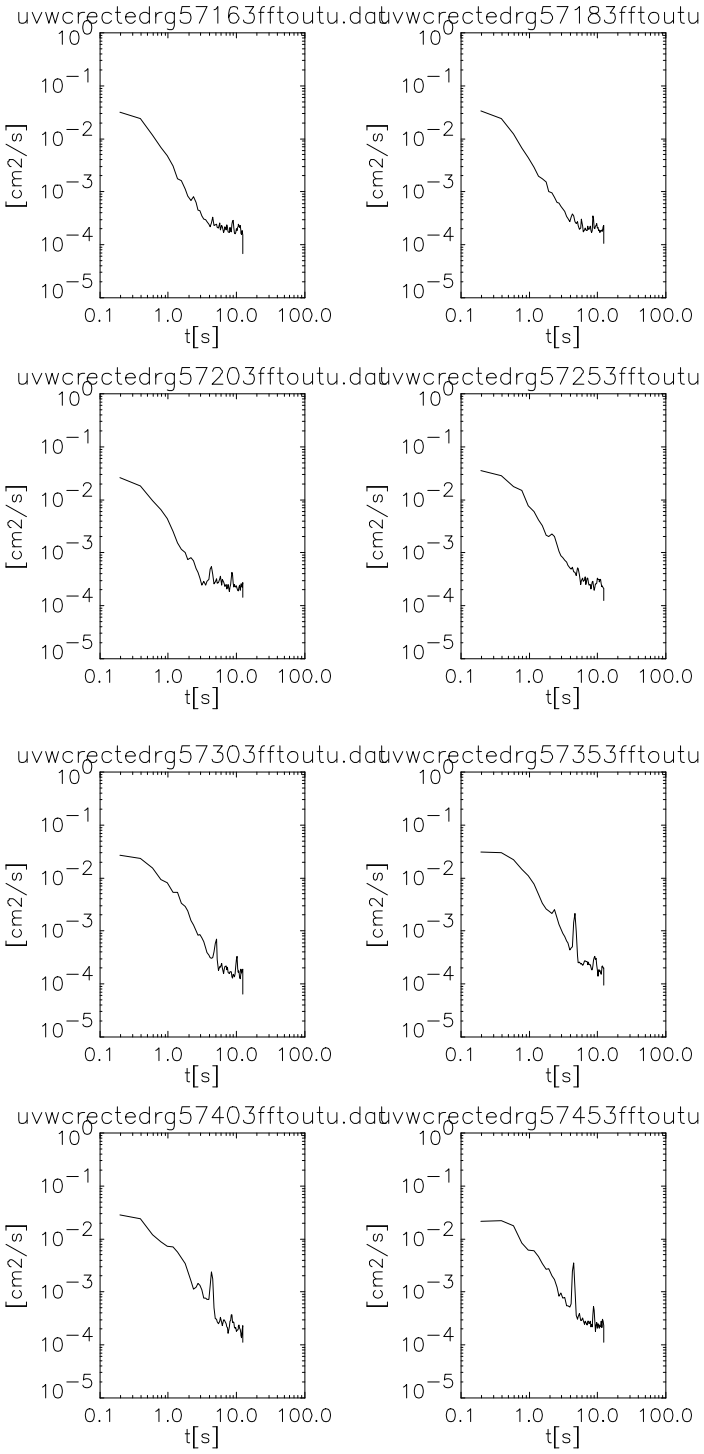

Figure 4-35.- Energy spectra for the u component at 3Hz. Measurements were taken at 0.00, 0.20, 0.40, 0.60, 0.80, 1.00, 1.20, 1.40, 1.60, 1.80, 2.00, 2.50, 3.00, 3.50, 4.00 and 4.50 cm measured from the boundary to the grid

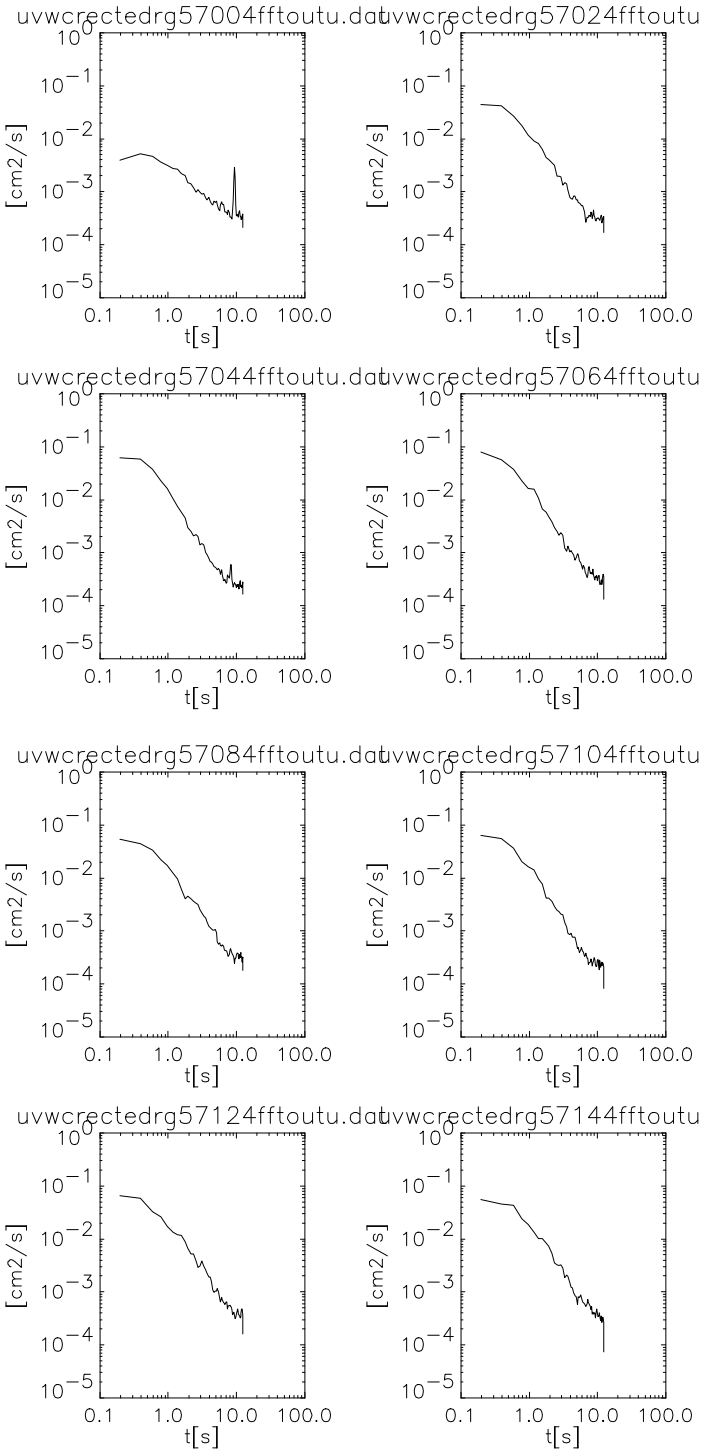
uvwcrectedrg57004fftoutu.dat
uvwcrectedrg57024fftoutu
uvwcrectedrg57044fftoutu.dat
uvwcrectedrg57064fftoutu
uvwcrectedrg57084fftoutu.dat
uvwcrectedrg57104fftoutu
uvwcrectedrg57124fftoutu.dat
uvwcrectedrg57144fftoutu
[cm2/s]
t[s]
0.1
1.0
10.0
100.0

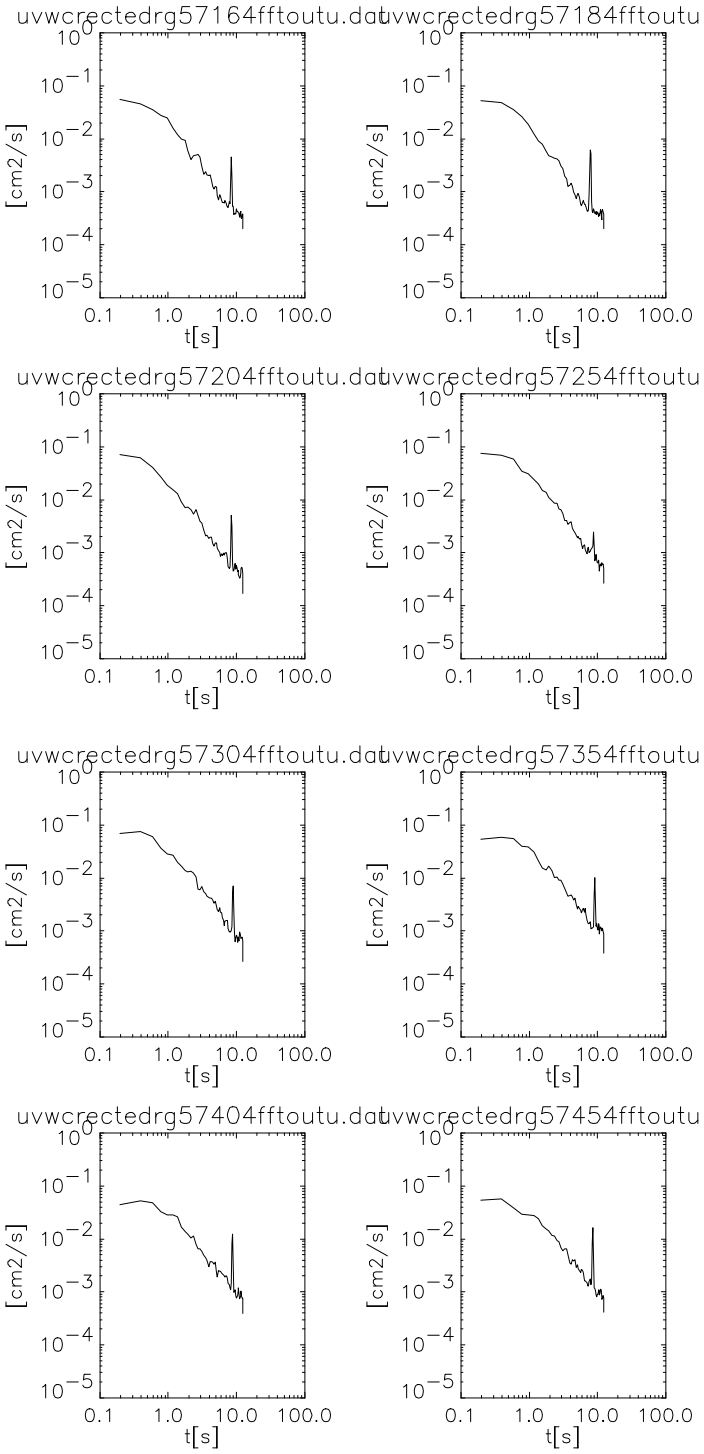

Figure 4-36.- Energy spectra for the u component at 4Hz. Measurements were taken at 0.00, 0.20, 0.40, 0.60, 0.80, 1.00, 1.20, 1.40, 1.60, 1.80, 2.00, 2.50, 3.00, 3.50, 4.00 and 4.50 cm measured from the boundary to the grid

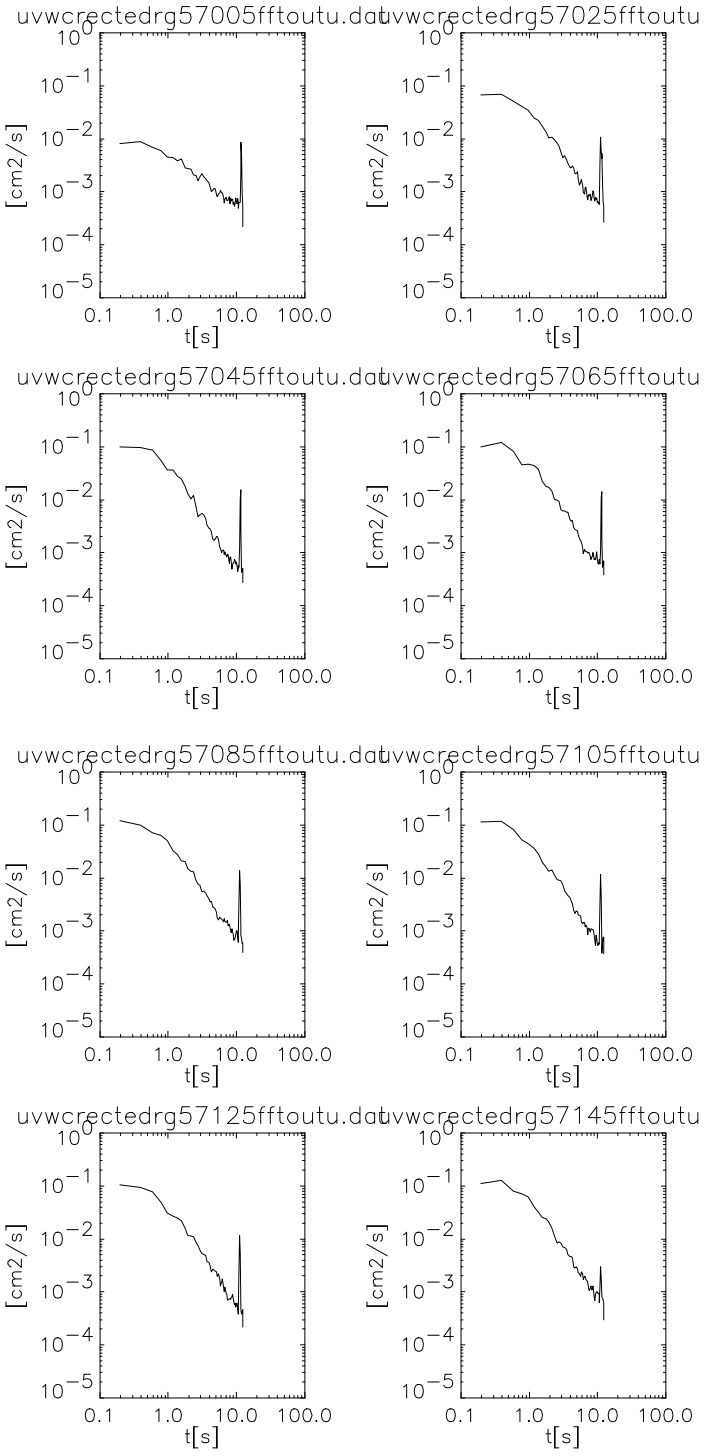
uvwcrectedrg57005fftoutu.dat
uvwcrectedrg57025fftoutu
uvwcrectedrg57045fftoutu.dat
uvwcrectedrg57065fftoutu
uvwcrectedrg57085fftoutu.dat
uvwcrectedrg57105fftoutu
uvwcrectedrg57125fftoutu.dat
uvwcrectedrg57145fftoutu
[cm2/s]
t[s]
0.1
1.0
10.0
100.0

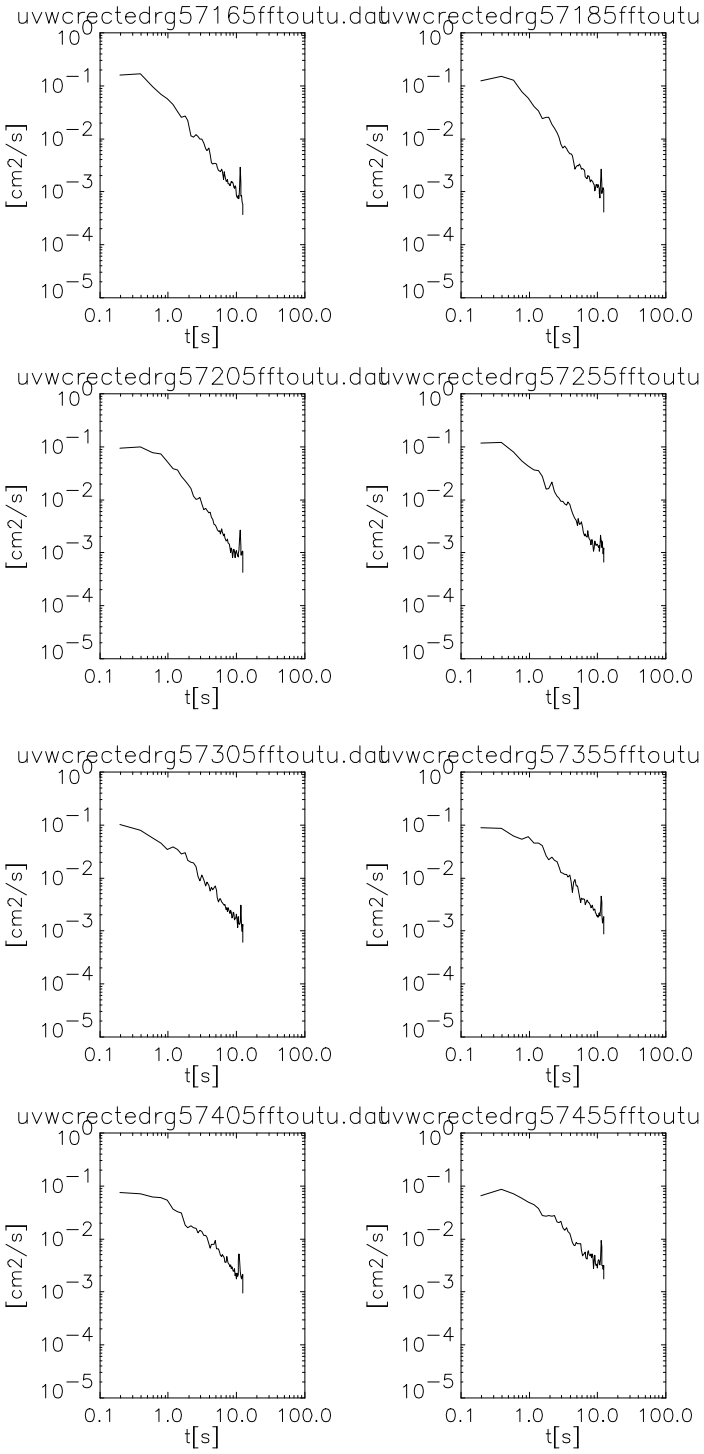

Figure 4-37.- Energy spectra for the u component at 5Hz. Measurements were taken at 0.00, 0.20, 0.40, 0.60, 0.80, 1.00, 1.20, 1.40, 1.60, 1.80, 2.00, 2.50, 3.00, 3.50, 4.00 and 4.50 cm measured from the boundary to the grid

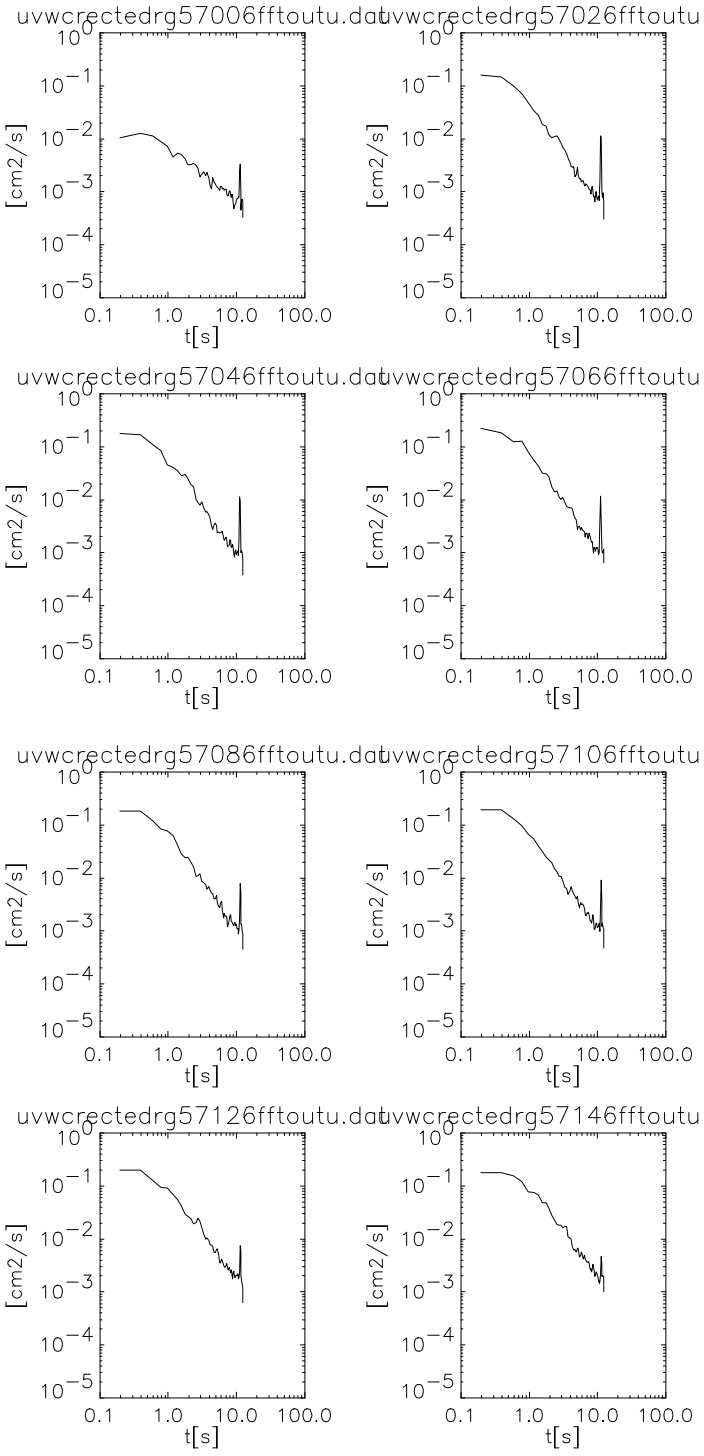
uvwcrectedrg57006fftoutu.dat
uvwcrectedrg57026fftoutu
uvwcrectedrg57046fftoutu.dat
uvwcrectedrg57066fftoutu
uvwcrectedrg57086fftoutu.dat
uvwcrectedrg57106fftoutu
uvwcrectedrg57126fftoutu.dat
uvwcrectedrg57146fftoutu
[cm2/s]
t[s]
0.1
1.0
10.0
100.0

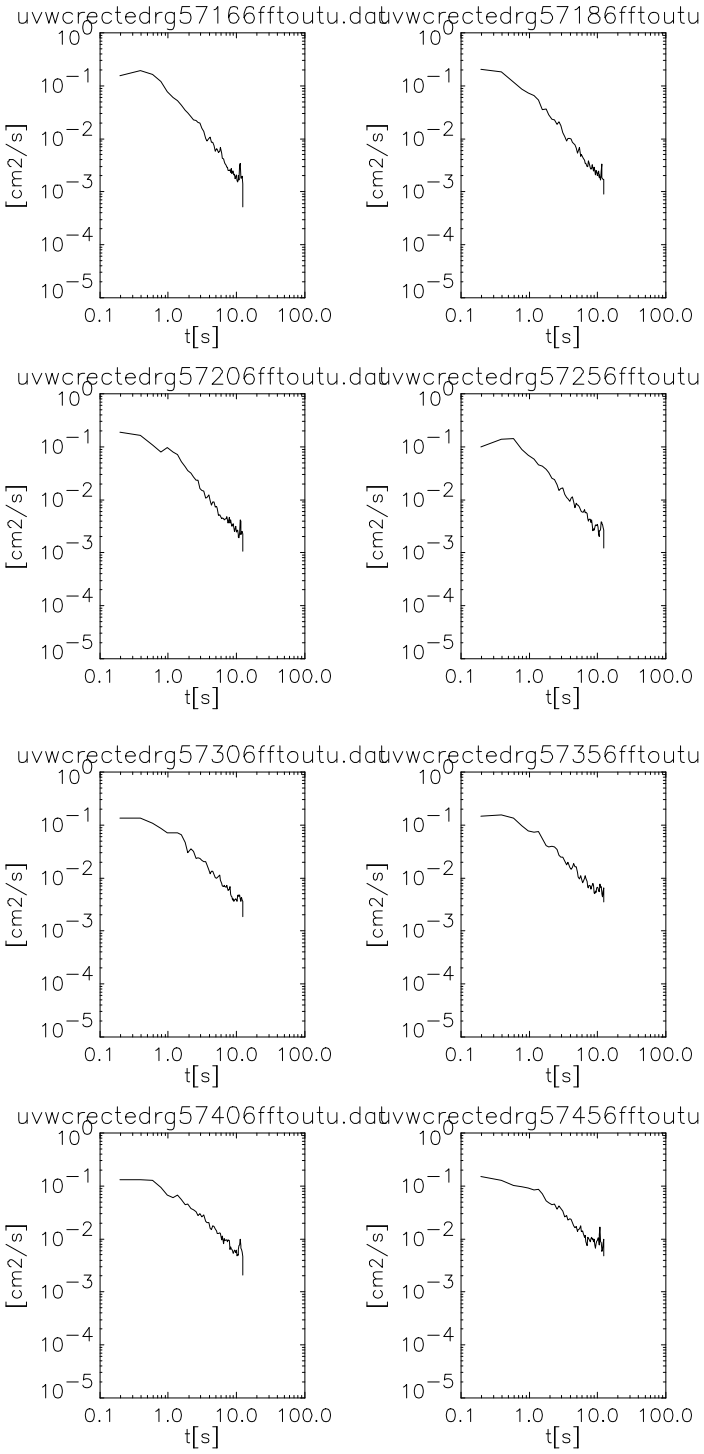

Figure 4-38.- Energy spectra for the u component at 6Hz. Measurements were taken at 0.00, 0.20, 0.40, 0.60, 0.80, 1.00, 1.20, 1.40, 1.60, 1.80, 2.00, 2.50, 3.00, 3.50, 4.00 and 4.50 cm measured from the boundary to the grid

4.2.1.7.5 Autocorrelation results:

Examples of the autocorrelation results corresponding to the u component are presented next. The same general observations made for the autocorrelation results corresponding to the **5MG-FSE-FFTA** could be made to these results, meaning that above the grid (**5MG-FSE-FFTA**) and below it the behaviour of the autocorrelation remains the same. The next four figures are the corresponding autocorrelation for each velocity measurement made (see measurements above). The first autocorrelation in each figure is the closest one to the boundary.

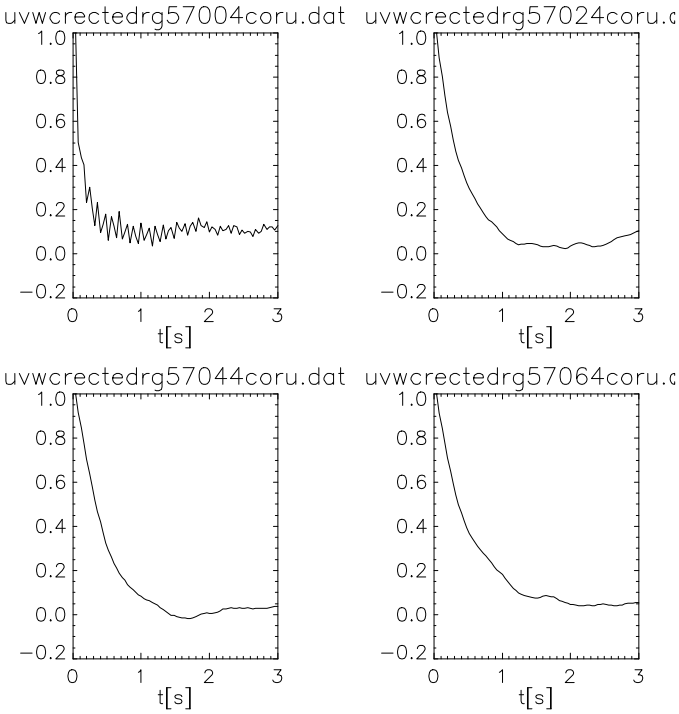

Figure 4-39.- Autocorrelation for the u component at 4Hz. Measurements were taken at 0.00, 0.20, 0.40 and 0.60 cm measured from the boundary to the grid.

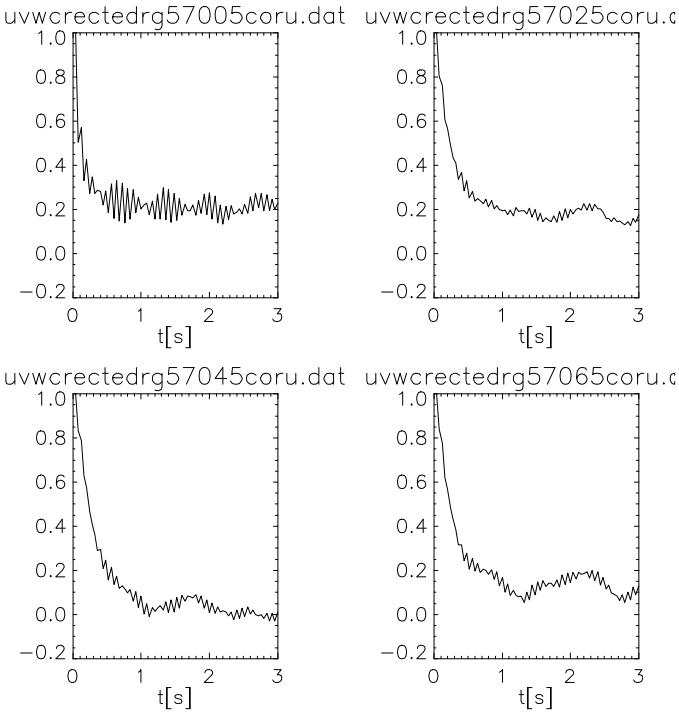

Figure 4-40.- Autocorrelation for the u component at 5Hz. Measurements were taken at 0.00, 0.20, 0.40 and 0.60 cm measured from the boundary to the grid.

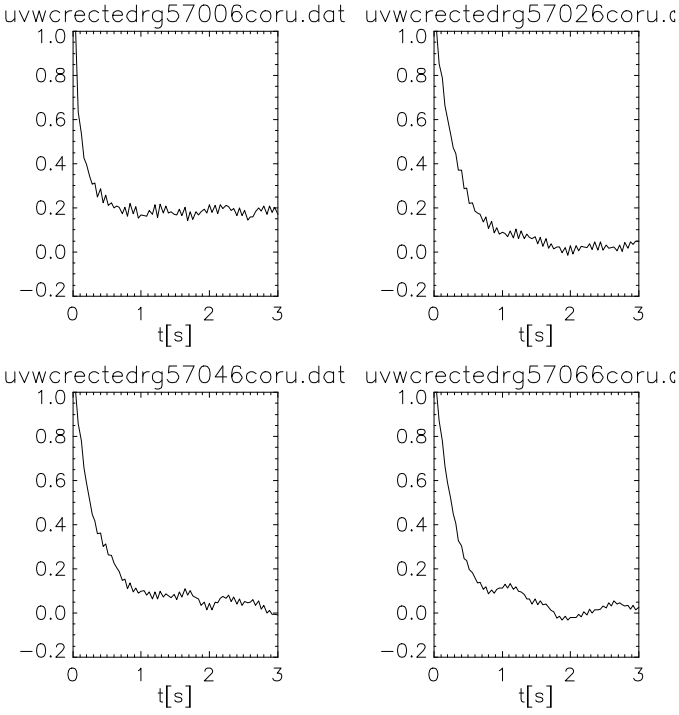

Figure 4-41.- Autocorrelation for the u component at 6Hz. Measurements were taken at 0.00, 0.20, 0.40 and 0.60 cm measured from the boundary to the grid.

4.2.1.8 Comparing SBFE with Hunt and Graham's Experiment.

There are not many experiments dealing with grid induced turbulence interacting with a solid boundary and none with oscillating grid turbulence. Probably Hunt and Graham's experiment (1978) is the most interesting one to compare this work with, since there are radical experimental configuration differences between both. The most important differences between both experiments are, first, that the Hunt and Graham configuration (Figure 4-42) includes a mean flow $\bar{u}_\infty$ and turbulence was produced when the flow passed trough a fixed grid. And, second, that the vortices generated in Hunt and Graham were advected by the mean flow parallel to the boundary also moving at speed $\bar{u}_\infty$, unlike the **SBFE** where no steady mean flow and vortices are advected perpendicularly to a static boundary by the effect of the oscillation of the grid.

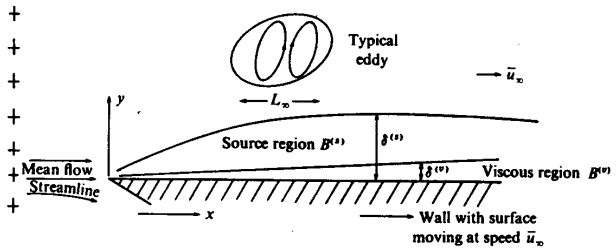

Figure 4-42.- Variance of turbulence components and the turbulent energy in Hunt and Graham (1978).

$$q = \frac{1}{2}(u'^2 + v'^2 + w'^2) \tag{4-8}$$

$$L = 0.1\,Z \text{ (for M = 5)} \tag{4-9}$$

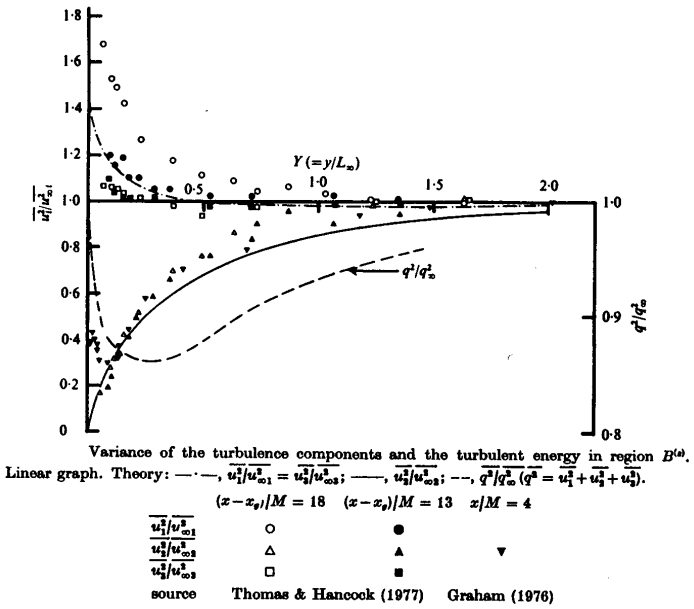

Figure 4-43.- Variance of turbulence components and the turbulent energy in Hunt and Graham (1978).

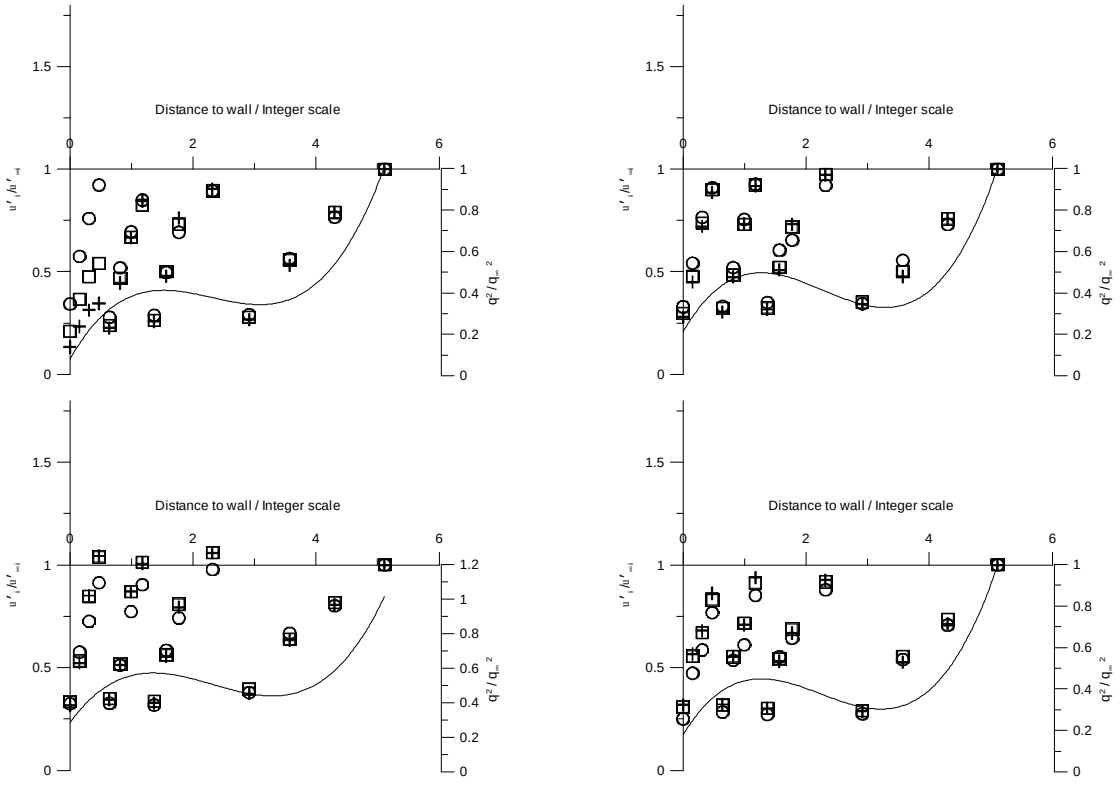

Figure 4-44.- Variance of turbulence components and the turbulent energy in **SBFE**. (+) $\overline{u_1^2}/\overline{u_{\infty 1}^2}$, (O) $\overline{u_2^2}/\overline{u_{\infty 2}^2}$, ( ) $\overline{u_3^2}/\overline{u_{\infty 3}^2}$, (____) $\overline{q^2}/\overline{q_\infty^2}$ $(\overline{q^2} = \overline{u_1^2} + \overline{u_2^2} + \overline{u_3^2})$.

The effect of the squashing of the Reynolds stresses by the solid wall detected by Hunt and Graham is not so evident in the oscillating grid experiments, probably due to the direct impingement of eddies on the wall detected by Redondo (1987).

4.3 Comparison of ADV and Visual Measurements

The purpose of the experiments presented in this section is to study the structure of grid stirred turbulence using different methods. This is done in order not only to verify existing models, but also to be able to compare measurements obtained by these different methods used simultaneously. More than one method of measurement is needed when not only water flow is important, but also, for example, the diffusion of a substance injected into this flow or the influence on some scalar gradient. An example of this is given in Figure 4-45.

Figure 4-45.- Example of a dye introduced into a grid stirred turbulent flow. If the structure of the dye is to be analysed and compared with the structure of the turbulent flow, two methods will be needed.

4.3.1 Experimental configuration

4.3.1.1 Visual experimentation

In this research, turbulence is induced in a large water-holding tank with a grid. The grid has a five centimetres mesh, *M*, and a one centimetre bar width *d*. The stroke *s* is 1.25 centimetres (Figure 4-46). The experimental configuration used was the same as for the 5MG-FSE-FFTA described before in this chapter, and is also detailed in Schaven (2000).

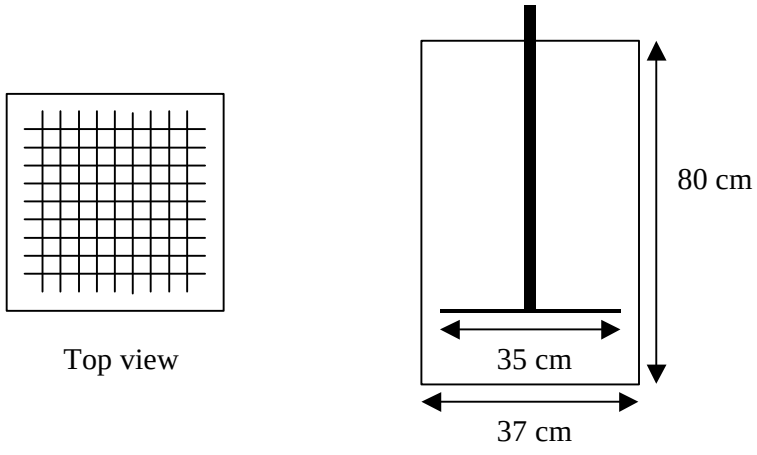

Figure 4-46.- Top view and side view of a schematic representation of the tank used in the experiments. The mesh of the grid is 5 cm, the width of the bars is 1 cm.

In order to minimise reflections, the walls of the tank, apart from the front and a vertical opening on one side, are lined with black adhesive plastic. In order to make the particles clearly visible to the camera a laser sheet is used and, also, to generate a sufficiently powerful laser sheet, a 3.2 Watts laser is employed. The sheet is generated by applying a circular perspex lens to the line of the laser beam. A Sony Video Hi8 is used for grabbing the experiments (Figure 4-47).

The laser sheet was not perfectly perpendicular to the plane of the camera, nor was there any compensation for the Gaussian characteristic of the laser. However, this was not a problem. In order to track all particles properly the DigImage program, needs only to identify a particle as such. No further use is made of the specific intensity level captured by the camera. As long as the intensity is high enough, or in other words, as

long as the laser is powerful enough, the program can distinguish between particles and background.

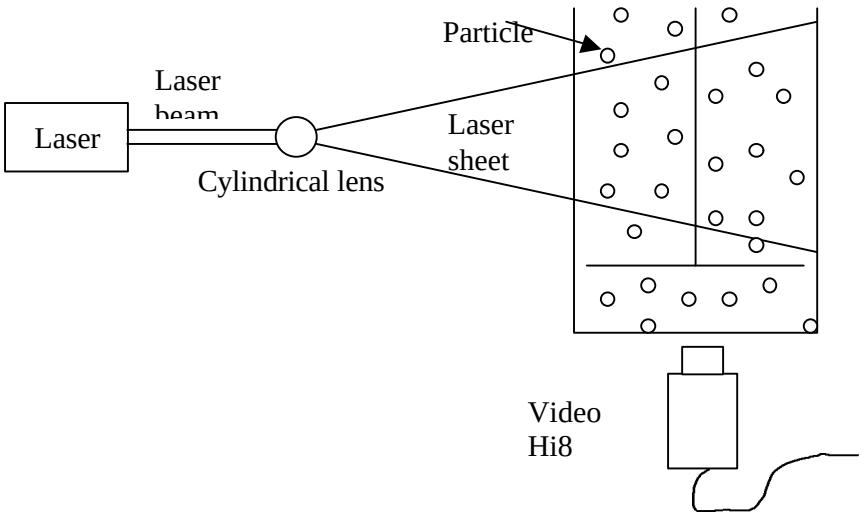

Figure 4-47.- Schematic representation of the configuration used for the visual experiments.

The first method for measuring the structure of the grid-induced turbulence is by visual representation using Particle Imaging Velocimetry (PIV). Tracer-particles (Pliolite) are added to the tank of water with a density similar to, but slightly larger than, that of water. By changing the salinity one can manipulate the water density until it reaches the same density as that of the particles. The theory is that all particles match exactly the flow of the water. By illuminating the particles with a laser, it becomes possible to capture the particles on film with a minimum of background illumination. This results in a 2-dimensional video of the flow.

The imaging program used to interpret the video images was DigImage. This program has a number of helpful possibilities. The program can track individual particles through time, thus enabling a Langrangian calculation of the velocity field. A related program, trk2Dvel, gives the averaged velocity statistics of the particles in a user-defined area for each point in time, with the option of averaging in time as well. It can also generate a grid, and calculate a spatial picture averaged in time. Apart from the

velocity statistics, parameters such as vorticity, dissipation and stream functions can be represented in this manner.

One can see that there are now two possibilities to obtain information regarding velocity characteristics and spatial distribution. Velocity characteristics can be obtained by the two methods described above. Spatial characteristics, i.e. the length scale of the vortices, can be obtained through the examination of the grid-generated velocity and/or vorticity field, and by direct observation of the video images.

4.3.1.1.1 Acoustic experimentation

The second method to measure turbulent flow is using an Acoustic Doppler Velocimeter, or ADV. The ADV emits sound waves, which are reflected by very small particles. These particles should be small enough not to need special treatment in the way the PIV-particles did, because they will then exactly match the flow of the water. Using the Doppler effect, one can obtain the velocity characteristics at a certain point in two or in three dimensions, depending on the ADV used. By using two ADV´s one can obtain the velocity characteristics in two points, and thus obtain a measure for the spatial correlation between these two points, as well as the temporal correlation and Fourier-spectrum in either one.

The experimental configuration for the ADV experiments is somewhat different. There are two ADV´s available, one that measures velocities in only two dimensions, and one that measures velocities in three dimensions (Figure 4-48). The ADV measures in an area five centimetres from its sensor. Furthermore, the one that measures in three dimensions does so five centimetres lower, but the one that measures in two dimensions does so five centimetres to one side. The general experimental configuration used was the same as for the 5MG-FSE-FFTA described before in this chapter.

It is now possible to define two measuring positions at the same distance from the grid, but at a variable distance between each other. This helps analyse spatial correlations between the two points, as well as temporal correlations in each point individually. However, this can only be done in the plane parallel to the grid. The velocity statistics perpendicular to the grid can only be measured by one of the ADVs.

In order to get as complete a picture as possible, measurements can be made at different distances to the grid, different distances between the two ADV´s and at different frequencies of the grid.

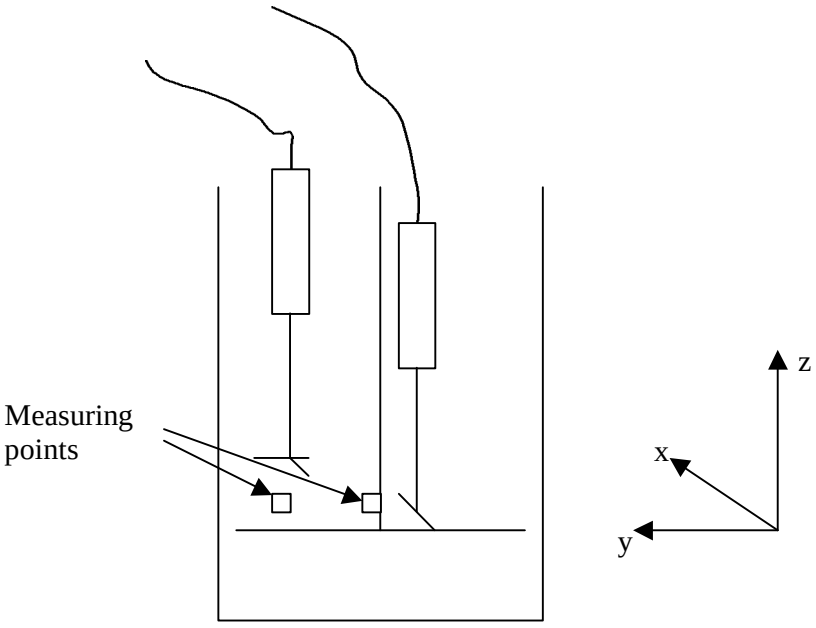

Figure 4-48.- Schematic representation of the configuration used for the ADV-experiments. The co-ordinate system is also given. The x-axis is perpendicular to the paper.

4.3.2 Visual and ADV experiments

Data Mesh Generation:

The first method used to determine the relevant parameters was to generate a data mesh or grid, so the data obtained from the images are extrapolated to a regular user defined mesh. This yields a picture where for instance velocity and vorticity are represented. However, this technique averages over time. It is obvious that the higher the velocity and the smaller the length-scale, the smaller the time-scale will be. It is therefore not possible to average the area far from the grid for the same amount of time as the area near the grid. The picture has therefore been divided into several areas,

which have been processed individually. An example of the result can be seen in Figure 4-49.

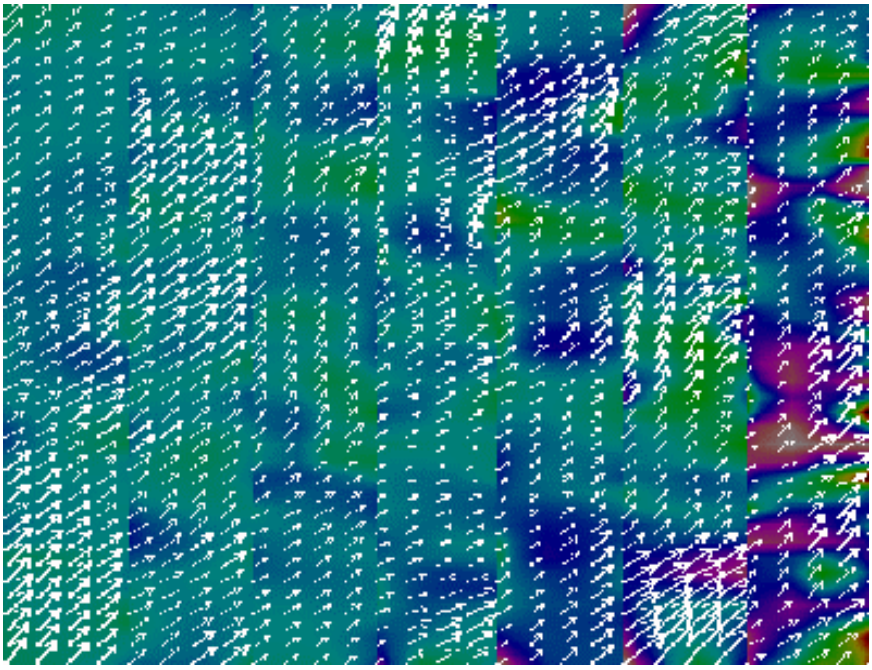

Figure 4-49.- Picture of a two-dimensional velocity and vorticity field. The scaled arrows represent the root- mean-square velocity, the colours represent vorticity intensity. The oscillating grid is to the right of the picture.

It is quite difficult to conclude from this picture exactly where the vortices are, and what their size is. The method used here was simply to count vertically the distinct shapes in each individual area, and divide them by the vertical size of the picture. The method implies the elaboration of a large amount of these pictures and average the results. Due to limited time and disk-space, and because the objectives are to examine the possibilities of the use of these methods in sediment research, however, only one picture was analysed. It does give a clear indication of the range in which the result should be.

The velocity for each area was determined in a similar way. In each area, a different velocity scale is used, due to the large differences between velocities far from and near to the grid. For each area there is a known reference length for the velocity arrows. Several different arrows are taken, typically of the order ten, and averaged.

Velocity Statistics and Direct Calculation:

The second method used for the determination of the size of the vortices was by direct observation of the recording. The film can be played at very low speeds, and particles can be tracked very accurately. However, a particle rarely, if ever, follows the entire contour of a vortex. Neither does a vortex stay fixed in space. Furthermore, in order to be able to do this at all low grid frequencies must be used. If the frequency is very high, it becomes almost impossible to analyse the picture close to the grid not using a high speed camera. However, if the frequency is very low, the turbulence becomes very susceptible to secondary flows.

An idea of what the flow looks like tracked over a short period of time, typically a few tenths of a second, is given in Figure 4-50. The trk2Dvel program calculates the velocity statistics. Here again the screen has been divided into several segments, and the velocity is averaged over this area as a function of time. Among others, the root-mean-square velocities are calculated.

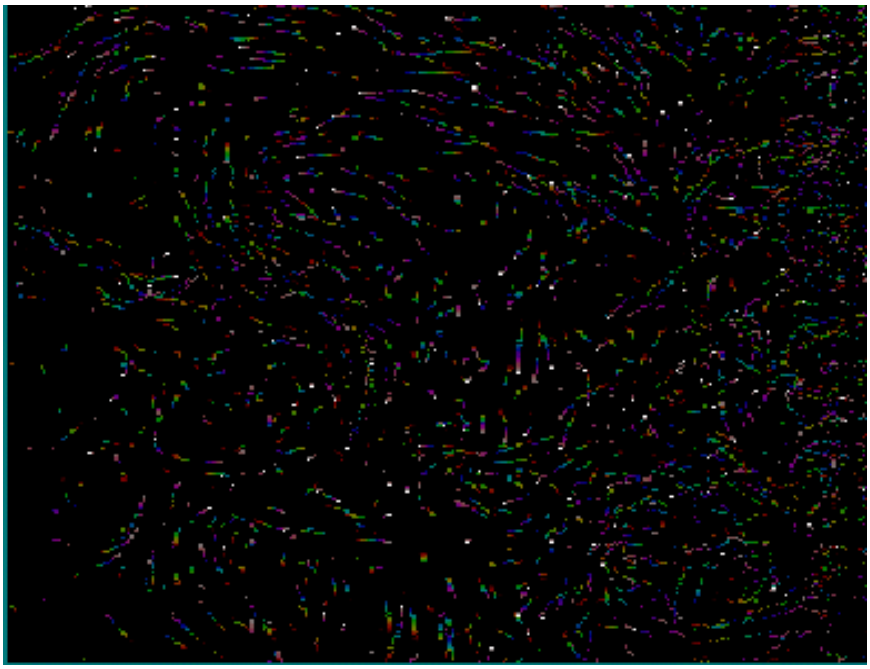

Figure 4-50.- Tracking of particles over a period of 0.5 seconds. The differences in scale of the vortices can clearly be seen.

The results given are two long series of velocity fluctuation data in two and three dimensions. In order to be able to use statistics on these data, long series are generated, of 22500 points, at a acquisition frequency of 25 Hz. This gives the integral time scale of the flow. Together with the velocity statistics one can calculate an integral length scale integrating the autocorrelations in time. This can then be compared with the spatial correlation between the two measuring points.

Similarly to the visual experiments, with these parameters it is ideally possible to describe the entire flow.

4.3.3 Results

Here the dependencies on the stroke, s, and mesh, M, are not included, as these quantities where not varied, and as seen before in this chapter, constant c depends only on the grid and general configuration geometry. They are therefore incorporated into the new constant a . Now equation **(4-1)** becomes:

$$u' = a\ w\ z^{-1} \tag{4-10}$$

In order to compare the results of the different measurement methods, we must first make some other calculations. The first is to determine the integral time-scale of the fluctuations given by the ADV. This is determined from the autocorrelation of the data. A typical result of the autocorrelations at a certain frequency is given in Figure 4-51.

From Figure 4-51 some important conclusions can be made. The correlations far from the grid are difficult to distinguish. This is probably due to the secondary flow in the tank, which grows more important as the frequency of the grid decreases and the distance to the grid increases. It is therefore important, when performing experiments far from the grid, to do so at high enough frequencies.

The u' velocities can be easily calculated from the fluctuation data, after subtraction of a mean. This mean can be calculated in two ways, a simple mean over all

points, or as a moving average. The advantage of a moving average is that it takes into account any larger scale movements and leaves only the real fluctuations. In Figure 4-52 and Figure 4-53 the two different methods are represented.

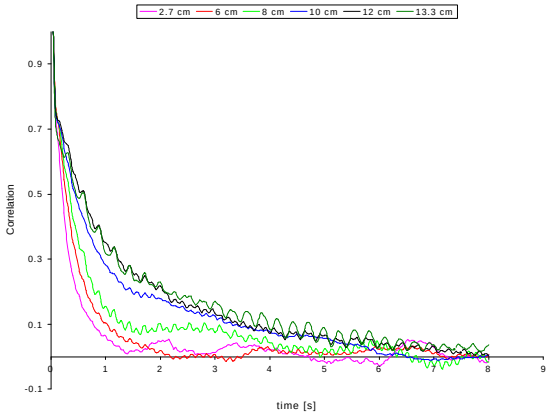

Figure 4-51.- Autocorrelations at different distances to the grid (distances at top of graph). The grid frequency is 3.7 Hz. From this the integral time-scales can be determined.

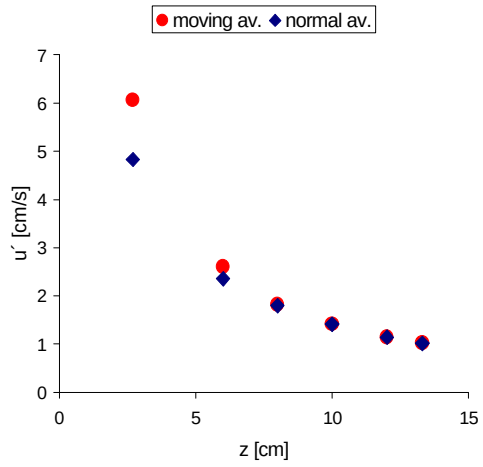

Figure 4-52.- The u' velocity as a function of the distance to the grid, with and without a moving average. The grid frequency is 6.2 Hz.

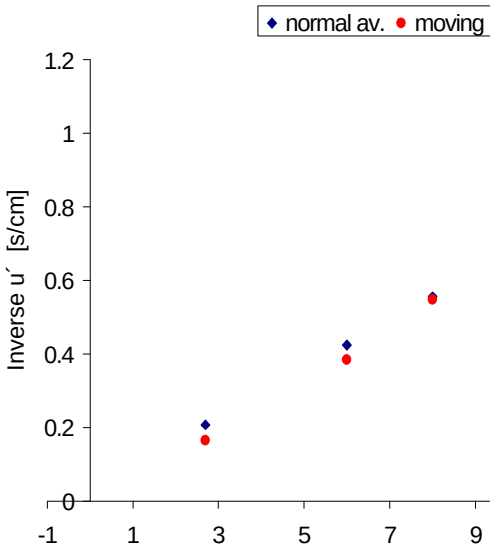

Figure 4-53.- The inverse of the u' velocity as a function of the distance to the grid, with and without a moving average. The grid frequency is 6.2 Hz.

It can be clearly seen that at a high frequency of 6.2 Hz there is only a significant difference at small distances to the grid. This is logical, as with high grid frequencies the turbulence close to the grid will be strongly influenced by its movement.

Far from the grid however, the velocity fluctuations are still strong enough not to be influenced by secondary flows, and do therefore not need a moving average. One can also expect, as verified by experiments, that at low frequencies the results are reversed. A moving average now gives the greater difference at large distances to the grid. In Figure 4-53 it can also be seen that the points calculated with the moving average follow a straighter line than when normal averaging is used and give a better result, consistent with theory. The use of a moving average, which somewhat complicates the data handling, therefore depends on the distance and grid-frequency of interest. Moving average and mean could be used to establish the full developed turbulence zone. Where both values come together a well develop turbulence flow is present.

Two ADV´s were being used in order to calculate the spatial correlation directly. Typical results can be seen in Figure 4-54. The data from the 3-dimensional probe was used for the autocorrelations, r.m.s. velocities and subsequent calculations.

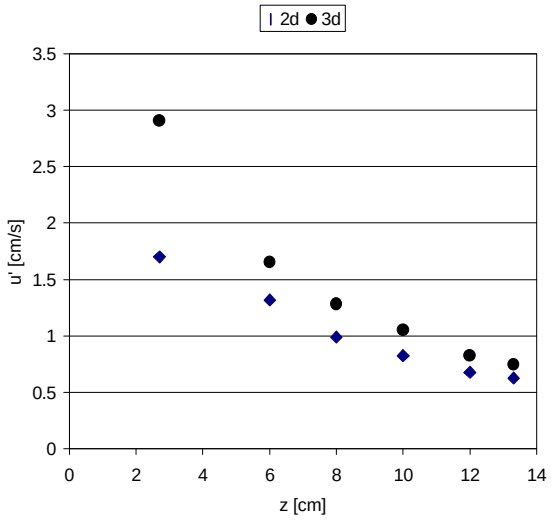

Figure 4-54.- u' velocity as a function of the distance to the grid. Each height is calculated simultaneously using a 2-dimensional and a 3-dimensional ADV.

First, the integral length-scale was calculated for the different frequencies of the grid. Although the length-scales differ somewhat, only the results calculated at 2.3 Hz do not exhibit any dependence with distance from the grid indicating that the flow is not fully turbulent (Figure 4-55). A linear relation is expected from theory and this is clearly not the case. The reason for this anomalous behaviour is also due to the fact that

the autocorrelations at this frequency were very sensitive to secondary flows. The other three relations are averaged, and the result can be well compared with the scales found with the visual method using DigImage.

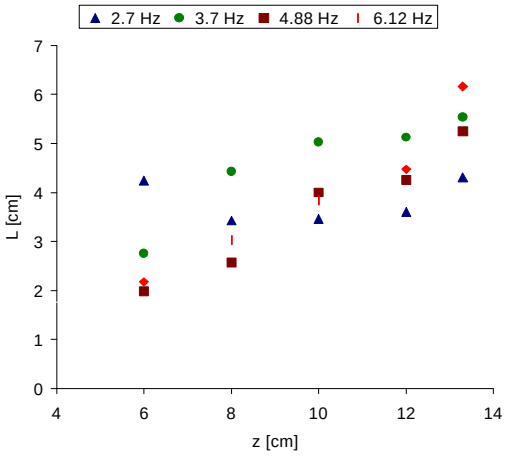

Figure 4-55.- Integral length-scale L as function of the distance to the grid. Measurements were made at four different oscillating frequencies.

The results in Figure 4-56 are also in fairly good agreement. The ADV results and the visual results have the same linear relation, but have an offset with each other. Only the result with the ADV at a small distance is very different. The point does not follow the linear relation, very probably because of the influence of the grid. This means that experiments closer than about 6 cm will be very difficult to perform.

As mentioned by Thompson and Turner (1975) the integral length scale for a grid of $M = 5$ could be estimated as:

$$L = b\, z \tag{4-11}$$

Fits can be made to the data in Figure 4-56, which will give the parameter b, given in equation (4-11). A value found in literature, for a grid similar to the one used here, was b = 0.10. However, for the ADV, grid-generation, and direct calculation, the values are respectively b = 0.43, b = 0.36, b = 0.32. The difference in the values found

is not very big. This is remarkable however, considering the velocity differences between the different methods (Figure 4-57).

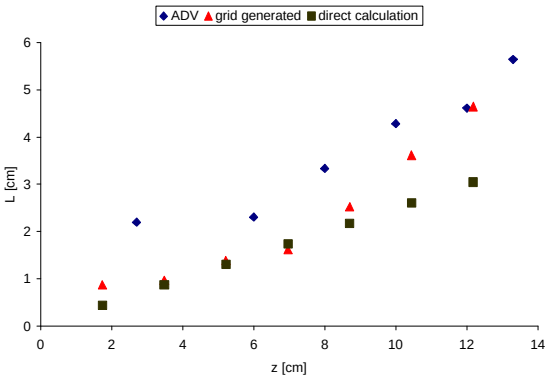

Figure 4-56.- Integral length-scale L calculated with the 3D-ADV, grid-generation and direct calculation.

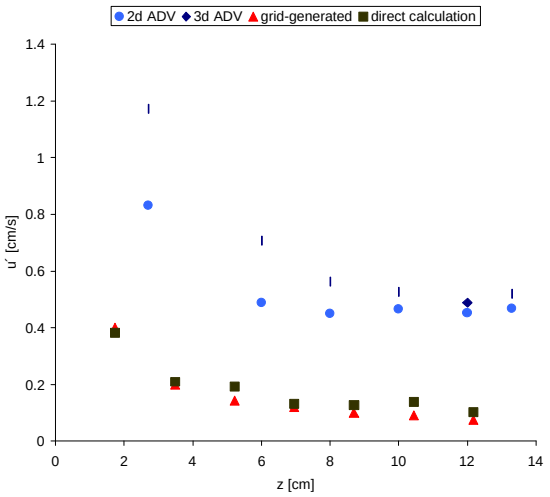

Figure 4-57.- u' velocities as a function of the distance to the grid, with a grid-frequency of 2 Hz. The flattening at large distances is due to secondary flows.

The two methods used in DigImage are very similar to each other. However, there is a great difference between either of the ADV´s and DigImage methods. It is therefore somewhat surprising that the integral length-scales shown earlier are so similar.

The probable reason is that in trk2Dvel the program calculated the velocities, whereas the length-scales were determined by hand. This makes it much more sensitive

to mistakes. As shown earlier, these length-scales do closely resemble the ones calculated with the ADV.

Another point of interest, in order to get a complete picture of the turbulence structure, is the relation between velocity and grid frequency, where a linear relation is expected. Results are given in Figure 4-58.

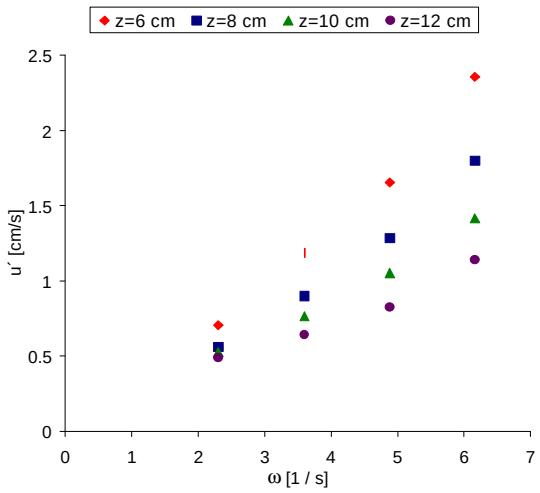

Figure 4-58.- u' velocities as a function of the grid-frequency, measured at different distances. A linear relation is clearly seen.

The linear relation between the r.m.s. velocity and the frequency, as predicted in equation (4-10), is verified in Figure 4-58. A L.S. fit is now made to the inverse of the r.m.s. velocity as a function of the distance to the grid. From these the value of $1/(a\ w)$ can be determined, and after dividing by the frequency, a itself. The results are given in Table 4-1. The same was done for the results found at 2.3 Hz with Trk2Dvel, the direct calculations as well as the grid-generated results (Table 4-2).

With the 2-dimensional probe a velocity offset was found, consistent with the velocity differences shown in Figure 4-54. This offset seemed to depend on the grid frequency, as it increases almost linearly with the frequency. However, with only three points it is difficult to tell.

Table 4-1.- The derivatives of Figure 4-59, and the values for the constant a , for the 2-dimensional (2D) and 3-dimensional (3D) ADV, at different frequencies.

Frequency (Hz)	$1/(a\,w)$ (2D) (s/cm^2)	a (2D) (cm^2)	$1/(a\,w)$ (3D) (s/cm^2)	a (3D) (cm^2)
3.6	0.1226	2.26	0.1313	2.12
4.88	0.0995	2.06	0.0996	2.06
6.16	0.0801	2.03	0.0731	2.22

Table 4-2.- Results found with the program trk2Dvel, at a frequency of 2.3 Hz.

Frequency (Hz)	$1/(a\,w)$ (s/m^2)	a (m^2)	$1/(a\,w)$ (s/m^2)	a (m^2)
2.3	0.9618	0.45	0.8632	0.50

The reason why no results are given for the ADV at 2.3 Hz, is that at small distances to the grid there already was a strong secondary flow (Figure 4-55). Because of that no linear relation between the inverse of the r.m.s. velocity and the distance to the grid existed, as described before in this section.

In Figure 4-57 the large differences between velocities found with the ADV´s and with trk2Dvel were demonstrated. This is also seen in the large differences between the values found for the constant a.

The equations found to describe the turbulence-structure are:

3D-ADV:

$$L = 0.43\,z \tag{4-12}$$

$$u' = 2.13\,w\,z^{-1} \tag{4-13}$$

Grid generation:

$$L = 0.36\,z \tag{4-14}$$

$$u' = 0.45\,w\,z^{-1} \tag{4-15}$$

Direct calculation:

$$L = 0.32\, z \tag{4-16}$$

$$u' = 0.50\, w\, z^{-1} \tag{4-17}$$

Finally, we can look at the energy spectrum of the velocity fluctuations. The slope here is –1.9, somewhat stronger than the –5/3 predicted by the spectral equivalent of the density of turbulent energy per unit mass ($E(k) = C < e >^{2/3} k^{-5/3}$). This is probably due to the influence of non-local and non-homogeneous dynamics and the lack of the application of Taylor's hypothesis to relate wavenumber k and frequency ($U \mu$ f k^{-1}) in a zero-mean flow. The difference is not very large however. It can also be seen that the slope is not influenced much by the frequency of the grid, or in other words, by the energy input into the system. The value found here for the constant C is 0.4.

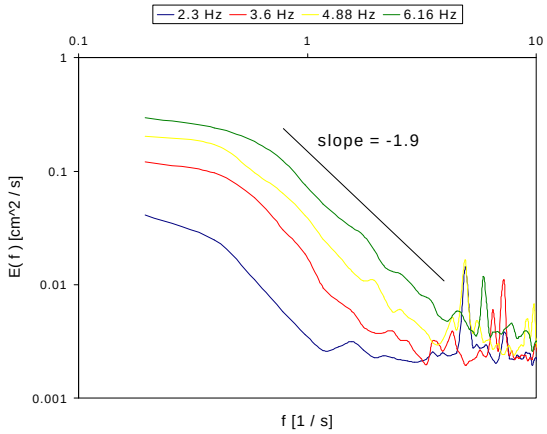

Figure 4-59.- Energy spectrum of velocity fluctuations in time, for four different frequencies of the grid.

4.4 Jet – Turbulence Flow Transitional Region

4.4.1 Jets, Vortex Interaction and Fully Developed Turbulence.

As mention before in this work, near the grid there is a generation of a quasi-steady jet flow close to each grid bar (Thomson and Turner, 1975). After a certain distance, jets interact, and break to give turbulence which is advected by the jets. It is

also expected that after turbulence is generated, no mean flow, or at least no steady mean flow is present.

Figure 4-60 shows the transitional region between quasi-steady jet flows and fully developed turbulence in the **0.8MG** experiments. In the upper part of the image quasi-steady jet flows could be seen (the oscillating is above the image), and the interaction between flows is noticed further down. It is there where the formation of vortices is. Then these vortices keep interacting between each other and are advected by the jets generated near the grid. This is the fully developed turbulent region.

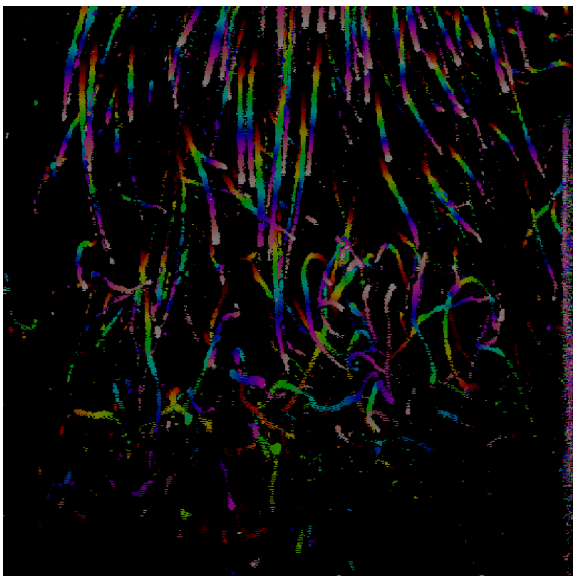

Figure 4-60.- Transitional region. In the upper part of the image quasi-steady flows could be seen. The interaction between flows is noticed further down. Particle streaks are shown.

4.4.2 Mean velocity and running average.

Some analysis were carried out using a running average and plain average for calculating the r.m.s. turbulent velocity, u', and no difference was found after turbulence was fully developed. If u' using plain average and u' using running average are plotted together, there is a clear difference near the grid. As we go farther from the grid, both u' merge to about the same value meaning that fully developed turbulence has been achieved and no effect of mean or secondary flow is noticed (see Figure 4-52 and Figure 4-53).

Chapter 5

SEDIMENT TRANSPORT EXPERIMENTS

The present chapter focuses on the experimental technique and on the interpretations of the data that may be obtained from grid generated zero-mean-flow turbulence. In section 5.1 the experimental configuration and its characteristics are presented. In section 5.1.3 some of the results obtained are shown, and in section 5.2 a method for measuring the mass flux during the lift-off experiments is presented following Sánchez and Redondo (1998). And in section 5.3 a practical case is presented.

5.1 Motion Initiation and Lift-off Experiments

The experiments and the different configurations used are described, as well as the basic experiment design on which all the experiments performed are based.

Grid - stirred turbulence has been used since Rouse and Dodu (1955) and Turner (1968) to investigate stratified flows mainly to estimate entrainment rates across density interfaces. Xuequan and Hopfinger (1987) and Tsai and Lick (1986) used it to investigate sediments.

These experiments consist of a box (Figure 5-1) full of water in which a regular square grid is stirred vertically generating a well-known turbulent field. The motion of the grid is controlled by a DC motor, and the frequency of oscillation of the grid is controlled by changing the input voltage to the motor. For further details see section "0.8 cm Mesh Grid (0.8MG) Experiments" in previous chapter.

The turbulence generated depends on various parameters: The distance to the centre of oscillation, Z, the stroke, s, the frequency of oscillation, ω, and the mesh of

the grid, M . The r.m.s. velocity of turbulence, u', can be expressed for our mixing box following Turner (1968) and Sánchez and Redondo (1998) as:

$$u' = c\, s^{3/2} M^{1/2} w\, z^{-1} \tag{5-1}$$

where $c = 0.6$ for this configuration as seen in the previous chapter.

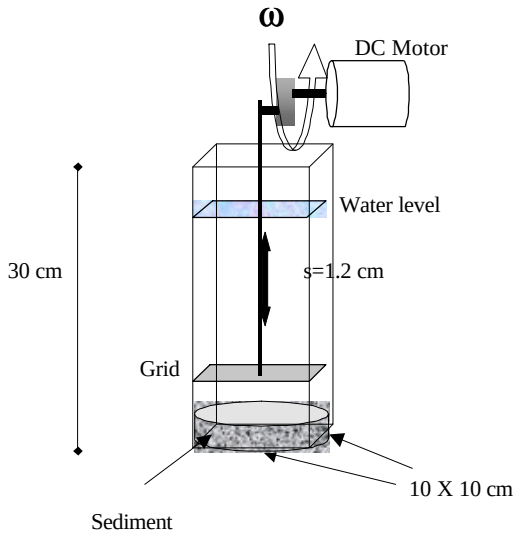

Figure 5-1.- Experimental configuration for stratified flows and sediment experiments. ω is the frequency, s is the stroke.

The r.m.s. velocity fluctuations u' damps very quickly with distance from the grid in a power law fashion. In Figure 5-2 the measure velocity decay for different grid frequencies is shown according to equation (5-1), and it is also clear from Figure 5-3 that the response of the turbulent r.m.s. velocity to changes in frequency is greater closer to the grid. Thanks to this characteristic, it is possible to control the velocity at the top of the sediment sample in two ways, by changing the frequency of the grid, and controlling the distance between the centre of oscillation of the grid and the sample surface. The u' at the top of the sample is considered equal to the friction turbulent velocity u_* ($u' \cong u_*$).

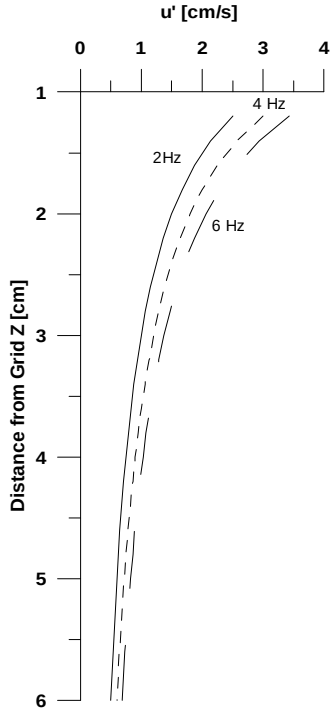

Figure 5-2.- Evolution of u' with distance from the grid for different oscillating frequencies of the grid (2, 4 and 6 Hz).

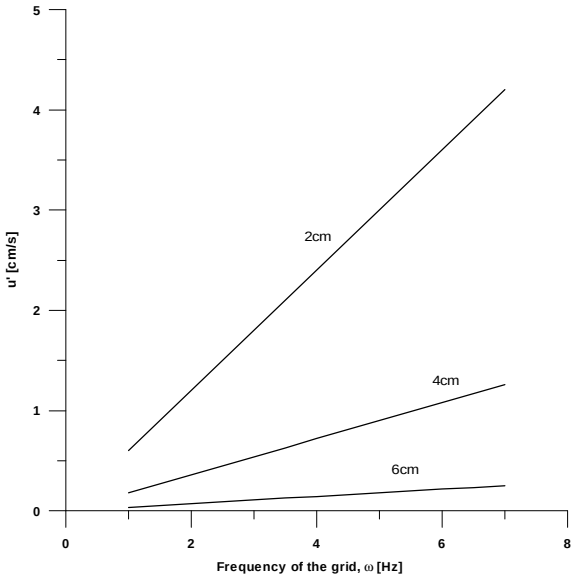

Figure 5-3.- Sensitivity of u' to changes of ω. Estimations at 3 different distances of the grid (2, 4 and 6 cm).

The frequency is directly measured from the digitized images (see previous chapter) and the suspended sediment concentration is measured using a calibration relation obtained for known concentrations of particles and their corresponding light intensity value. The concentration change in time is proportional to the change in light intensity. The vertical mass flux could be determined from a simultaneous calibration of the spatial and temporal gradients of the sediment concentration (Sánchez and Redondo 1998)(See further on in this chapter).

Subsamples from the cores extracted were used to calibrate the suspended sediment concentration with the light intensity transmitted from the back of the box to the camcorder. These core subsamples were taken from the surface of the cores. The subsamples were dried and desegregated. Small amounts of sediment weighing between 0.018 g and 0.10 g were kept separately in different packages. Once this was done, the mixing box used to perform the experiments was filled with a given volume of water and the light characteristics were configuration in order to record the calibration process under the same conditions as the experiments.

The initial conditions were considered as 100 % of light transmitted, then the pre-weighed sediment was added. The water in the tank was strongly agitated to get it well mixed and sediment concentration was computed each time sediment was added. A fit was made to these results so the sediment concentration could be estimated for every light intensity value present during the experiments.

The relationship between light transmittance (or light intensity) and the suspended load concentration was obtained using Digimage software. This software has 255 (0 to 254) different values for light intensity. Thus, a known amount of suspended sediment load could be assigned to a specific intensity value (e.g. for 100 % transmittance, the value 0 was assigned, and for 0 % the assigned value was 254). The fact that a value of 254 is reached does not mean that a maximum suspended sediment concentration is achieved. The sediment concentration could increase but since the light transmittance is already 0%, if more sediment is suspended no change in transmittance will be noticed. This is a limiting factor at the time the experiments are being conducted.

5.1.1 Motion Initiation Experiments

A thin layer of nonconsolidated sediment is placed at the bottom of the tank paying particular attention to letting the surface rest as flat as possible avoiding compacting the sample. The sediment size used ranged from 0.0149 cm to 0.071 cm (fine to coarse sands according to the Wentworth (1922) scale. Folk, 1968), within this range 7 grain sizes were analysed (0.0149, 0.021, 0.03, 0.035, 0.05, 0.059 and 0.071 cm). Each sample was made of a single sediment size by sieving, using a series of progressively finer square-mesh sieves, and separating particles principally on the basis of their intermediate axial diameter.

The distance between the centre of oscillation of the grid and the sediment surface (Z) was the same for all the experiments. Each of them began at a frequency of 3.5 Hz and then increased gradually until a generalized movement of the particles could be seen on all the sample surface, this was done several times and the same procedure was followed for each sample.

The critical velocity, u'_{cr} ,that produces this movement at the surface of the sample was computed using equation (5-1) for each sediment size used.

The friction velocity, u_* is defined as

$$u_* \equiv \sqrt{\frac{t_0}{r}} \tag{5-2}$$

where t_0 is the turbulent wall shear stress and is defined in terms of a turbulent viscosity as

$$t_0 = r\ \overline{u'_1 u'_3} = K \frac{\partial u}{\partial z} \tag{5-3}$$

When u_* is strong enough to initiate the motion of the sediment on the top of the bed then it is called Critical Bed Shear Velocity, u_{*cr}, determined by Shields (Rijn, L.C., van 1984) for the initiation of sediment motion in shear flow. The critical r.m.s. turbulent velocities, u'_{cr}, were also compared with the theoretical Critical Bed Shear Velocity, u_{*cr}, for each sediment size. An analytical method given by Rijn, L.C. was used to determine this value. The steps followed were:

1.- Compute the particle parameter, D_* using

$$D_* = D_{50}\left[\frac{(s-1)\,g}{u^2}\right]^{1/3} \tag{5-4}$$

where D_{50} = average particle size, s = specific density $\left(\frac{r_s}{r}\right)$, g = acceleration of gravity, u = kinematic viscosity coefficient.

2.- A specific range of D_{50} is chosen from Figure 5-4 according to the result obtained from step 1, and the corresponding critical mobility parameter, q_{cr}, is computed.

3.- Compute the critical bed-shear velocity, u_{*cr}, using

$$u_{*cr} = \sqrt{q_{cr}\,(s-1)\,gD_{50}} \tag{5-5}$$

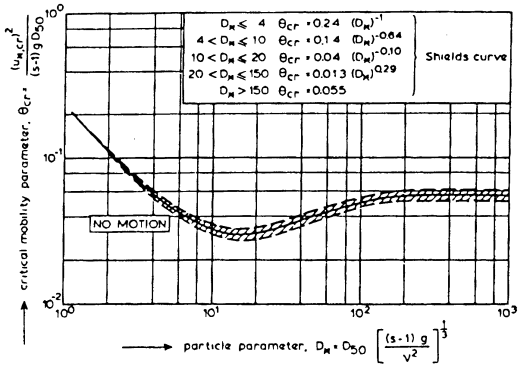

Figure 5-4.- Initiation of Motion According to Shields. (Taken from Rijn, L.C., van, (1984))

5.1.2 Sediment Lift-off Experiments

A different set of experiments was performed using samples taken from different locations in the bottom of the sea at the Gulf of Lion and at the Ebro Delta (Figure 5-5). In the case of the samples from the Gulf of Lion (D_{50} = 0.00066cm, fine silt) one centimetre thick disks were cut from the cores and placed at the bottom of the tank, and for the Ebro Delta (D_{50} = 0.026cm, fine sand) a uniform plane bed of sediments was placed at the bottom of the tank. The frequency was gradually increased as in the previous section but leaving a frequency higher than the critical *motion initiation frequency*, until severe sediment entrainment occurred. The sediment resuspension and later deposition were recorded. After deposition, some samples were resuspended again immediately, others were let to rest for different time periods (between 1 and 30 days) and then resuspended again.

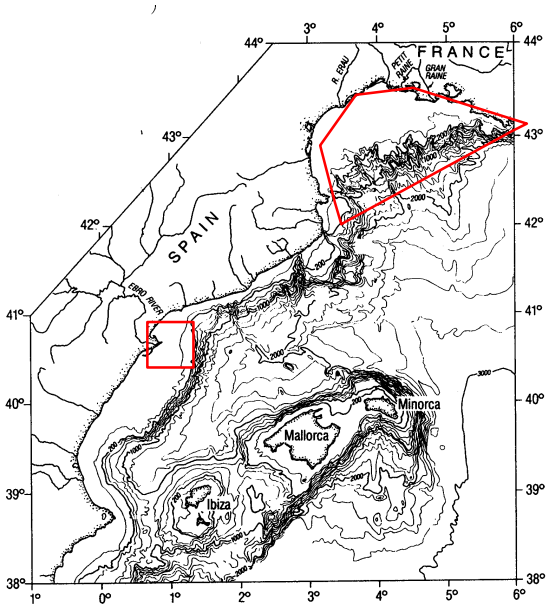

Figure 5-5.- Map showing the Ebro Delta (square) and the Gulf of Lion (irregular shape) areas where field sediment samples were taken to be used in the experiments.

5.1.3 Results

5.1.3.1 Motion Initiation Experiments

The results of the experiments, as well as the Shields critical bed-shear velocity value (u_{*cr}) calculated for each sediment size used, are displayed in Figure 5-6. The zero-mean-flow turbulent velocity, u', obtained from the experiments are always lower than the comparable velocities estimated for the Shields parameter. The difference is greater for smaller sediment sizes. This could probably be so because the surface rugosity is proportional to the grain size. The decrease in surface rugosity needs an increase of the shear velocity at the bottom in order to generate enough turbulent shear to start the motion of the sediment grains. While for zero mean turbulence generated by the grid, u' does not depend in a non-linear way on the surface rugosity, probably this characteristic is responsible for the relation between u' and sediment size, $u' \propto D_{50}$.

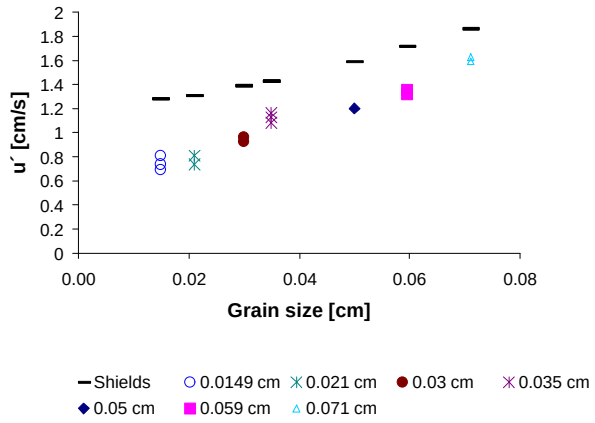

Figure 5-6.- The u' measured needed to start sediment motion is plotted as well as the corresponding u_{*cr} (Shields Parameter) for each sediment size used.

5.1.3.2 Sediment Lift-off Experiments

In this section, the results of the sediment lift-off experiments are explained. Grid oscillation was started at a low frequency and was increased gradually. As soon as there was enough turbulent energy to lift-off the sediment, a sharp lutocline was formed, advancing until equilibrium was reached. The evolution of the lutocline during lift-off and deposition was analyzed. As an example, time series of sedimentation (a) and sediment lift-off (b) are shown on Figure 5-7 a) and b). Time series are composed of 500 columns of light intensity measured along one pixel thick band at a fixed position, and are taken at assigned time intervals. The vertical position of lutocline is represented in the Y-axis, and time is plotted on the X-axis. The different gray intensities represent light intensity attenuation due to change in sediment concentrations. This helps to measure the rising and falling velocities for different sediment concentrations.

Different u' at the bottom were needed in order to lift-off the sediment depending on the sediment size, the larger the sediment size, the greater the u' required. This same linear relation was found in experiments dealing with compacting and with different resting periods (consolidation time). The first time that the samples from the Gulf of Lion were resuspended, they were as undisturbed as possible, this means that they had approximately the same consolidation as in the seabed. The second time they were resuspended within a few hours after the first time, they lacked consolidation due to such a short time period. In Figure 5-8, the difference between the u'_{cr} of undisturbed samples and the pre-resuspended samples from the Gulf of Lion is shown. These values are very useful to characterize a certain site. The u' required to resuspend the samples for the second time was between 63 and 87 percent lower than the first time. Concerning the relation between de minimum u' required to start the resuspension and the resting time of the sample between lift-off experiments, we found that a higher critical lift-off r.m.s. velocity u' is necessary as the time of consolidation increases. Silvester and Hsu (1993) mention that the erosion resistance of a bed of cohesive sediments increases as consolidation takes place over time, but it is less with waves than

for current alone. As duration of consolidation increases, the resistance due to these two sources of energy becomes similar. This increase is not infinite and has an upper limit at about the same u' required to resuspend the compacted undisturbed samples.

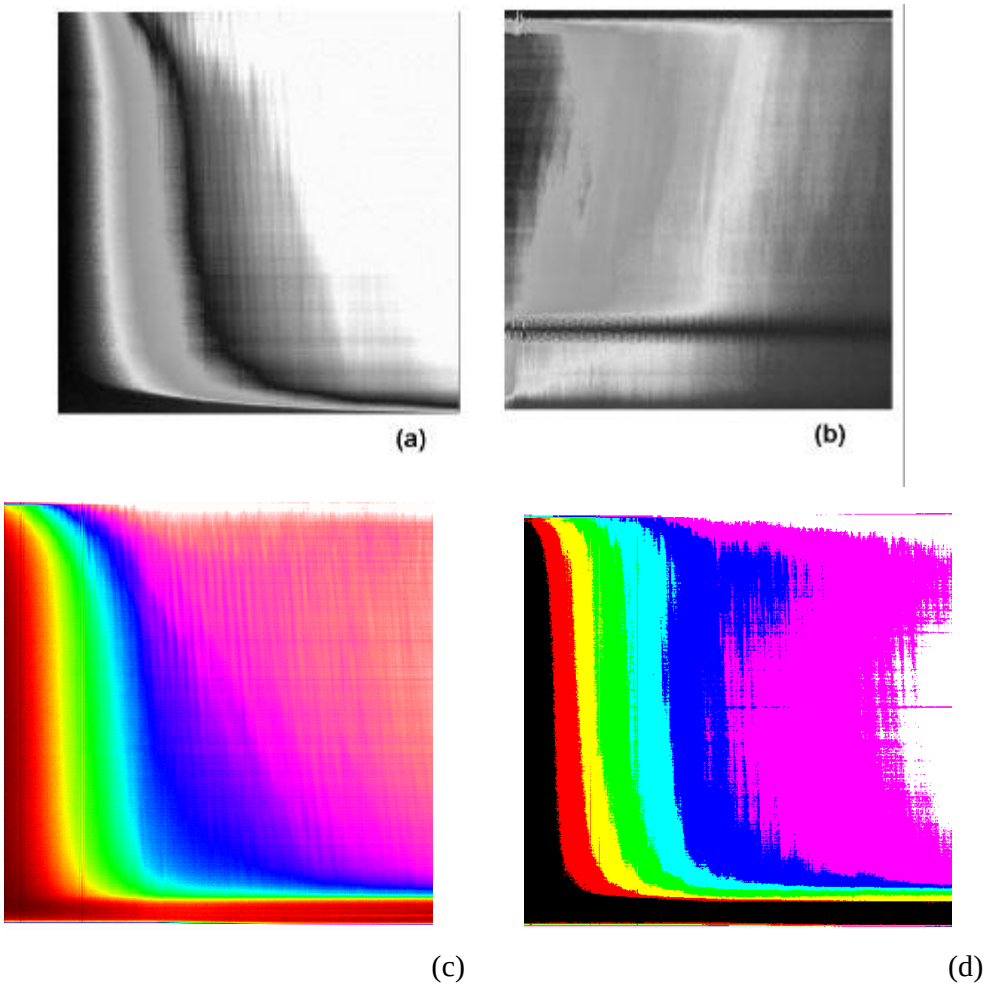

Figure 5-7.-Time series of sedimentation (a) and sediment lift-off (b). Vertical position of lutocline is represented in the Y-axis, and time is plotted on the X-axis. c) and d) are time series of sedimentation of different samples. False colour was applied to enhanced different SSC profiles using Digimage software.

When sediment was lifted off a lutocline was formed which advanced upward at a certain speed until equilibrium was reached forcing the lutocline to remain at a constant height (Figure 5-9). The upward speed and the height at which the lutocline stops are controlled by the frequency of oscillation of the grid (ω). An interesting observation that seems important is that the vorticity seems to remain constant at the

lutocline for a given sediment size independent of the grid's frequency, ω, this does not happen with u' at that same height (Figure 5-10 and Figure 5-11).

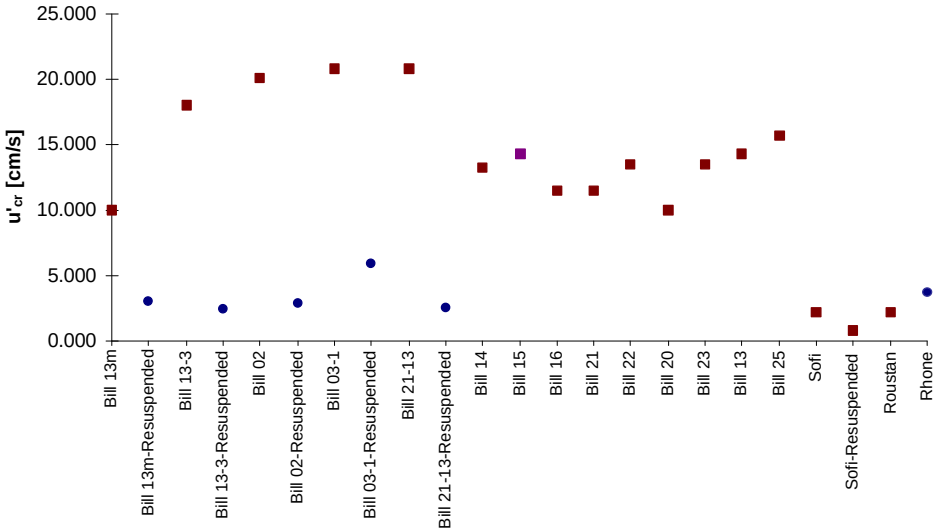

Figure 5-8.- The u'_{cr} for different samples from the Gulf of Lion. Undisturbed (■) and re-resuspended (●) samples. These values are very useful to characterize a certain site.

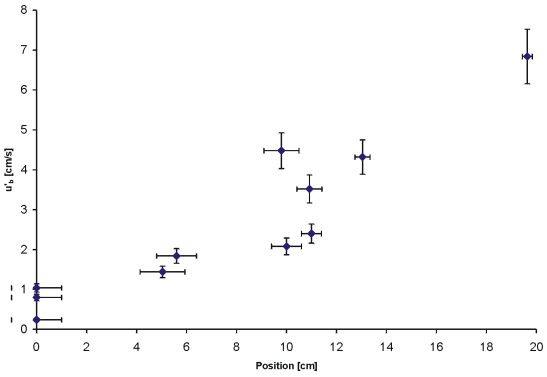

Figure 5-9.- The u' at the bottom and the corresponding height reached by the lutocline is shown (D50=0.26mm).

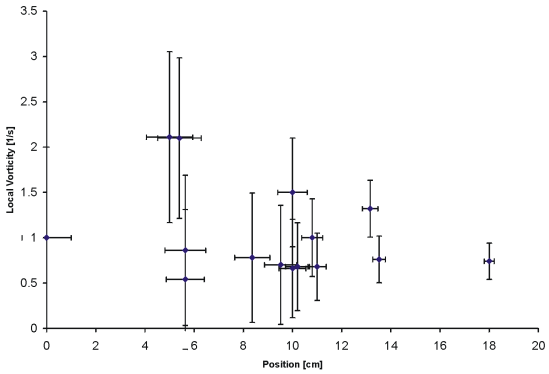

Figure 5-10.- The local vorticity at the lutocline position vs. lutocline height (D50=0.26mm).

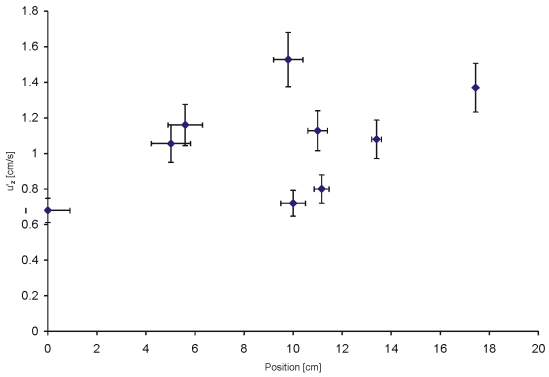

Figure 5-11.- The r.m.s. turbulent velocity u' at the lutocline position and the corresponding height reached by the lutocline is shown (D50=0.26mm).

5.2 Mass Flux

The tank is lit from behind to relate the decrease in transmitted intensity to the increase in suspended sediment concentration (SSC). The frequency was directly measured from the digitized images of the tank (See previous chapter). Those were processed recording the intensities of a given column with the maximum recording frequency given by the digitizing card (Figure 5-7). The maximum scanning frequency is 25 Hz, therefore the maximum measuring frequency is 12.5 Hz. The experimental work is based on the images of the tank. The experiments are recorded using a video tape. The images are then analyzed using the software package designed for fluid dynamic experiments Digimage (Dalziel, 1993), in combination with a specific code.

There is a wide range of experimental techniques that should be used to study different aspects of sedimentation and lift-off of sediments. To study the cohesivity it is interesting to change the frequency of the grid to find the minimum turbulent velocity needed to start the lift-off and relate it with the resting time of the sediment previous to the experiment.

The general procedure required to obtained the evolution of the concentration profile is as follows. The evolution of the tank is recorded. From the views a given column is chosen. A recording frequency is given and then a new time series image is constructed by putting each recorded column following the previous one, from left to right. An example time series of sedimentation is presented in Figure 5-7 a), c), d) and of lift-off in Figure 5-7 b)

To calibrate the concentration with the intensity a known volume of water and a controlled mass of dry sediment is taken. The sediment is mechanically mixed inside the tank using the same configuration in which the experiments are carried out. The concentration is given in parts per thousand (ppt) or parts per million (ppM) for different particle sizes. To find the distribution of sizes of our samples we have used a COULTER LS 100. These samples from the Ebro Delta had a mean size of 259.3μm, and the samples from the Lacaze Canyon (Gulf of Lion) had a mean size 6.6μm (for the Rhone, Sofi and Roustan samples properties see chapter 6).

To measure the velocity of advance of the density profile one possibility is to choose a set of heights and evaluate along the time at those points a magnitude which should detect the crossing of a change in concentration. For instance, the time derivative of concentration in a case of sedimentation, where we can follow the lutocline, and evaluate its velocity.

Another way to find the mass flux could be to choose a set of given concentrations and apply a filter to get its position at all times (Figure 5-13, Figure 5-14, Figure 5-15). We can see that at any height the change between the two values of concentration happens in an approximate constant time. We evaluate the mass flux from those values. Other possibilities may be tested. However, it is difficult to measure the

mass fluxes and the velocities in all cases using these methods because in most cases we do not have real passive tracers and the following restrictions apply:

- As we are restricted to a finite volume, the effect of the accumulation of the sediment that otherwise should have arrived beyond the top of the tank is that the background becomes uniformly darker. Then there is no match between concentration variation from flux variation and the intensity variation.

- Particles fall down with different velocities depending on their size and at the same time that other particles are rising. Therefore we can only work in the transient regime before the first particles reach the top of the tank.

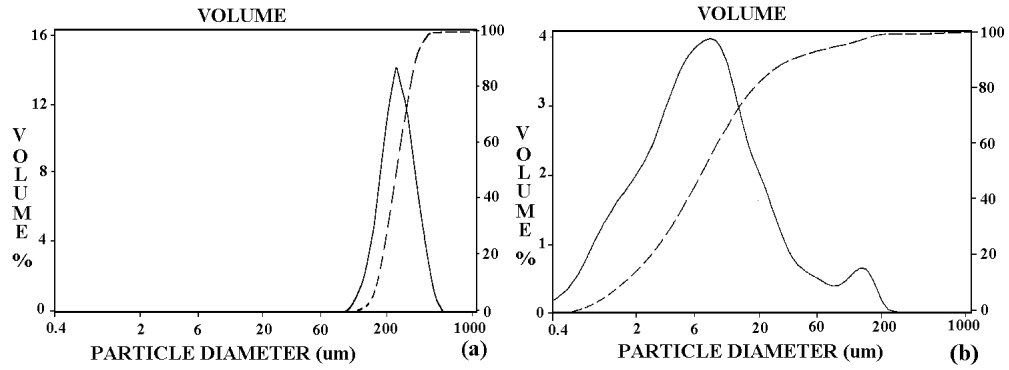

Figure 5-12.- Distribution of sizes taken from COULTER LS. Sample a) is from Ebro Delta with mean size 259.3 μm and sample b) is from Gulf of Lion with mean size 6.6 μm.

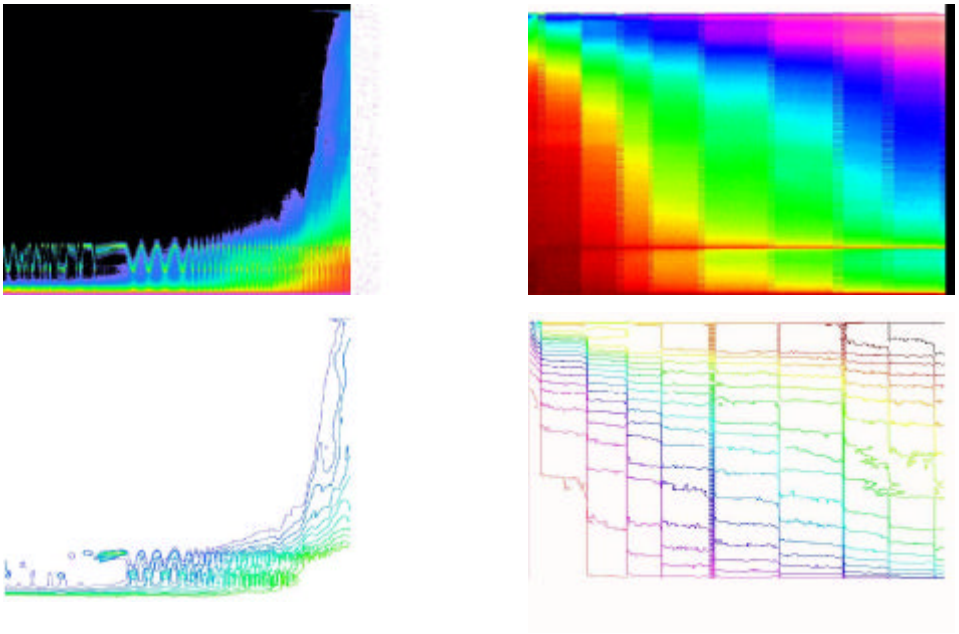

Figure 5-13.- Rhone sample (See next chapter for further information on sample properties). a) and b) are time series of resuspension. In a) the different SSC are represented in false colour, each colour represents a range of concentrations. b) is generated from a), each line represents a single SSC. c) and d) are the equivalent to a) and b) for sedimentation after resuspension. The difference between a)b) and c) d) is that the first two are continuous time series, whereas the other two are formed of several continuous time series (forming the different columns) taken with 5 minutes difference.

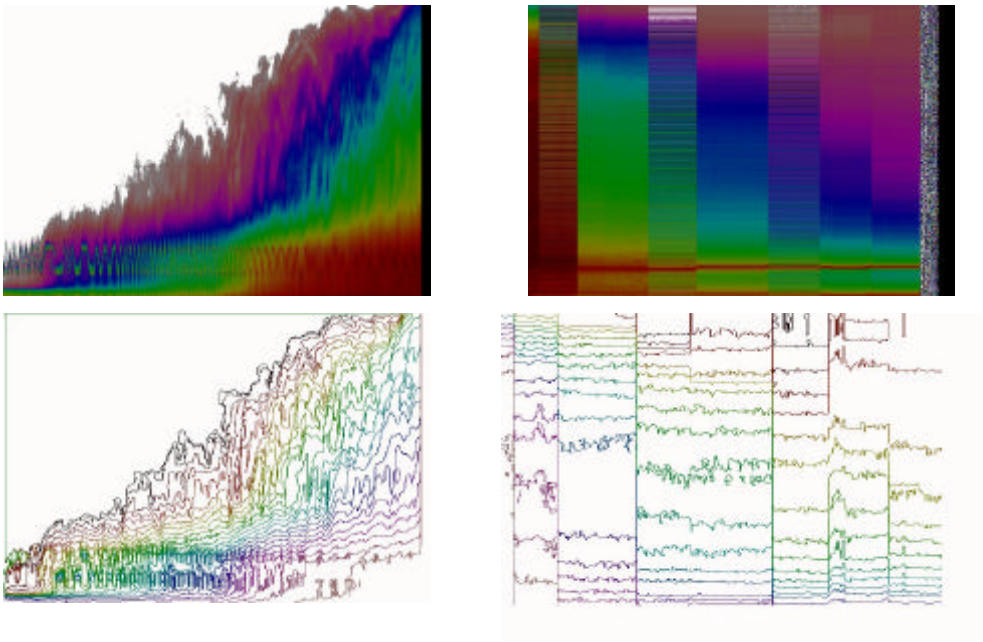

Figure 5-14.- Roustan sample (See next chapter for further information on sample properties). a) and b) are time series of resuspension. In a) the different SSC are represented in false colour, each colour represents a range of concentrations. b) is generated from a), each line represents a single SSC. c) and d) are the equivalent to a) and b) for sedimentation after resuspension. The difference between a)b) and c) d) is that the first two are continuous time series, whereas the other two are formed of several continuous time series (forming the different columns) taken with 5 minutes difference.

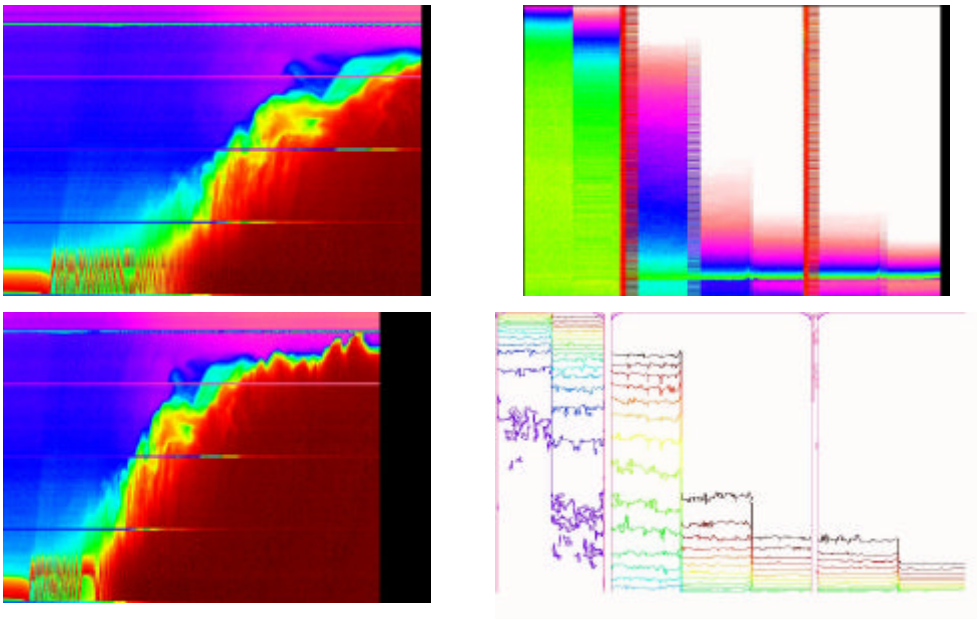

Figure 5-15.- Sofi sample (See next chapter for further information on sample properties). a) and b) are time series of re-resuspension. The different SSC are represented in false colour, each colour represents a range of concentrations. c) is equivalent to a) and b) for sedimentation after re-resuspension. d) is generated from c), each line represents a single SSC. The difference between a)b) and c) d) is that the first two are continuous time series, whereas the other two are formed of several continuous time series (forming the different columns) taken with 5 minutes difference.

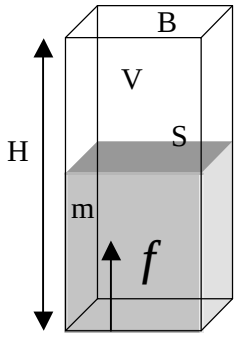

Figure 5-16.- Model proposed for the evaluation of the mass flux from conservation of mass. m is mass, V volume, S surface limiting V, B top/bottom surface, H height, c concentration and f mass flux.

The technique proposed by Sánchez and Redondo (1998) and used in this work takes advantage of the conservation of mass.

Then

$$\frac{d}{dt}m = \iint_S f\, ds - \iint_B f\, ds \tag{5-6}$$

$$m = \iiint_V c\, dv = \iint_B \left[\int_H c\, dz\right] ds \tag{5-7}$$

where m is the mass in a volume V with a boundary surface S, top and bottom surfaces B, height H, c the concentration, and f flux of mass. From equations (5-6), (5-7) it follows

$$\frac{d}{dt}\left[\int_H c\, dz\right] = f \tag{5-8}$$

Then we can determine the mass flux f as

$$f = H\frac{d}{dt}\langle c\rangle_H \tag{5-9}$$

where $\langle c\rangle_H$ is the concentration averaged on a column. This procedure may give values of the vertical transport of sediments as a function of the local r.m.s. velocity fluctuations at the sediment bed. The flux f=0 for $u' < u'_{cr}$, and drops to zero as time goes to infinity because of the saturation and the limited amount of energy available for the suspension of the sediment. We assume the flux to be the maximum reached. In Figure 5-17 a) we present a time series where the jumps in the frequency are marked as increases in illumination. the analysis is presented in Figure 5-17 b).

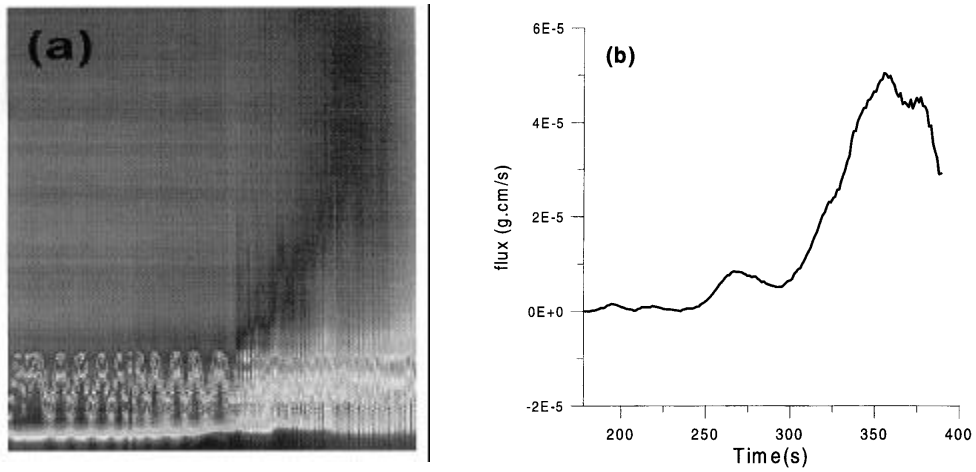

Figure 5-17.- Evolution of the mass flux. a) is a time series of a lift-off and b) is its associated mass flux *versus* time. The value taken is the maximum.

5.3 PRACTICAL CASE: Sediments from the Lacaze Canyon, Gulf of Lion.

In this section sediments extracted from the Lacaze Canyon at the Gulf of Lion are studied to see which of the sediment components has a greater influence hampering erosion. The u'_{cr} for each sample was determined by means of grid-stirred analysis as described before. The results are compared with the different sediment properties in order to find the main factor that hampers erosion (lift-off). Also, an analysis was done to determine the probable mass flux (as described above) in the region where the samples were extracted.

A total of 9 cores extracted from the Gulf of Lion where studied. The general procedure, after the cores were received in the laboratory in Barcelona, was to cut a 1 cm thick disk of the upper part of each core. The disk was gently deposited at the bottom of the mixing box. Water was poured in the box letting it slide very slowly down the wall of the box so as not to disturbed the sample surface. The rest of the procedure was as described in section 5.1.2 “Sediment Lift-off Experiments”. Thus, the u'_{cr} for lift off (in the case of cohesive sediments u'_{cr} for motion initiation is equal to u'_{cr} for lit off) was obtained for each sample.

Simultaneously to this procedure, a small amount of the undisturbed sample was analyzed in the University of Perpignan for percentage of sand [>50µm], sample median size [<50 µm], sample main mode size[<50µm], percentage of main mode [<50 µm], sample secondary mode size [<50 µm], percentage of secondary mode [<50µm], percentage of fine fraction [<0.3µm], percentage of water content [water/dryW], percentage of water content [water/HumW], percentage of total clays, percentage of total detritic, percentage of total Calcite, percentage of Illite[<2µm], percentage of Chlorite [<2µm], percentage of Kaolinite [<2µm], PlasticityIndex and LiquidityIndex.

In Figure 5-18 a), the value of the u'_{cr} found for each sample is plotted. As it could be seen, the values range is between 10 and 16 $^{cm}/_{s}$. The samples are plotted in order of increasing depth from left to right (Figure 5-18 b)). Since no direct relationship

could be seen between r.m.s. velocity and depth (see also Figure 5-18b)), the u'_{cr} values obtained were plotted against the other sample properties listed above.

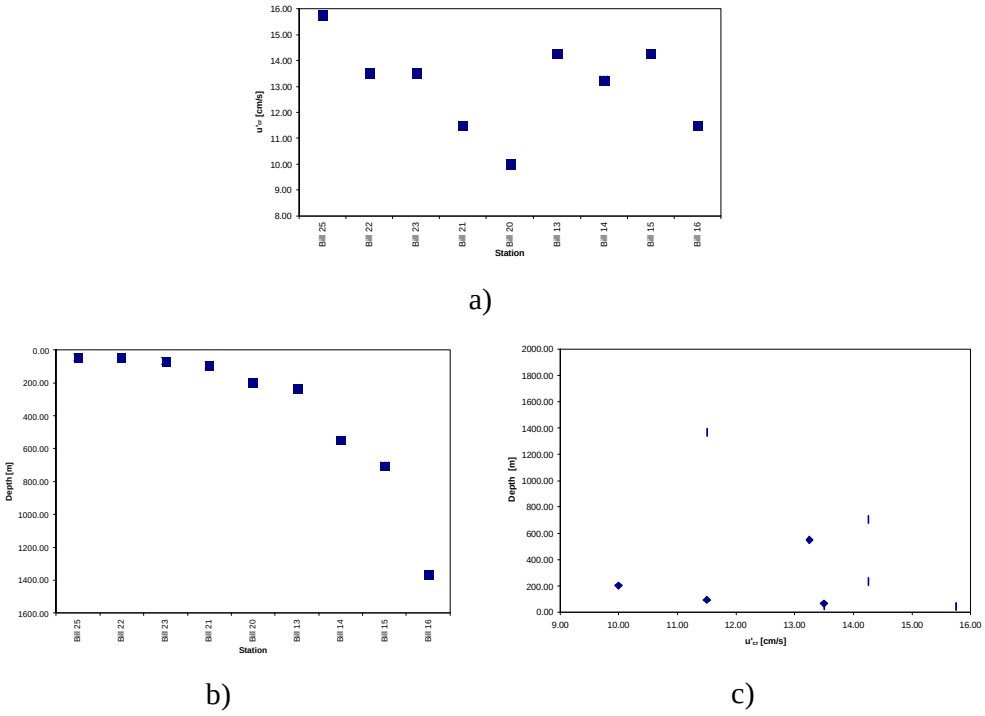

Figure 5-18.- a) u'_{cr} for the Lacaze Canyon samples. b) Shows the depth of the samples. c) u'_{cr} vs. depth. No evident relationship between these two parameters is observed.

The relationship between u'_{cr} and the different sediment size components presented in each sample are analyzed in Figure 5-19. As in Figure 5-18, no evident relationship between these parameters is observed. All the plotted parameters seem to have a value roughly constant that does not change with depth. For the sand percentage, the two samples with the higher percentage are at mid depth, and the third is the shallower one.

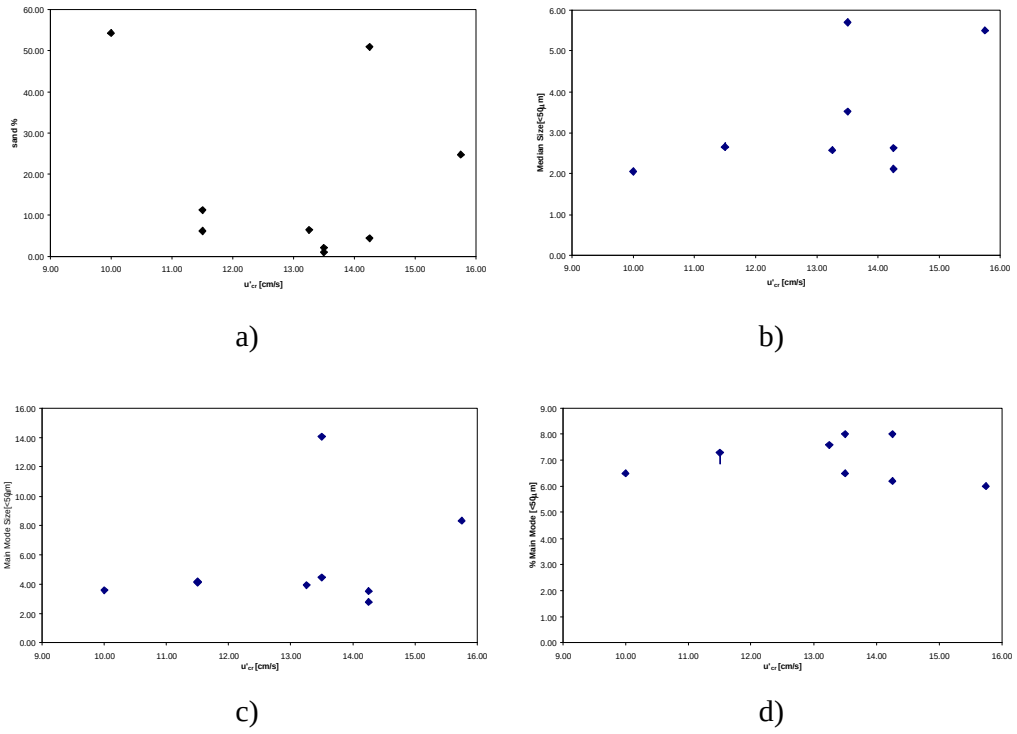

Figure 5-19.- Relationship between u'_{cr} and sediment size components.

The relationship between u'_{cr} and sediment contents of clay minerals and detrital components is analyzed in Figure 5-20 since sediment contents of clay minerals is responsible for cohesiveness. As in Figure 5-18 and Figure 5-19, no evident relationship between these parameters is observed.

The relationship between u'_{cr} and sediment physical properties (plasticity and liquidity index) is analyzed in Figure 5-21. As in Figure 5-18, Figure 5-19 and Figure 5-20 no evident relationship between these parameters is observed. The liquidity index seems to be about constant for all samples.

In view of the fact that no direct relationship between u'_{cr} and any of the parameters analyzed was found, another approach was carried out. All the u'_{cr} for sediment lift off obtained during the development of the present work that corresponded to sediment samples extracted from the Gulf of Lion, were put together in Figure 5-8. When the plotted values corresponding to undisturbed sediment (■), where analyzed, three different groups were found. The first one, from left to right, was composed of five samples. The second one corresponded to the nine samples analyzed in this section.

And the third one with three samples which are described in the next chapter. The first group of samples where analyzed about two years after they were extracted. The second group were analyzed a few months after they were extracted from the sea bottom, whereas the third group was analyzed within the next 12 hours subsequent to their extraction and much care was put on not disturbing the sediment sample surface. We found that there is a direct relationship between the time span that exists since the sample is extracted and the time when it is analyzed and the u'_{cr} .

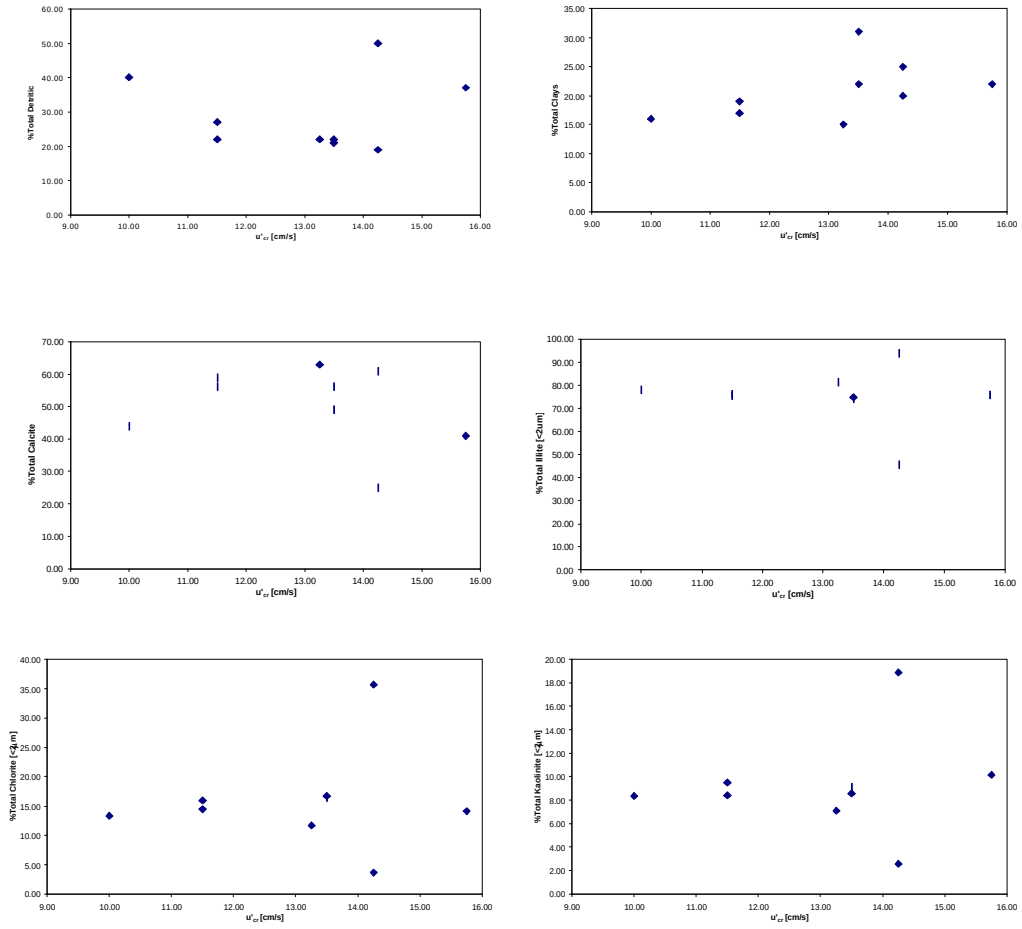

Figure 5-20.- Relationship between u'_{cr} and sediment contents of clay minerals and detritical components.

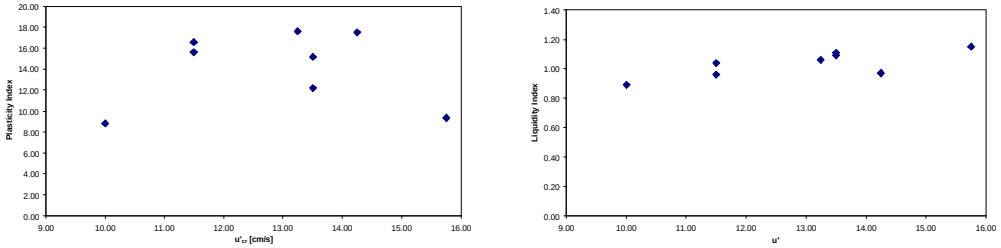

Figure 5-21.- Relationship between u'_{cr} and sediment physical properties (plasticity and liquidity index).

Chapter 6

TURBULENT SEDIMENT RESUSPENSION IN SHEARED AND ZERO-MEAN FLOWS

Dynamical processes associated with the initial lift off of sediments from the sea bottom in the benthic layer and the ways in which turbulence maintains the sediment in suspension are poorly understood due to their complexity. An important factor is that the entrainment at the sediment interface or at a lutocline is affected by the r.m.s. turbulent velocity that depends on the local velocity shear because the value of the mean velocity at the sediment bed is always zero. Predictions of sediment transport rates are found to differ by several orders of magnitude. This results from attempting to describe a very complex problem too simplistically, without first acquiring at least a qualitative understanding of all the transport mechanisms involved (Jones S.E., Jago C.F. and Simpson J.H., (1996), Redondo J.M., et.al. (1995), Sánchez and Redondo (1998)).

We present results on two series of laboratory experiments where an initially stable sediment layer is stirred by either a lateral current (Shaaff (1999)) or a grid generated zero mean turbulent flow (Tsai and Lick(1986), Redondo(1987)).The mechanism of reentrainment (lift off) of sediment under the grid is a mechanical one, driven by the Reynolds stress acting on the bed of particles, and in this respect it is similar to the shear stress criterion that has been used to described the entrainment of particles from the bed in channel flows or turbidity currents (Huppert, Turner and Hallworth, 1995). The two laboratory experiments were designed to compare sediment lift off produced by zero mean turbulence and sheared flows and were performed on recently extracted cores from three sites in the Gulf of Lion.

6.1 Description of sediment samples and field data

Sediment cores were collected at three sites in the Gulf of Lion, which are characteristic of the major sedimentary units of the continental shelf (Figure 6-1). The Roustan station (43°18.28N, 4°50.18E, 40 m depth) is located on the Rhone river prodelta. The Rhone station (43°14.53N, 4°53.10E, 98 m depth) is located at the edge of the mid-shelf muddy belt, and the Sofi station (43°04.00N, 5°07.60E, 160 m depth) is located on the outer shelf.

The cores were collected with a Bowers & Connelly MarkVI multicorer, which is an adaptation of the one described in Barnett et al. (1984). This multicorer was equipped with 4 polycarbonate tubes with an inner diameter of 15 cm, which normally collects virtually undisturbed cores of 15-30 cm in length with clear overlying water. Cores that were turbid or disturbed were discarded. A minimum of 6 cores was obtained at each site. After retrieval on deck, the upper opening section of the tubes was hermetically sealed and stored vertically until further handling. The purpose was to disturb the natural characteristics of the benthic layer as little as possible.

6.1.1 Sediment porosity

For each site, one of the cores was sectioned into 1 cm slices. The sediment slices were weighed, freeze-dried and re-weighed. The sediment porosity is determined as $P = (\alpha/\rho_w) / ((1-\alpha)/\rho_s + \alpha/\rho_w)$, where α is the water content, ρ_s the sediment density (2645 kg m^{-3}) and ρ_w the pore water density (1038 kg m^{-3}). The Roustan and Rhone samples have similar porosities with an average value on the first centimetre of 0.80. The Sofi sample is clearly different with an average porosity of 0.57 within the first centimetre.

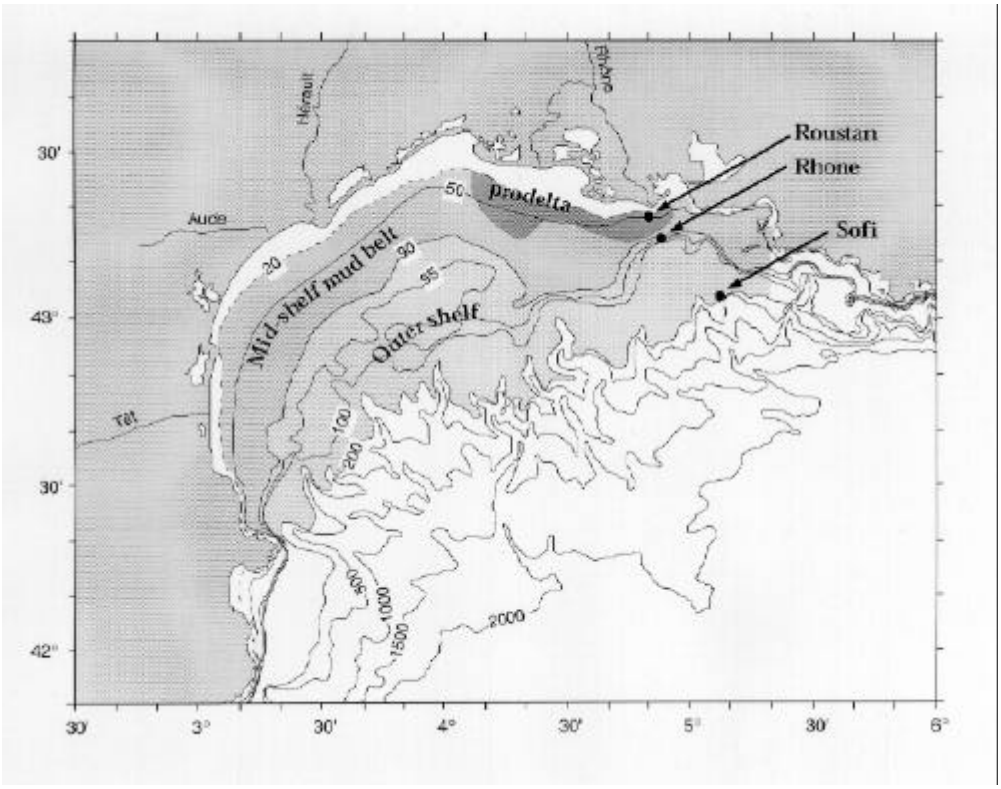

Figure 6-1.- Map of the Gulf of Lion, showing the bathymetry and the sediment extraction sites.

6.1.2 Sediment grain size

The sediment grain size in the first centimetre of the cores was measured with a laser particle size analyser (Table 6-1). Sediment on the prodelta (Roustan station) was composed of 22% clays, 71% silts and 7% of very fine to fine sand. Sediment from the Rhone station was composed of 33% clays, 66% silts and 1% of very fine to fine sand. Sediment from the Sofi station was composed of 30% clays, 56% silts and 14 % of very fine to medium sand.

The increase of the sandy fraction at the Sofi station is due to the outcropping of relict sand on the outer shelf. The increase in the content of silt between the Roustan and the Rhone stations could be the result of a decantation of the finer particles as a function of the distance from the Rhone river outlet as well as to an increase in depth.

Table 6-1.- Sediment size of each of the samples.

	Station		
	Roustan	**Rhone**	**Sofi**
Mode (μm)	15.76	9.76	7.80
Median (μm)	13.03	7.31	9.55
Skewness	0.84	0.71	1.08
Sand %	7	1	14
Silt %	71	66	56
Clay %	22	33	30

6.2 Experiments

6.2.1 Experiments with Shear Flow

These experiments were performed entirely at the installations of the Oceanographic Centre of Marseille (Centre D'Océanologie de Marseille) in France. A rectangular PVC channel (0.4 m wide, 3 m long, and 0.4 m high) was used adapted from Cole et al. (1992) and is described in detail in Shaaff (1999). A motor drove the water between the ends of the channel through a return pipe (Figure 6-2). The test section of 0.016 m^2 surface (0.4 x 0.4 m) was positioned 2.1 m downstream of the channel entry. According to Nowell and Jumars (1987), the water depth in the channel was fixed to 10 cm so that the sidewall effects may be neglected. Two honeycomb baffles of 4 cm thick and a 1 mm mesh grid, located at 30 cm from the flow outlet, attenuate the turbulent motions and homogenize the velocities. Velocity measurements were performed in order to determine the vertical velocity profiles both above the Perspex bottom and the sediment samples. The experiments are described in detail in the following sections. All the experiments were performed using seawater at about 15.7°C.

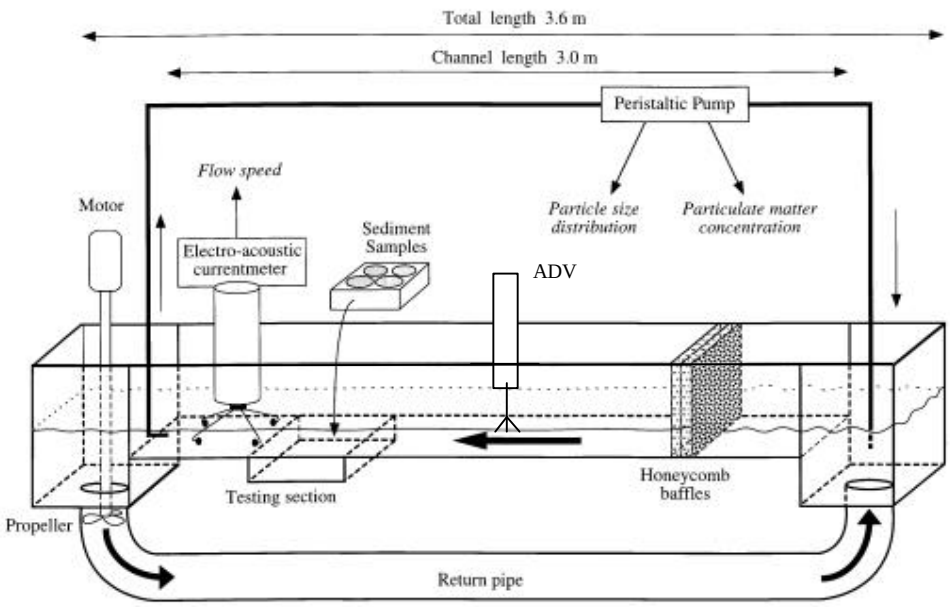

Figure 6-2.- Recirculation tank at the Oceanographic Centre of Marseille (Centre D'Océanologie de Marseille), where the shear induced sediment lift off was studied.

6.2.1.1 Equipment

Velocities were measured in two points simultaneously. The flow velocity at 4 cm above the bottom was measured with a Meeres-Electronik Gmbh (ME) acoustic currentmeter at 5 Hz downstream of the testing section during all the experiments. A *Nortek* Acoustic Doppler Velocimeter (ADV) (described in chapter 3) was used to obtain a detailed description of the turbulent flow over the sediment for a stabilized reference mean flow speed in the channel, as well as over the Perspex bottom before the sediment samples. It was also used to measure the velocities 3 cm above the samples during the lift off threshold velocity experiments. The ADV measured, the three components of the velocity within a volume of 0.5 cm^3, at a rate of 25 Hz.

Water samples were collected next to the ME at 1 cm above the bottom with a peristaltic pump (flow rate of 1 liter min^{-1}) to measure the suspended sediment concentration (SSC). Total particulate matter concentration (TPM) was determined by low-vacuum filtration of 500 ml on pre-weighted Whatman GF/C (47 mm diameter, 1.6 µm pore size), rinsing the filter with milliQ water to remove salt, drying (60°C, 24 h) and re-weighed. Particle size distribution was estimated with a portable laser

granulometer MET-ONE (WGS-267 model). Six size classes were recorded: < 2 µm, 2-5 µm, 10-50 µm, 50-100 µm, 100-200 µm.

6.2.1.2 Tank Calibration Measurements

In order to determine the velocity profiles between the Honeycomb baffles and the test section and to compare the measurements of both courrentmetres, a compete set of velocity measurements was performed. Measurements were taken as follows:

6.2.1.2.1 Vertical profile above the Perspex bottom.

A complete vertical velocity profile was measured above the Perspex bottom of the tank between the Honeycomb baffles and the sediment samples. The measuring point was located at 120 cm from the Honeycomb baffles in the centre line of the tank. The velocities were measured at eleven points separated 0.5 cm (z = 0.2, 0.5, 1.0, 1.5, 2.0, 2.6, 3.1, 3.5, 4.1, 4.6, and 5.2 cm). Each measurement was taken during 1 minute with the ADV at 25 Hz. The mean velocity during all measurements was of 20 $^{cm}/_{s}$.

6.2.1.2.2 Transversal profile above the Perspex bottom.

A complete transversal velocity profile was measured above the Perspex bottom of the tank between the Honeycomb baffles and the sediment samples. The measuring point was located at 120 cm from the Honeycomb baffles in the centre line of the tank. The velocities were measured at six points at 6.0, 11.0, 15.5, 21.0, 26.0 and 30.5 cm from the right wall of the tank. Each measurement lasted 1 minute. The ADV was placed at 3 cm from the bottom and the sampling rate was 25 Hz. The mean velocity during all measurements was 22 $^{cm}/_{s}$.

6.2.1.2.3 20 min series above the Perspex bottom.

In a second stage, the ADV was positioned at 0.5 cm above the Perspex surface to measure current velocities during 20 minutes at 25 Hz.

6.2.1.2.4 Comparison between the ME and the ADV measurements.

To compare the measurements of both courrentmeters, simultaneous measurements were carried out 10 cm apart one from the other at a distance of 3.0 cm from the bottom.

6.2.1.3 Lift off threshold velocity experiments.

This set of experiments was implemented in order to measure the bottom friction threshold velocity needed to lift off undisturbed sediment samples from tree different sites of the Gulf of Lion. The methodology described next was systematically repeated in the analysis done to the three samples collected from sea bottom. The order of performance was as follows:

6.2.1.3.1 Sample manipulation:

The upper part of the sediment cores and overlying water collected from the sea bottom were slid into a tube 10 cm high (15 cm diameter), with a minimum of perturbations. Four cores from the same site were fitted within the testing section and a punched plate was adjusted to cover the remaining openings (Figure 6-2). The surface of the cores was in the same plane as the rest of the tank bottom.

6.2.1.3.2 Measurements above samples.

Velocity was measured throughout the experiment at 3 cm above the sediment using the ADV at 25 Hz. The flow speed increased gradually by steps of approximately 2.5 $^{cm}/_{s}$ from 2 $^{cm}/_{s}$ up to 34 $^{cm}/_{s}$. During each step, that lasted 8 minutes, water samples for particulate matter concentration and particle size distribution analyses were taken 2 and 5 minutes after each speed increment. Water sampling was done near the ME.

6.2.1.3.3 Calibration velocity measurements

Vertical profile above sediment.

A detailed vertical velocity profile was measured above each sediment sample (Roustan, Rhone, Sofi) at a constant velocity. The measurements were performed at the centre line of the tank. The vertical shear of the horizontal current was obtained by measuring the current velocities at 9 levels above the sediment (0.2, 0.5, 1, 1.5, 2, 2.5, 3, 3.5 and 4 cm). Each profile measurement lasted 1 minute.

Time series above sediment.

A time series was measured using the ADV, with a sampling rate of 25 Hz, and at 0.5 cm above the samples during 20 minutes.

6.2.2 Experiments with Zero Mean Flow Turbulence

These experiments were performed entirely at the installations of the Oceanographic Centre of Marseille (Centre D'Océanologie de Marseille) in France, and the respective analyses were performed at the Fluid Dynamics Laboratory of the Applied Physics Department of the Technical University of Catalonia (Laboratorio de Dinámica de Fluidos del Departamento de Física Aplicada de la Universidad Politécnica de Cataluña) in Barcelona, Spain.

6.2.2.1 Equipment and Tank Calibration Measurements

The experimental apparatus is the same used by Medina, Sánchez and Redondo (2001) (described in chapters 4 and 5) which is similar to that described by Turner (1968), Thorpe (1966), Turner (1973), Thompson and Turner (1975), Hopfinger and Toly (1976), Xuequan and Hopfinger (1987), Tsai and Lick (1987), Noh and Fernando (1991), Huppert, Turner, and Hallworth (1995), Redondo, Sánchez, Castilla (1995), Peters and Redondo (1997), Sánchez and Redondo (1998), Redondo and Sánchez (1999), Mann, Ott and Andersen (1999), Ott and Mann (2000), Redondo and Sánchez (2000), Matas and Redondo (2000), among others.

Xuequan and Hopfinger (1987), Tsai and Lick (1987), Noh and Fernando (1991), Huppert, Turner and Hallworth (1995), Redondo and Sánchez (2000), Matas and Redondo (2000), Medina, Sánchez and Redondo (2001) used grid stirred turbulence to study sediment behaviour as described in the previous chapters.

The tank was lit from behind and the experiments recorded using a compact PAL system VHS-C colour video camera (JVC, GR-AX200). The images were analysed using Digimage (Dalziel, 1993), a software package specially designed for fluid dynamic experiments. This software operates using a Data Translation Card DT-2861 on a P.C. computer. The oscillation frequency of the grid is measured directly from the digitized images and the suspended sediment concentration is estimated by relating a range of known concentrations to their measured attenuation of light intensity. At the beginning, the grid was oscillated at a low frequency (3 Hz), which gradually increased until sediment lift off was observed. The oscillation frequency at the moment of the lift off was registered as the threshold frequency. In most of the experiments lift off is rather abrupt, this behaviour minimizes the error on determining the threshold frequency. This frequency was used later on to determine the critical turbulent r.m.s. velocity, u', needed to lift off each sample.

The relevant turbulent parameters, integral length scale, ℓ , and r.m.s turbulent velocity, u', for these mixing boxes have been taken from previous measurements (Sánchez and Redondo, (1998), Medina, Sánchez and Redondo (2001)) as a function of the distance between the grid centre of oscillation and the distance to the interface (sediment surface), z , the grid's mesh, M , and the stroke, s , and its frequency, w , following other parameterizations such as Xequan and Hopfinger (1995) and Sánchez and Redondo, (1998) as:

$$\ell = b\,z \tag{6-1}$$

$$u' = c s^{3/2} M^{1/2} w z^{-1} \tag{6-2}$$

With fitted value $C = 0.6$. This constant is a function of the type of grid (M, s, w, z), and its solidity ($S = 0.61$).

6.2.2.2 Sample manipulation

Two subsamples were taken from one core from each site mentioned above. The first one (9.2 x 9.2 x 5 cm) was taken from the surface of the core, with a square PVC corer made especially for this experiment, being careful not to disturb the sample surface maintaining some water on top. A square lid was slid under the corer to keep the sample in place while it was transported to the grid mixing box. The corer with the subsample was placed at the bottom of a 10 x 10 x 35 cm transparent Perspex mixing box (Medina, Sánchez and Redondo, 2001) shown in Figure 6-3. The oscillating grid with an 0.8 cm mesh and a 0.3 cm bar width was placed at 2.95 cm above the sample surface. The second subsample was obtained from the same three cores used before in order to calibrate the suspended sediment concentration as a function of the light intensity transmitted from the back of the box and recorded in the video, following the procedure described in Sánchez and Redondo (1998).

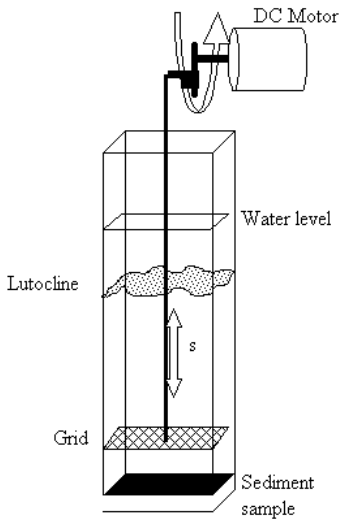

Figure 6-3.-. Experimental apparatus used for the zero mean flow experiments.

6.3 Results

In this section we present the results obtained from the two different sets of experiments (1) with shear flow and with (2) turbulence with zero mean flow) and these will be compared and discussed in the next section “Discussion and Conclusions”.

6.3.1 Results of the Experiments with Shear Flow

Measurements where performed to determine the flow behaviour in the recirculation tank. In order to do so, velocity profiles at constant speed where obtained, both above the Perspex bottom (vertical and transversal) and vertically above the samples from the three sites. Other measurements were performed to achieve this goal, and to be able to compare the measurements from both currentmeters. These results are presented first. Velocity measurements above the sediment samples where also performed to determine the lift off threshold velocity. These results are presented next with the results of the particulate matter concentration and particle size distribution measurements. Some other results derived from the direct velocity measurements as the shear velocity estimation at the bottom, u_*, are also presented in this section.

6.3.1.1 Tank Flow Measurements

6.3.1.1.1 Vertical velocity profile above the Perspex bottom

A complete vertical velocity profile was measured above the Perspex bottom of the tank between the honeycomb baffles and the sediment samples. In Figure 6-4 a), the mean velocity, $\bar{u}$, is plotted against its position in height. The profile has two segments well differentiated. The four lower points (0.5 to 1.5 cm from bottom) behave as the expected logarithmic profile, while the rest of the points fluctuate around a constant value. All points in the upper part of the velocity profile had a lower value for the $\bar{u}$ than those at the bottom. In Figure 6-4 b), the 3 components of the mean velocity are plotted. The values for $\bar{v}$ and $\bar{w}$ are about zero and remain constant for the entire profile.

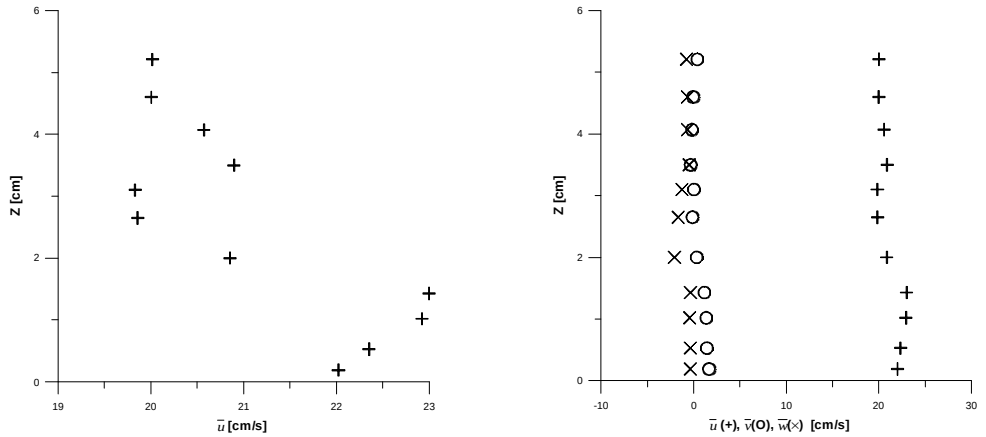

a) b)

Figure 6-4.- Mean velocity vertical profile above the Perspex bottom. a) $\overline{u}$ Vs. height. b) $\overline{u}$ (+), $\overline{v}$ (O), $\overline{w}$ (×) Vs. height.

At the same height where the expected logarithmic mean velocity profile has a maximum, the profile of the u component of the standard deviation, σ_u, (Figure 6-5 a)) has a maximum. In the remaining profile the σ_u fluctuates near a value equal to 2. In Figure 6-5 b) the 3 components of the standard deviation, σ, are plotted. It is seen that σ_u and σ_v had the same behaviour, while σ_w has a linear behaviour. This means that the main fluctuations are in the horizontal plane while the vertical plane is not being affected by them.

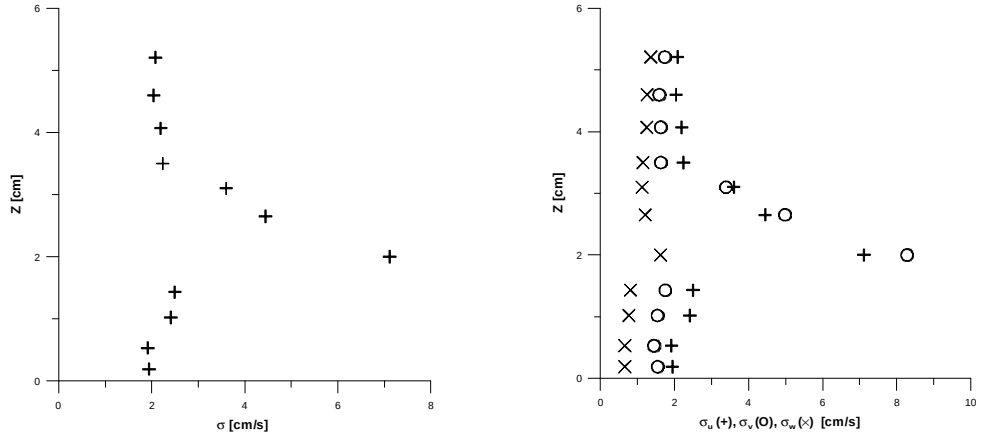

a) b)

Figure 6-5.- Velocity standard deviation vertical profile above the Perspex bottom. a) S Vs. height. b) S u (+), S v (O), S w (×) Vs height.

A possible explanation for the maximum at the mean velocity and σ profiles, and for the higher velocities present at the bottom, seems to be the position of the return pipe and the geometry of the tank. This is discussed in detail further on in this chapter.

6.3.1.1.2 Transversal velocity profile above the Perspex bottom.

A complete horizontal velocity profile was measured above the Perspex bottom of the tank between the honeycomb baffles and the sediment samples. In Figure 6-6 a) the mean velocity, $\bar{u}$, is plotted against its horizontal position to determine its position from the right wall of the tank. At the points where velocity was measured, the speed fluctuated around a constant value for the entire sample section. In the same figure, a schematic adjusted profile, assuming u = 0 at the wall, is plotted. It is clear from this adjustment that the effect of the wall is rapidly lost within the first centimetres. Something similar is plotted in Figure 6-7 a) where the standard deviation is shown. The effect of the wall is not lost as fast as for the $\bar{u}$. The segment of lower σ is restricted to a narrow area at the centre of the tank.

In Figure 6-6 b) the 3 components of the mean velocity are plotted. The value for the $\bar{v}$ and $\bar{w}$ components remains constant near zero as expected in this kind of flows.

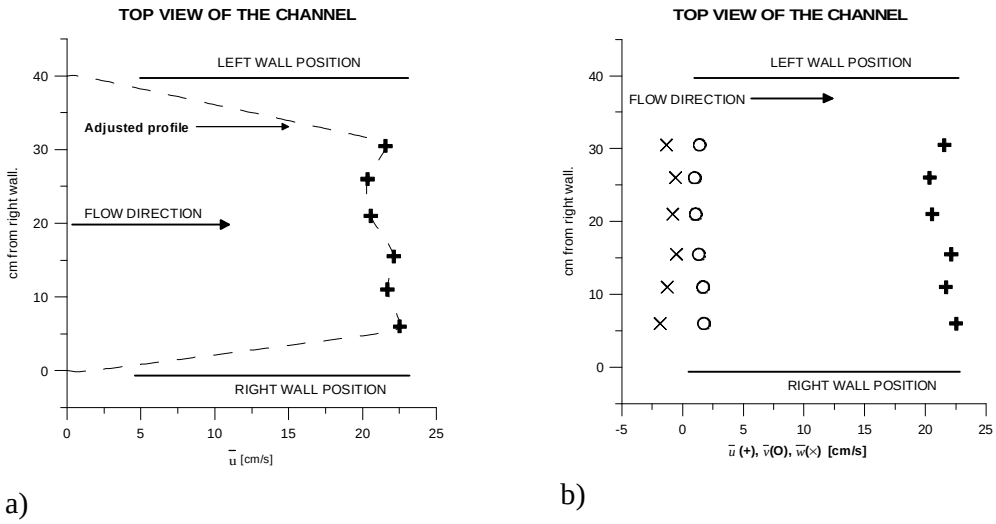

Figure 6-6 .- Horizontal velocity profile above the Perspex bottom. $\bar{u}$ Vs. distance (to right wall). + Measure velocities. ---- Schematic adjusted profile assuming u = 0 at the wall.

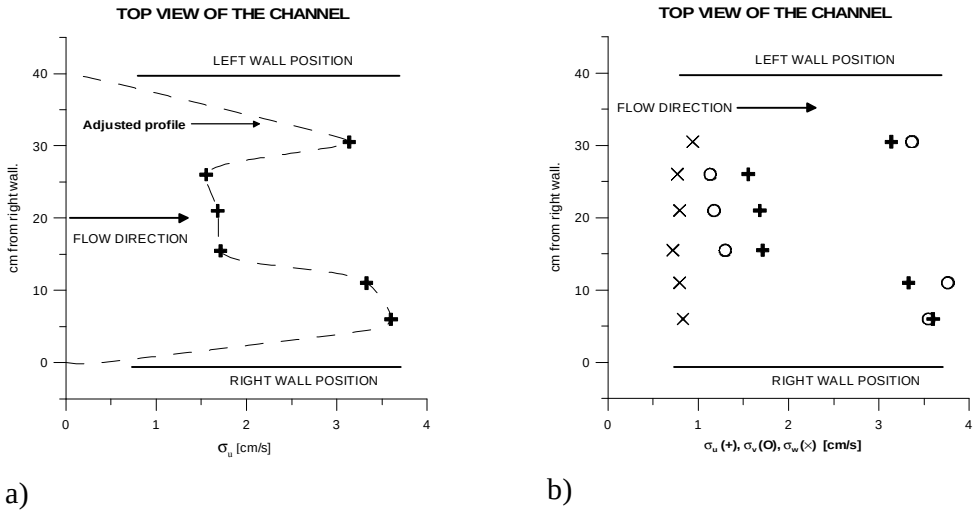

Figure 6-7 .- Horizontal velocity profile above the Perspex bottom. σ Vs. distance to right wall. + Measure σ. ---- Schematic adjusted profile assuming u = 0, σ = 0 at the wall.

In Figure 6-7 b), the 3 components of σ are plotted. As for the vertical profile, the *u* and *v* components (horizontal plane) have the same behaviour, while σ_w has a constant value lower than that for *u* and *v*.

6.3.1.1.3 Time series above the Perspex bottom.

The instant velocities of the 3 components at 0.5 cm for the Perspex bottom are plotted in Figure 6-8. The main flux is in the u direction. The values of the *u* component fluctuate around 20 $^{cm}/_{s}$. The values of the *v* component are 10 times smaller than for the u component probably due to some up-flow asymmetry at the inlet, and the values of the w component fluctuate around 0.0 $^{cm}/_{s}$.

6.3.1.1.4 Vertical velocity profile above the sediment samples.

A vertical velocity profile was taken above each sediment sample at constant speed. The results of these measurements are shown in Figure 6-9 and Figure 6-10. The mean velocity profiles (Figure 6-9) show that at the testing section the discontinuity of the profile seen in Figure 6-4 is no longer present. This is probably due to the fact that the distance from the honey comb baffles to the testing section is long enough for the flow to stabilize. The former is not true for the standard deviation of the velocity. Figure 6-5 and Figure 6-10 (a, b, c) present the same behaviour. The standard deviation of u

,σ_u, is about one order of magnitude smaller than the mean velocity, $\overline{u}$, present at the same height. The difference between the standard deviation and the mean u is greater as the distance from the bottom increases. The standard deviation has a tendency to a constant value up to 2.5 cm from the bottom where the highest value is found in the three samples, decreasing afterwards with height. While the $\overline{u}$ changes with height, the $\overline{v}$ and $\overline{w}$ components are almost constant, near 0.0 cm/s, for the three samples.

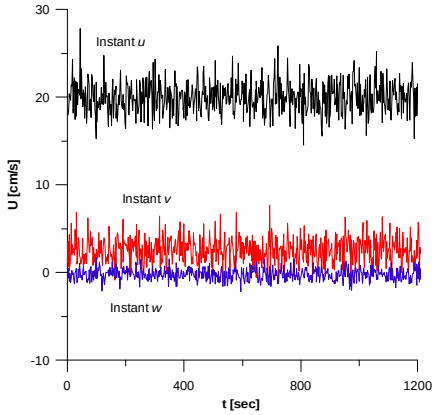

Figure 6-8 .- Instant velocities of the 3 velocity components measured at 0.5 cm above the Perspex bottom (ADV – 25Hz).

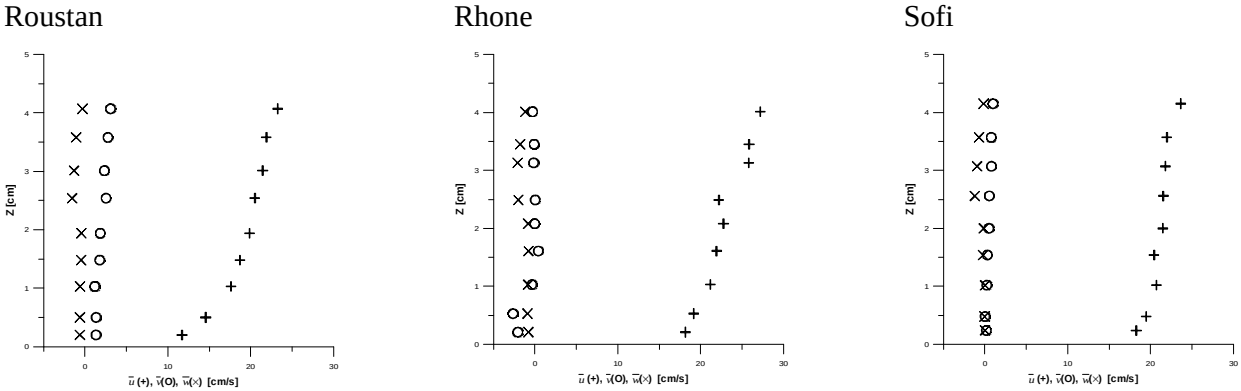

Figure 6-9.- Mean velocity vertical profile above the sediment samples. $\overline{u}$ (+), $\overline{v}$ O), $\overline{w}$ (×) Vs. height.

Roustan Rhone Sofi

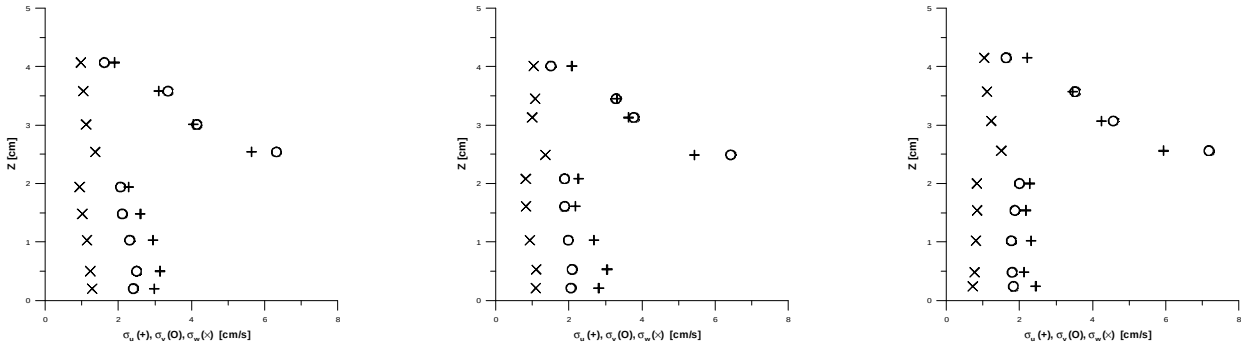

a) b) c)

Figure 6-10 .- Vertical profile of velocity standard deviation above sediment samples. S u (+), S v (O), S w (×) Vs. height.

The profile of the correlation between the instant u and w components of the velocity was also estimated as:

$$c' = \frac{\overline{u'w'}}{u'w'} \tag{6-3}$$

and

$$c'_{u_*} = \frac{\overline{u'w'}}{2u_*} \tag{6-4}$$

where the estimated u_*'s were used (using: (6-5), graphically using (6-6) and (6-7). See section 6.3.1.3 Friction Velocity Determination). In Figure 6-11 a) the c' (6-3) is plotted versus height for the three samples. All the values for c' are negative, and the correlation decreases with height. In Figure 6-11 b) the c' is plotted against the mean velocity. Since the mean velocity in the u direction, $\bar{u}$, increases with height, and from Figure 6-11 a) and Figure 6-9, it was expected that as the velocity increases, the correlation , c', decreased. On the other hand, at a fixed depth, if $\bar{u}$ increases, c' tends to a constant value. For the three samples c' goes constant at about 10 $^{cm}/_{s}$ (Figure 6-12).

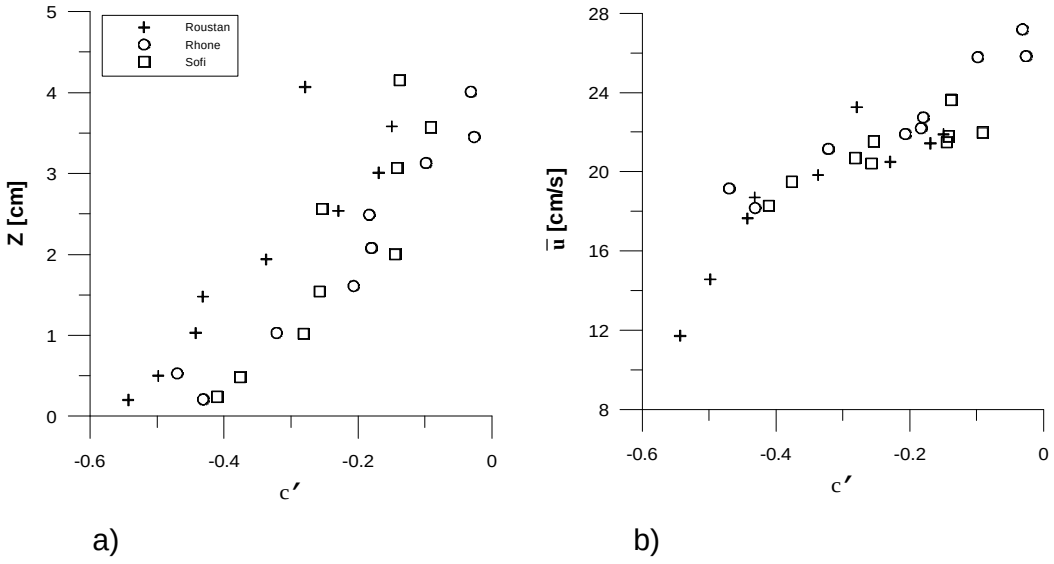

Figure 6-11.- a) c' Vs. height. b) c' Vs. $\bar{u}$. (c' using **(6-3)**).

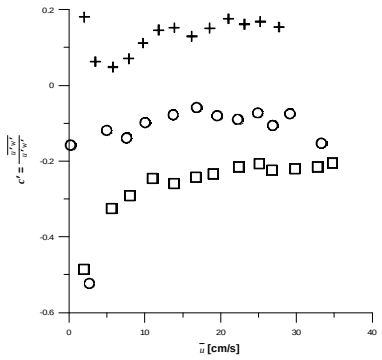

Figure 6-12.- c' Vs. $\bar{u}$ at a depth of 2.79 cm above the bottom (c' using **(6-3)**).

It has previously been noticed that there is a common behaviour in all standard deviation, σ, profiles where at certain height above the bottom an abrupt increase of the standard deviation exists. The behaviour mentioned for the σ is not seen in Figure 6-11, meaning that it does not affects the correlation. When the c'_{u_*} is plotted with height (Figure 6-13 a), b) and c)), two sets of points are also seen. One set below Z = 2 cm, and the other above. In this case the behaviour of the standard deviation affects the

correlation. On the other hand, the values for c'_{u_*} goes beyond the expected range [-1,1] because they are not properly normalized as c' (6-3).

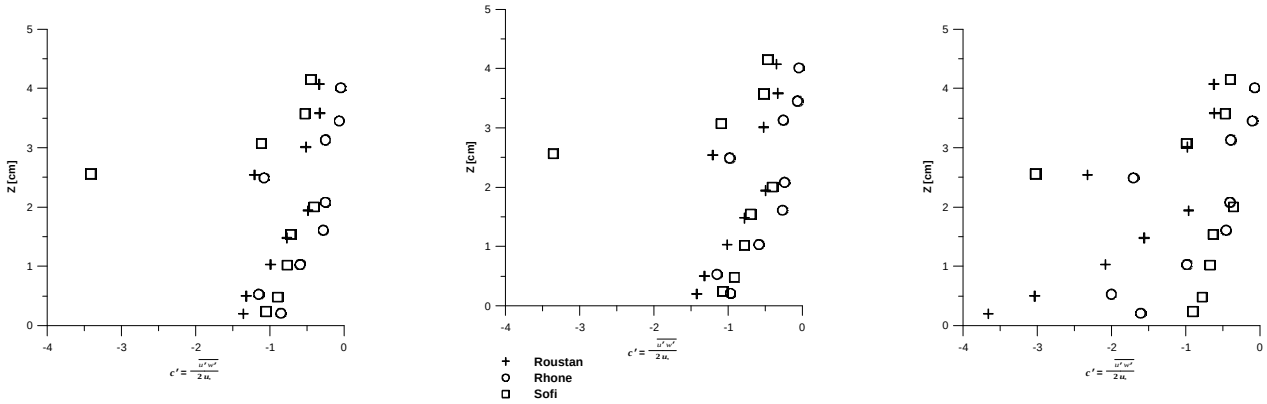

a) b) c)

Figure 6-13.- c'_{u_*} Vs. Z. a) using (6-5); b) using the graphical method, (6-6); c) using Nikuradse's approximation (6-7). a) and b) are practically identical. Both use the graphical method at the beginning to estimate the roughness parameter Z_0.

6.3.1.1.5 Time series above the sediment samples.

A 20 minute time series was measured 0.5 cm above the sediment samples and was compared with the one minute time series at the same height corresponding to the vertical profiles above the sediment samples (Figure 6-9 and Figure 6-10). Results are presented in Table 6-2. No relevant differences were found for the mean velocities nor for the standard deviations.

6.3.1.2 Threshold velocity measurements, particulate matter concentration and particle size distribution measurements.

The experiments in the channel consisted of measuring the velocities at approximately 3 cm above the sediment with an Acoustic Doppler Velocimeter (ADV) with an acquisition frequency of 25 Hz. The data measured with the ADV was used to characterize the flow over the samples. A Meeres-Electronik Gmbh (ME) acoustic currentmeter at 5 Hz was placed downstream of the testing section 4 cm above the

bottom. The measurements of this currentmeter were used together with the particle matter data to describe the evolution in time of the suspended sediment concentration. The water speed was increased from 2 $^{cm}/_{s}$ to 34 $^{cm}/_{s}$ in 13 steps of approximately 2.5 $^{cm}/_{s}$. The time span between speed increments was of 8 minutes, and water samples for particulate matter analyses were taken 2 and 5 minutes after each speed increment was made. Six size classes were recorded: < 2 µm, 2-5 µm, 10-50 µm, 50-100 µm, 100-200 µm.

Table 6-2.- Comparison between 20 minute measurements and 1 minute measurements above sediment samples.

	20 min time series at 0.5 cm above sediment. [$^{cm}/_{s}$]						Equivalent measurement of the vertical profile (Figure 6-9 and Figure 6-10) [cm/s]					
	$\bar{u}$	σ_u	$\bar{v}$	σ_v	$\bar{w}$	σ_w	$\bar{u}$	σ_u	$\bar{v}$	σ_v	$\bar{w}$	σ_w
Roustan	14.11	3.16	1.75	2.52	-0.57	1.27	14.56	2.98	1.32	2.40	-0.60	1.28
Rhone	21.24	2.76	1.95	2.09	-1.69	0.98	19.15	3.04	-2.64	2.08	-0.89	1.10
Sofi	18.38	4.57	0.12	1.68	-0.17	0.69	19.49	2.12	0.01	1.79	-0.01	0.77

In order to determine the threshold velocity, the mean flow velocity at 3.0 cm above the sediment samples is plotted together with the SSC and the particle number against time in Figure 6-14 a), b) and c). These figures show the variation of particle concentration and number as a function of current speed for the different samples. Using the number of suspended particles and the particle concentration as an indicator of the sediment lift-off, the increase of these parameters suggests a minimum critical mean velocity (Uc) between 23 - 26 cm/s for the Roustan sample. This sample shows a second increase of these parameters at about 28 cm/s. For the other two samples the Uc was between 21.6 - 22 cm/s for the Rhone sample and between 18 – 21 cm/s for the Sofi sample.

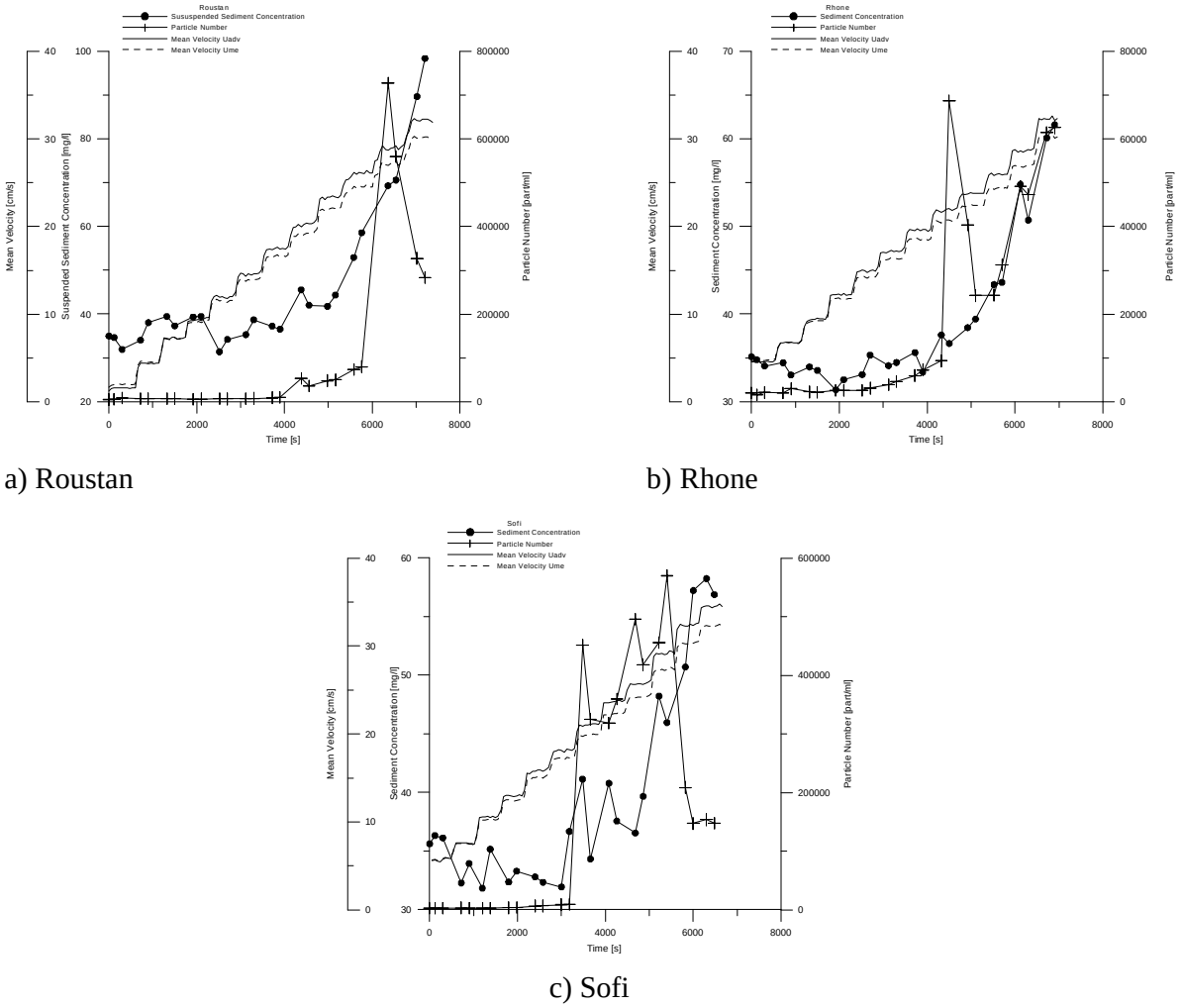

Figure 6-14.- Mean flow velocity at 3.0 cm above the sediment samples is plotted together with the SSC and the particle number against time.

Maximum resuspension rate for the different samples was estimated from the temporal increase of concentration in the tank above the critical speed (Table 6-3). The resuspension rates were higher on the prodelta and mid-shelf (~ 200 g m^{-2} h^{-1}) than on the outer shelf (~ 70 g m^{-2} h^{-1}). The suspended matter was mostly composed of very fine particles (< 2 μm, clay) (Table 6-4).

Table 6-3.- Maximum resuspension rates for the different sites.

Sample	Resuspension rate $\left(\mathrm{gr}/\mathrm{m}^2 h\right)$
Roustan	217
Rhone	84
Sofi	64

Table 6-4.- Grain size distribution of the suspended matter in the tank after resuspension.

	0-2µm * %	**2-5µm **%**	**5-10µm ***%**
Roustan	68.4	24.4	7.2
Rhone	70.0	23.0	7.0
Sofi	77.7	17.8	4.5

* Clay ** Clay-Silt *** Silt

6.3.1.3 Friction Velocity Determination

The break of the logarithmic profile at the upper section of the tank is shown in Figure 6-4 and limits the relevant layer depth to obtain the friction velocity above the Perspex bottom as:

$$u_* = \frac{U}{\left(\frac{1}{k}\right)\ln\frac{z}{z_0}} \tag{6-5}$$

The typical turbulent velocity (friction velocity) at the bottom (u_*) was obtained by different three means (Table 6-5). Using equation (6-5) where k is the Von Karman constant (0.4), graphically from the adjustment made in Figure 6-15 considering that u_*

is the slope of the adjusted line (6-6), and using roughness parameter Z_0 defined as a function of the sediment size (6-7), then

$$u_* = \frac{kU}{\ln(z_0) - \ln(z)} \tag{6-6}$$

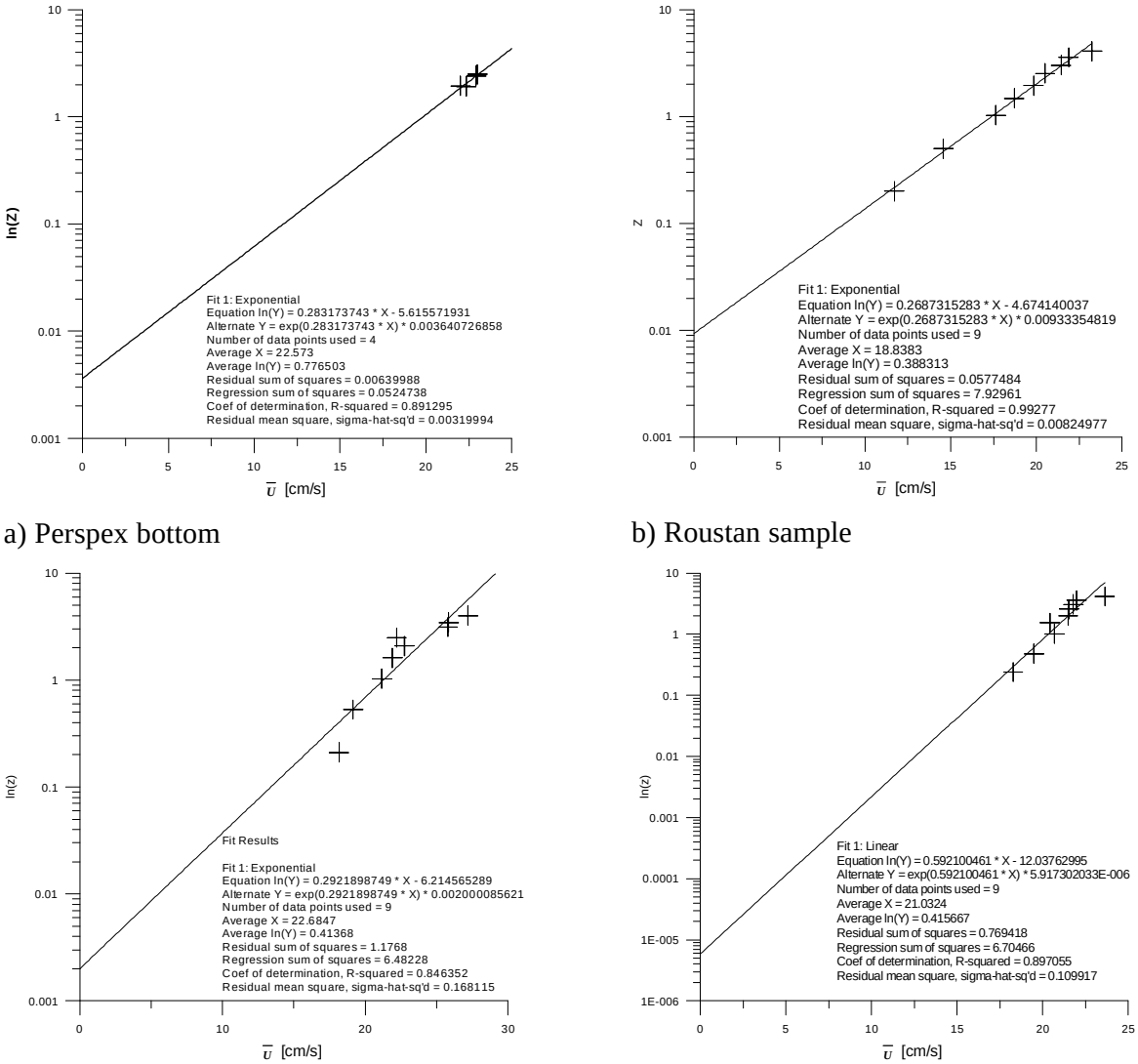

a) Perspex bottom

b) Roustan sample

c) Rhone sample

d) Sofi sample

Figure 6-15.- Graphical method to determine u_*.

For both the smooth Perspex bottom and the sediment cores, it is necessary first to obtain the value for the roughness height, Z_0. This was done by plotting the mean

value of the velocity against the logarithm of the position above the bottom. Only the lower points were used for the Perspex profile. An exponential adjustment was applied to these points, and the Z_0 obtained as the value where the adjusted line crosses the Y axis. Results are shown in Table 6-5.

A third way to estimate u_* was computed using roughness parameter Z_0 defined as a function of the sediment size. Nikuradse in 1933, found that the logarithmic velocity profile over a bed of closely packed spheres of diameter d is zero at

$$z_0 = \frac{1}{30} d \qquad (6\text{-}7)$$

Calculations obtained using Nikuradse's approximation are indicate with a (d) in Table 6-5.

Table 6-5.- Values of Z_0 for u_*.

Sample	Z_0 (1) **cm**	u_* (2) cm/s	$u_* g$ (3) cm/s	Z_0 (d) **cm**	u_* (d) cm/s	$\sigma_{(u/v)}$ (4) cm/s
Perspex Bottom	3.6 x 10^{-3}	1.40	1.54	-------	-------	1.94 / 1.53
Roustan	9.3 x 10^{-3}	1.48	1.46	5.25 x 10^{-5}	0.72	2.81 / 2.05
Rhone	2 x 10^{-3}	1.37	1.37	3.25 x 10^{-5}	0.84	2.44 / 1.83
Sofi	0.006 x 10^{-3}	0.67	0.67	2. 6 x 10^{-5}	0.76	4.57 / 1.68

(1) – using Eq. (6-6)
(2) – using Eq. (6-5)
(3) – graphical method
(4) – at 0.2 cm above bottom (Figure 6-5 and Figure 6-10).
(d) – using Nikuradse's z_0 Eq. (6-7)

We see in Table 6-5 that the standard deviation near the bottom (0.2 cm) tends to a value close to the estimated u_* using equations (6-5), (6-6) and (6-7). The value for the estimated Z_0 using (6-6) for the Perspex bottom does not correspond to the real roughness of Perspex. It is probably reflecting an apparent roughness due to the effect of the adjacent Honey Combs up the flow. The values for u_* using Nikuradse's

approximation is smaller for Roustan and Rhone samples but it is not for Sofi. The respective Z_0 are of the same order of magnitude whereas for the Z_0 estimated with (6-6) three are of the same order (Perspex, Roustan and Rhone) and one is three orders smaller (Sofi). It seems from Table 6-5 that the best approximation between u_* and σ is in general for σ_v. The worst approximation is for the Sofi sample.

6.3.1.4 Velocity fluctuations peak

A peak of velocity fluctuations was measured at a given height above the bottom, as could be seen in the vertical velocity profiles, both above the flat (Perspex) bottom (Figure 6-5) and above the sediment samples (Figure 6-10). In order to explain this high velocity fluctuation region, we first have to state that a possible origin is the existence of a difference in depth before and after the honey comb baffles in the channel (Figure 6-16). The baffles hamper the flow, and produce a layered flow after them. The depth difference related to the hydrostatic pressure gradient was measured for several mean velocities of the flux. Figure 6-16 shows a linear relation between the depth difference before the honey comb baffles and the mean flux velocity.

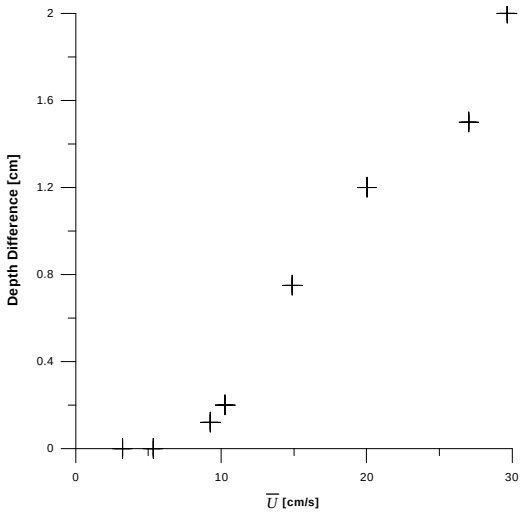

Figure 6-16.- Relation between the depth difference before the honey comb baffles and the mean flux velocity in the u direction.

The mean velocity profile above the Perspex bottom (Figure 6-4) shows some particular characteristics such as a constant velocity layer in the upper part, and a parabolic profile at the bottom. The greatest velocity is present in the lower part of the profile. The configuration is shown in Figure 6-17 as a schematic drawing.

If we consider this flow as a fully developed stage of a steady flow between two infinite parallel plates, where the lower plate is immobile (bottom) and the upper plat moves at uniform speed (the upper constant layer of the flow), and where the flow is driven by a combination of an externally imposed pressure gradient (maintained by the depth difference mentioned before and the pump of the channel) and the motion of the upper plate then, the conditions needed in order to have a vertical velocity profile such as the one shown in Figure 6-4 and Figure 6-17 are (Virto L. 1991, Kundu P 1990):

1.- The height from the bottom to the position of the maximum velocity of u, $Z_{u_{max}}$, is smaller than the distance from the bottom to the upper plate, h.

$$z_{u_{max}} < h$$

2.- The pressure difference between two points at the same height has to be negative, $\frac{\partial P}{\partial x} < 0$

3.- And the downstream pressure gradient has to be larger than the Navier-Stokes equation for plane Couette flow $\left|\frac{\partial P}{\partial x}\right| > \frac{2mU}{h^2}$

Now, in the experimental configuration corresponding to Figure 6-17, $Z_{u_{max}}$ is 1.0 cm while h is 2.6 cm. Then the first condition is satisfied. Regarding the pressure gradients $\left(\frac{\partial P}{\partial x}\right)$ conditions, a depth difference of 1.2 cm was obtained for a mean velocity, U, of 20 $^{cm}/_{s}$, and the typical downstream distance between the two points was of 50 cm. Using these data we obtain:

$$\frac{\partial P}{\partial x} = -497.61 \quad {dyn}/{cm^3}$$

$$\frac{2\mu U}{h^2} = 0.06 \quad dyn/cm^3$$

These values amply satisfy the other two conditions, meaning that the kind of plane Couette flow proposed to explain the measured vertical velocity profile above the flat bottom of the recirculation tank is satisfactory.

Now that the base flow conditions have been described, the peak in the vertical profiles of the standard deviations may also be explained. The recirculation pump does not only force an homogeneous layer at the surface, but also forces a horizontal pressure gradient. There are two layers flowing in the same direction with different speeds. This shear generates more turbulence at this point making the velocity fluctuations higher at height h.

As the flow moves away from the baffles, the mean velocity profiles tend to a logarithmic profile from bottom to top (Figure 6-9) even though the velocity fluctuation peak persists further downstream at the same height as before. The mean velocity profiles measured at the test section show that the two-layer flow is no longer present, but the velocity perturbations due to the upstream shear need a longer distance to decay.

6.3.2 Results of the Experiments with Turbulence with Zero Mean Flow

In this section we present the results obtained from the experiments performed in the grid mixing box and the basic experimental set up values (stroke, mesh, distance from grid to sample). Since Sánchez and Redondo (1998) carried out an extensive work to calibrate the flow generated by a grid of 0.8 mesh like the one used in these experiments in a box of a similar geometry, no additional velocity calibrating measurements where performed. Nevertheless, some calibration was necessary in order to determine the suspended sediment concentration inside the mixing box at any given moment. The results of this calibration are reported.

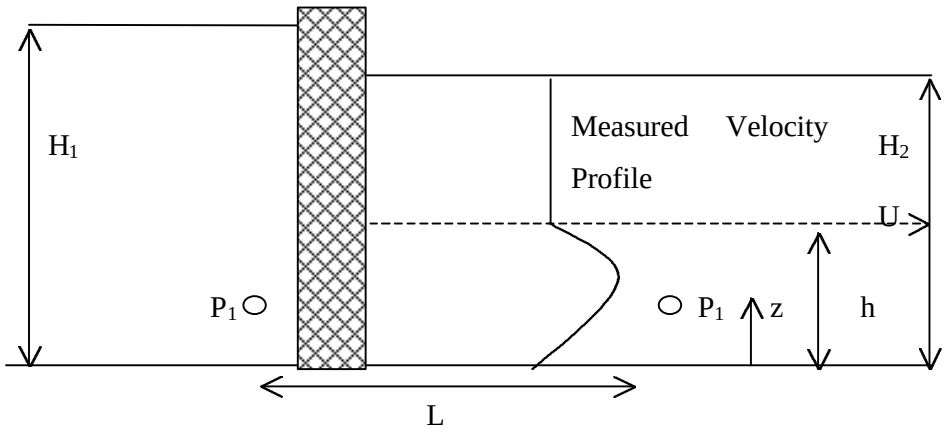

Legend:

P_1= Local pressure before the honey comb baffle, at height z above the bottom. P_2= Local pressure after the honey comb baffle, at height z above the bottom. H_1= Distance between the surface and the bottom before the honey comb baffle. H_2= Distance between the surface and the bottom after the honey comb baffle. Z= Height from the bottom. h= Distance between the bottom and upper layer. U= Mean velocity of the upper layer. L= Distance between P_1 and P_2.

Figure 6-17.- Schematic drawing of the tank configuration to explain the velocity fluctuations peak.

The measurements performed to obtain the suspended sediment concentration at the beginning and at the end of each experiment are presented as well as the values for the corresponding threshold velocity for the early sediment resuspension (ER) and for the main sediment resuspension (MR).

6.3.2.1 Experiment set-up characteristics

There are some basic parameters that are required to calculate the turbulent r.m.s. velocity, u', at the sediment surface or at any distance from the grid's centre of oscillation using equation (6-2). In all experiments the distance from the grid's centre of oscillation to the sample surface, known as height, z, was of 2.95 cm.; the grid stroke, s, was of 1.25 cm. and the grid's mesh (defined as the distance between centres), M, was of 0.8 cm as stated before. The frequency range of oscillation of the grid, w, was gradually increased from 3 Hz to 6 Hz.

6.3.2.2 Critical Turbulent r.m.s. Velocity, u'.

The grid's oscillation frequency was gradually increased starting from the lower possible frequency. In this setup it was 3 Hz. As soon as a sediment lift off was observed the corresponding grid frequency was registered. This frequency was used to estimate the critical turbulent r.m.s. velocity, u', for lift off or threshold velocity for resuspension. For each sample two resuspension events were observed at different values of u'. The first event or early resuspension (ER) was at very low values of u' and of minor suspended sediment concentration rates. The second event or main resuspension (MR) took place when higher values of u' were reached and the corresponding suspended sediment concentration was of greater importance. This second event could be described as an abrupt and strong erosive event.

The values of the corresponding critical turbulent r.m.s. velocity, u', for each event are presented in Table 6-6 as well as the corresponding suspended sediment concentrations. Note that the threshold value of u' for the early resuspension is always lower than 1.35 $^{cm}/_{s}$. This is due to the fact that the lowest possible velocity of this specific experimental setup was higher than the real critical velocity for the early resuspension.

Table 6-6.- Critical turbulent r.m.s. velocity, u'.

Sample	Critical turbulent r.m.s. velocity, u' for ER [$^{cm}/_{s}$]	Sediment Concentration [$^{mg}/_{l}$]	Critical turbulent r.m.s. velocity, u' for MR [$^{cm}/_{s}$]	Sediment Concentration [$^{mg}/_{l}$]
Roustan	<1.35	10.98	2.24	637.48
Rhone	<1.35	18.29	3.67	326.26
Sofi	<1.35	-----	3.67	-----

6.3.2.3 Suspended Sediment Concentration

Subsamples from the cores extracted were used to calibrate the suspended sediment concentration with the light intensity transmitted from the back of the box to the camcorder. These subsamples taken from the cores were also taken from the surface using a 42.4 cm^3 vial. The content of the vessel was dried and desegregated. Small

amounts of sediment weighing between 0.018 g and 0.10 g were kept in different packages. Once this was done, the mixing box used to perform the experiments was filled with a known volume of water and the light characteristics were set up in order to record the calibration process under the same conditions as the experiments.

The initial conditions were considered as 100 % of light transmitted, then the pre-weighed sediment was added. The water in the tank was strongly agitated to get it well mixed and sediment concentration was computed each time sediment was added. A fit was made to these results so the sediment concentration could be estimated for every light intensity value present during the experiments. The result from this fit is shown in Figure 6-18.

The relationship between light transmittance (or light intensity) and the suspended load concentration was obtained using Digimage software. This software has 255 (0 to 254) different values for light intensity. Thus a known amount of suspended sediment load could be assigned to a specific intensity value (e.g. for 100 % transmittance, the value 0 was assigned, and for 0 % the assigned value was 254). The fact that a value of 254 is reached does not mean that a maximum suspended sediment concentration is achieved. The sediment concentration could increase but since the light transmittance is already 0%, if more sediment is suspended no change in transmittance will be noticed.

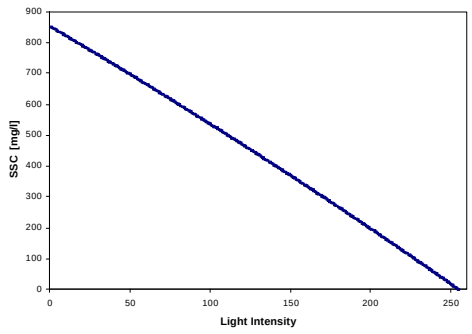

Figure 6-18.- Calibration. Light Intensity Vs. Suspended Sediment Concentration.

In Figure 6-19, an example of sediment resuspension time series is shown. This way the moment of ER and MR could be estimated as well as the SSC at any height and

time (Table 6-6). If the same procedure is followed for the sedimentation process, the mean sedimentation speed could be determined as well as the mean sediment size (Table 6-7).

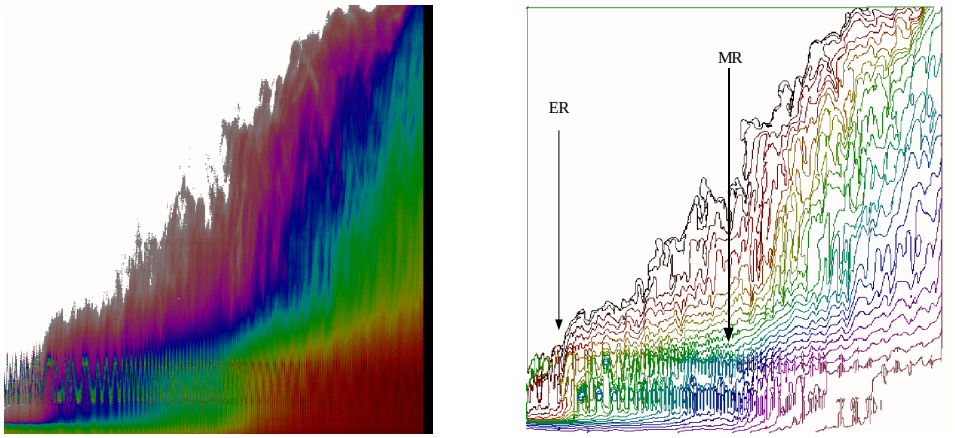

a) b)

Figure 6-19.- An example of time series of sediment resuspension (MR), this corresponds to the Roustan sample. In the vertical axis Z (height) is represented. In the horizontal axis t (time) is represented. Surface of sediment is at the bottom of the image, and the grid position and movement is seen as an oscillatory signal at the bottom of the images. a) Time series as obtained from Digimage Software. b) Contour lines or isolines of light intensity. Light intensity or light transmittance has a direct relation to suspended sediment concentration (Figure 6-18).

Sediment size was estimated considering the mean settling speed measured in the tank with Digimage Analysis software as the falling velocity in suspension, V_s (Allen, 1970) and is defined as

$$V_s = V_0 (1-C)^n \tag{6-8}$$

where V_0 is the free falling velocity of the sphere, C is the volumetric concentration of spheres in the suspension, and n is an exponent varying between 4.6 in the Stokes region and 2.4 where the Reynolds number is large. V_0 is defined as:

$$V_0 = \frac{1}{18} \frac{(r_s - r) g D^2}{m} \tag{6-9}$$

which is Stokes law of settling, where r_s is the density of the sphere, r is the density of the fluid, g is gravity, D is the diameter of the sphere and m is the viscosity of the fluid. Solving for D we obtain

$$D = \sqrt{\frac{V_s}{(1-C)^n}\frac{18m}{(r_s - r)g}} \tag{6-10}$$

Comparing the results obtained for D using (6-10) with the measured mode in Table 6-1, the error could be estimated (Table 6-7) as

$$\text{Size Error (\%)} = \frac{\text{Measured Mode - Image Estimated Size}}{\text{Measured Mode}}\ (100) \tag{6-11}$$

Table 6-7.- Deposition Speed and Image-Estimated Sediment Size.

Sample	Mean Deposition Speed [$^{cm}/_{s}$]	Max. Deposition Speed [$^{cm}/_{s}$]	Min. Deposition Speed [$^{cm}/_{s}$]	Image-Estimated Sediment Size [μm]	Size Error in Percentage [%]
Roustan	0.0154	0.027	0.007	14.52	7.8
Rhone	0.0063	0.015	0.003	9.76	4.8
Sofi	0.0113	0.015	0.006	------	------

6.4 Discussion.

The resuspended sediment in the channel was mostly fine particles (clays), much smaller than the sample mode size (Table 6-1 and Table 6-4). This was because the friction velocities, u_*, reached during the experiments were only strong enough to remove the smaller particles placed on top of the samples, probably particles of recent deposition that hadn't been able to consolidate with the rest of the bed (Møller-Jensen (1993)). This event was similar as the one described in the grid experiments as an early

resuspension ER to distinguish between this and the strong erosive (main resuspension, MR) event where particles of a bigger size and which had been deposited for a longer period of time are lift off from the sample.

In the grid experiments, these particles were resuspended at the very beginning (Table 6-8 and Figure 6-19). The lower u' obtained at the sample surface was higher than the critical needed to generate the early resuspension, this is the reason why the ER value for the all the samples is lower than 1.37 $^{cm}/_{s}$ (Table 6-6 and Table 6-9). For the Roustan sample it is possible to see that the critical turbulent velocity required to resuspend this fraction of the sample is smaller for the grid experiment than for the channel experiment. The same thing could be considered for the Rhone sample, but it is not so clear for the Sofi sample (Table 6-9).

Table 6-8.- Comparative table between the SSC at beginning of the ER and at the end of the experiments.

	Sample	**SSC at ER at the lutocline front** [mg/l]	**Max. SSC reach in experiment at the lutocline front**** [mg/l]
Channel	**Roustan**	34.6	98.3
	Rhone	34.0	61.6
	Sofi	35.6	58.2
Grid	**Roustan**	10.98	637.48
	Rhone	18.29	326.26
	Sofi	**-----**	**-----**

** Value prior to reaching transmittance = 0 in the Grid Experiments.

The MR, generated by the grid experiments, unlike the ER, could be seen as an abrupt event when reaching the critical u'. This resuspension was clearly stronger than the one seen during the channel experiments. This event was able to resuspend a layer of sample in a few seconds and not only the few particles placed on top of it. No SSC measurements were done during the grid experiments. In spite of this, the Image-Estimated sediment size results, confirmed that the achieved u' during the experiments was strong enough to resuspend some of the compacted sediments and not only the smaller particles placed on top of the samples.

The lowest critical u' (2.24 $^{cm}/_{s}$) corresponds to the Roustan sample. The other two samples had similar critical turbulent velocities (3.67 $^{cm}/_{s}$), this value is close to the upper limit imposed by the grid set up. After certain voltage intensity input to the motor, the grid frequency had a tendency to a value near 6.2 Hz., implying that the turbulent velocities had an upper limit near 3.7 $^{cm}/_{s}$.

Table 6-9.- Comparative table between u' and u_* in Grid and Channel.

	Grid		**Channel**			
Sample	u'_{ER} ($^{cm}/_{s}$)	u'_{MR} ($^{cm}/_{s}$)	U_{ER} ($^{cm}/_{s}$)	u_{*ER} ($^{cm}/_{s}$)	**Max. *U* reach** ($^{cm}/_{s}$)	**Max. u_* reach** ($^{cm}/_{s}$)
Roustan	<1.35	2.24	23.3 26.1	1.75	27.7	1.94
Rhone	<1.35	3.67	21.6 22.0	1.2	33.2	1.83
Sofi	<1.35	3.67	18.1 21.0	0.58	34.7	1.06

Computing the mean velocities, U, needed to get the same critical turbulent velocities (u') in the channel as the ones obtained in the grid experiments for MR, it is seen that for the Roustan sample this mean velocity is 31.92 $^{cm}/_{s}$, near the limit reach in the channel experiments. But for the other two samples, the computed velocities are between 2 (Rhone) and 3.5 (Sofi) times higher than the highest value reach during the channel experiments.

The former does not mean that when those mean velocities are reached in the channel, a strong resuspension will take place, probably faster velocities are needed. For example, the critical turbulent velocity needed to induce the early resuspension in the Roustan sample was higher for the channel experiment than for the grid. There is an important difference between the velocity fluctuations at the bottom, expressed as the r.m.s. (u') or as u_* of the different velocity components, of both systems. For the shear flow, the difference among the measured fluctuations of the u component and the w component is 2.4 to 3 times, being larger the u component. Whereas for the grid

experiments, where a fully developed 3D turbulence is present, the fluctuations are about the same in the three directions ($u' \sim v' \sim w'$).

This difference is very likely the reason why it is easier to resuspend the sediment in the grid experiments. In the channel, the unidirectional flow make the pressure gradient over the sediment work in one preferential direction. Whereas under the grid the velocity fluctuations are about the same in the three directions and in a random way meaning no preferential direction of stresses. This hamper the process of particle imbrication (the way particles arrange in presence of an unidirectional flow) making easier to dislocate the particles from the bed.

The size mode of the Roustan sample is the biggest one (Table 6-1), because it is taken from the site closer to the shore and the shallower one. If no cohesive particles were present, this sample would be expected to have the higher critical turbulent velocity. But to explain the differences between the turbulent velocities, u', it is necessary to take into account the percentage of clays in each sample. The Rhone and Sofi samples had the higher percentage of clays (about 32 %), and the Roustan sample the lowest (22 %).

The cohesiveness of the sediment seems to play a more important role than sediment size, hampering the erosion processes that cause sediment lift off from the sediment bed. For the Sofi sample, where the u_* is always lower than for the other samples (Table 6-9) and the estimated $\bar{u}$ for the strong resuspension is the highest of them all, we have to consider that this sample is the one that presented the lower porosity value and the smaller mode size thus making the sample more compact and smoother.

The fact, that the error obtained estimating the sediment size by means of image analysis was so low, shows that this way of analysis has advantages over time demanding traditional methods (e.g. pipette analysis takes more than one day) and expensive ones (e.g. COULTER LS, Enhanced Laser Diffraction Particle Size Analysis). These results deserved further work to corroborate the precision of the method and to establish the sediment size range where it could be use. It will be

necessary to establish the methodology that has to be follow so that it could be used by different researchers in different applications.

Chapter 7

DISCUSSIONS AND CONCLUSIONS

This chapter reviews the main conclusions derived from this work. We shall begin by remembering the main objectives, and then, specifying all the relevant results achieved.

The objectives of the thesis were, on the one hand, to test the possibilities of a well-known experimental configuration used to study stratified fluids in turbulent flows with zero-mean flow, on the study of sediment transport, and to find out what aspects involved in this phenomena could be explored from this new perspective. On the other hand, we also wanted to compare a well-established criterion, such as Shields parameter, with the local turbulent energy (u'), which is an appealing physically relevant parameter, as well as to compare the differences between zero-mean and sheared induced lift-off.

Probably, the most relevant result reached was proving that the experimental configuration used could be employed in further works to investigate different aspects of sediment transport with great accuracy. This experimental configuration, in combination with techniques of image analysis, greatly improves the capabilities of the grid stirred experimental configurations, mainly on the study of sediment behaviour.

Many different experimental configurations can be used. An extensive calibration of the flow prior to any experimental run is the utmost important thing to do. Even though it has been demonstrated that in all the different experimental configurations used during the development of this work, u' could be estimated as $u' = cs^{3/2} M^{1/2} w z^{1/2}$, constant c varies between configurations, even between those apparently equivalent (ie., **5MG-FSE** and **5MG-FSE-FFTA**).

The flow behaviour, between the grid and the free surface, and between the grid and the bottom, is, in general terms, the same. If the grid is too close to a boundary (bottom), a strong secondary flow is generated. In turn, this flow, when passing through the grid, becomes a source of turbulence by itself, and enhances the vortex advection at the side of the grid opposite the boundary. The effect of this secondary source of turbulence on the overall flow behaviour, is that the fully developed turbulence zone is displaced closer to the grid (less than $2\boldsymbol{M}$), and constant c ($u' = cs^{3/2}M^{1/2}\boldsymbol{w}z^{1/2}$) increases.

Other important contributions of the present work are the measurements taken near the boundary. There are no previous works that measure the velocities in a turbulent flow generated by an oscillating grid near the boundary. Other authors (Hunt and Graham (1978)) measure the velocities in a turbulent flow generated by a flow passing through a grid. In that case, the generated vortices were advected parallel to the boundary promoting the vortices anisotropy. In our case, the vortices are advected perpendicular to the boundary. As far as our measurements show, vortices do not distort much before impingement. The former is in accordance with the results of Fernando (1989) (see Chapter 2). After vortex impingement, no constant mean flow is distinguished. The former enhanced the idea that these experimental configurations are suitable for studying the behaviour of a sediment bed under the influence of a turbulent flow.

Turner and Hallworth (1995), together with the above results, supported the assumption that the u' limit at the surface of the sediment bed was equivalent to the friction velocity u_* ($u' \cong u_*$). We observed nevertheless that a smaller magnitude of u'_{cr} than of $u_{*_{cr}}$ was required to start sediment motion (section 5.1.3.1, Figure 5-6), through comparing the theoretical critical friction velocity, $u_{*_{cr}}$ (Critical Shields Parameter), needed to start sediment motion with the measured critical u' for different sediment sizes.

The relation between $u_{*_{cr}}$ and sediment size (in the range studied) is not linear, whereas for the experimental results where u'_{cr} was measured, the relation is linear (section 5.1.3.1, Figure 5-6). This is possibly due to the fact that the u_* value depends

also on the roughness of the sediment bed surface for its development, whereas u' does not.

Other important contribution of the present work is the possibility to research the sediment properties that play a major role in hampering sediment erosion, as it was done in section 5.3. The results obtained from the analysis of the available samples show the importance that the time span between extraction and analysis has on the measured value of u'_{cr}.

The results of the analysis made to the sea bottom samples during the comparison experiments (zero-mean flow Vs. sheared flow), show that cohesiveness of sediment seems to play a more important role than sediment size, hampering the erosion processes that cause sediment lift off from the sediment bed.

If the sediment bed is composed of very fine sediment with low porosity, making the sediment bed compact and smooth, the $\overline{u}$ required to generate a u_* strong enough to lift off the sediment has to be very high, since the u_* depends on the roughness of the sediment bed. Under the same circumstances, a turbulent flow is more efficient eroding the sediment bed, since it does not depend on the roughness of the sediment bed.

The portable experimental configuration proposed in section 4.1.3 is of great help in minimizing the time span between the extraction of a sample and its analysis. As demonstrated in section 5.1.3.2 (Figure 5-8), this time span greatly changes the value of u'_{cr}, and not so much the u'_{cr} value of a second resuspension. This portable configuration could be used on board of any research vessel, enabling us to perform the sediment analysis as soon as the sample is extracted. Thus, the time span extraction-analysis is minimized, as well as sample perturbation by handling and transport procedures.

It is possible to measure sediment velocities during lift-off and settling, using grid stirred experimental configurations in conjunction with image analysis techniques.

It is even possible to determine the sediment size (size mode), even in the range of clays and silts, with an experimental error as small as a 6 or 8 percent.

The fact that the error obtained in the estimate of the sediment size by means of image analysis was so low, shows that this technique of analysis has advantages over time demanding traditional methods (e.g. pipette analysis takes more than one day) and expensive ones (e.g. COULTER LS, Enhanced Laser Diffraction Particle Size Analysis). These results deserve further work to corroborate the precision of the method, and to establish the sediment size range where it can be used. It will be necessary to establish the methodology that has to be followed so that it can be used by different researchers, if precision is corroborated.

Following Sánchez and Redondo (1998), and using grid stirred experimental configurations in conjunction with image analysis techniques, it was possible to quantify the sediment flux at a given turbulence intensity (section 5.2).

When comparing between sheared and zero-mean flow, we found out that great differences exist mainly in the flow capacity to erode the sediment bed. The resuspended sediment in the channel was composed, mostly, of fine particles (clays), much smaller than the sample mode size. This was because the friction velocities u_* reached during the experiments, were only strong enough to remove the smaller particles placed on top of the samples, probably particles of recent deposition that hadn't been able to consolidate with the rest of the bed (Møller-Jensen (1993)). This event was similar to the one described in the zero-mean experiments as an early resuspension ER, to distinguish between this and the strong erosive (main resuspension, MR) event, where particles of a bigger size which had been deposited for a longer period of time were lifted off from the sample.

In zero-mean experiments, these particles were resuspended at the very beginning. The lower u' obtained at the sample surface was higher than the critical u'_{cr} needed to generate the early resuspension. The critical turbulent velocity required to resuspend this fraction of the sample is smaller for the zero-mean experiments than for the sheared experiments.

The MR, generated by the zero-mean experiments, unlike the ER, could be seen as an abrupt event when reaching the critical u'. This resuspension was clearly stronger than the one seen during the sheared experiments. This event was able to resuspend a layer of sample in a few seconds, and not only the few particles placed on top of it. The image-estimated sediment size results, confirmed that the achieved u' during the zero-mean experiments was strong enough to resuspend the compacted sediments and not only the smaller particles placed on top of the samples.

Computing the mean velocities, *U*, needed to get the same critical turbulent velocities (u') in the sheared experiments as the ones obtained in the zero-mean experiments for MR, we can see that for the Roustan sample this mean velocity is 31.92 $^{cm}/_{s}$, near the limit reached in the sheared experiments. But for the other two samples, the computed velocities were between 2 (Rhone) and 3.5 (Sofi) times higher than the highest value reached during the sheared experiments. The former does not mean that when those mean velocities are reached in the sheared experiments, a strong resuspension will take place, probably faster velocities are needed. (ie., the critical turbulent velocity needed to induce the early resuspension in the Roustan sample was higher for the sheared experiments than for the zero-mean experiments).

There is an important difference between the velocity fluctuations at the bottom, expressed as the r.m.s. (u') or as u_* of the different velocity components, of both systems. For the shear flow, the difference among the measured fluctuations of the u component and the w component is 2.4 to 3 times, the u component being larger. Whereas, for the grid experiments where a fully developed 3D turbulence is present, fluctuations are about the same in the three directions ($u' \sim v' \sim w'$).

This difference is very likely the reason why it is easier to resuspend the sediment in the zero-mean experiments. In the sheared experiments, the unidirectional flow makes the pressure gradient over the sediment work in one preferential direction. Whereas, under the grid, the velocity fluctuations are about the same in the three directions and in a random way, meaning no preferential direction of stresses. The former hampers the process of particle imbrication (the way particles arrange in the

presence of an unidirectional flow) making it easier to dislocate the particles from the bed. This is also the reason why after vortex impingement, no constant flow is distinguished above the boundary (sediment bed; section 4.2 **SBE**).

Future work derived from this thesis would include a spatial characterization of u'_{cr} values for areas subject to sediment transport. A full analysis of the consolidation time and the role of biological activity in the stability at a sediment bed are still at large.

ACKNOWLEDGEMENTS

A special recognition is given to the director of this thesis Dr. José M. Redondo and to other colleagues working in the Fluids Dynamic Laboratory, specially, Alejandro Carrillo, Miguel A. Sánchez, Arthur Schraven, Otman Ben Mahjoub and Maria O. Bezerra for there invaluable help during the development of the present work.

A special recognition is given to the Mexican National Science and Technology Council (Consejo Nacional de Ciencia y Tecnología, **CONACyT**), due to the scholarship granted to the author.

This work has been funded in part by the European Community under programme MAST 3 in project METROMED, MAS3-CT96-0049, and MAS3-CT95-0016 (DGE: UE95-0016). The C.N.R.C. the CICIT Network XDFTG are also thank for support that aided this research.

The collaboration and help of Dr. X. de Madron and E. Shaaff in the experiments described in Chapter 6 is greatly appreciated.

Other special recognition is given to all the members of the Maritime Engineering Laboratory (Laboratorio de Ingeniería Marítima, LIM), and of the Applied Physics Departament (Departamento de Física Aplicada) within the Catalonian University of Technology (Universidad Politécnica de Cataluña, UPC).

REFERENCES

Allen, J.R.L., (1970). **Physical Processes of Sedimentation. George Allen & Unwin, London.**

Bagnold, R.A., (1956). **The flow of cohesionless grains in fluids. Phil Trans Roy Soc Lond, No. 964, Vol. 149, pp 235-297.**

Barnett, P.R.O., Watson J., Connelly D., (1984). **A multiple corer for taking virtually undisturbed samples from shelf, bathyal and abyssal sediments. Oceanologica Acta 7 : 399-408**

Basset, A.B., (1888). **On the motion of a sphere in a viscous fluid. Phil Trans Roy Soc Lond, Ser A, Vol 179, pp 43-63.**

Batchelor, G.K., (1953). **The theory of homogeneous turbulence. Cambridge University Press, London.**

Cao, Z., (1997). **Turbulent bursting-based sediment entrainment function. J. Hydraulic Engineering, Vol. 123, No. 3, pp 233-236.**

Cole, B.E., Thompson, J.K., Cloern, J.E., (1992). **Measurement of filtration rates by infaunal bivalves in a recirculating flume, Mar. Biol. 113, pp. 219-225.**

Crespo, D. and Redondo, J.M., (1989). **A simple experiment on the interaction between gravity currents and sediment transport. Rev. Geofisica, 45, pp 203-210.**

Dalziel, S.B., (1993). **Rayleigh-Taylor instability: Experiments with image analysis. Dyn. of Atmospheres and Oceans, 20, pp.127-153.**

Engelund, F. and Hansen, E., (1972). **A monograph on sediment transport in alluvial streams. Teknisk Forlag, Copenhagen.**

Fernando, H.J.S., (1991). **Turbulent mixing in stratified fluids. Annu. Rev. Fluid Mech., 23, pp 455-493.**

Folk, R.L., (1968). **Petrology of sedimentary rocks. Hemphill's, Drawer M. University Station. Austin, Texas.**

Gibbs, R.J., Mathews, M.D. and Link, D.A., (1971). **The relationship between sphere size and settling velocity. J. Sed. Petrology, Vol 41, pp 7-18.**

Hanes, D.M. and Inman, D.L., (1985). **A dymanic yield criterion for granular-fluid flows. J. Geophys. Res., Vol 90, No B5, 3670-3674.**

Hopfinger, E.J. and Toly, J.A. (1976). **Spatially decaying turbulence and its relation to mixing across density interfaces. J. Fluid Mech., vol. 78, part 1, pp. 155-175**

Hunt, J.C.R. and Graham, J.M.R., (1978). **Free-stream turbulence near plane boundaries. J. Fluid. Mech., Vol. 84, part 2, pp 209-235.**

Huppert, H.E., Turner, J.S. and Hallworth, M.A., (1995). **Sedimentation and entrainment in dens layers of suspended particles stirred by an oscillated grid. J. Fluid Mech. vol. 289, pp. 263-293.**

Jones, S.E., Jago, C.F. and Simpson, J.H., (1996). **"Modeling Suspended Sediment Dynamics in Tidally Sirred and Periodically Stratified Waters: Progress and Pitfalls". Mixing in Estuaries and Coastal Seas. Coastal and Estuarine Studies Volume 50, Pag. 302-324. American Geophysical Union.**

Kundu, P., (1990). **Fluid Mechanics. Academic Press, Inc.**

Linden, P.F., (1973). **The interaction of vortex rings with a sharp density interface: a model for turbulent entrainment. J. Fluid Mech., 60, pp 467-480.**

Madsen, O.S. and Grant, W.D. (1976). **Sediment transport in the coastal envionment. Report No209, Palph M Parsons Lab, MIT.**

Magnus, G., (1853). **Poggendorfs annale der physik und chemie, Vol 88, No 1.**

Mann, J., Ott, S. and Andersen, J. S., (1999). **Experimental study of relative, turbulent diffusion. Technical Report Risø-R-1036(EN), Risø National Laboratory.**

Matas, J. and Redondo, J.M., (2000). **Some observations of entrainment in grid stirred stratified flows. Advances in Turbulence. Redondo J.M. and A. Babiano (eds).**

Medina, P., Sánchez, M.A. and Redondo, J.M., (2001). **Grid stirred turbulence: Applications to the initiation of sediment motion and lift-off studies. Phys. Chem. Earth (B). Vol. 26, No. 4, pp 299-304.**

Middleton, G.V., (1966). **Experiments on density and turbidity currents. Canadian Journal of Earth Siences, Vol 3, pp 523-547.**

Møller-Jensen, P., (1993). **Wadden Sea Mud. Methods for estimation of transport, erosion and consolidation of marine cohesive sediments. Centertrykkeriet, Aalborg University. Department of Civil Engineering.**

Nielsen, P., (1979). **Some basic concepts of wave sediment transport. Ser. Paper 20, Inst Hydrodyn. Hydraul. Eng. Tech Univ. Denmark, 160pp.**

Nielsen, P., (1992). **Coastal bottom boundary layers and sediment transport. World Scientific Publishing Co. Pte. Ltd.. Singapore.**

Noh, Y. and Fernando, H.J.S., (1991). **Dispersion of suspended particles in turbulent flow. Phys. Fluids A, vol. 3, No. 7, pp 1730-1739.**

Nortek AS, (2000). Nortek ADV Manuals.

Nowell, A.R.M., Jumars, P.A., (1987). **Flumes: theoretical and experimental considerations for simulation of benthic environments, Oceanogr. Mar. Biol. Ann. Rev. 25 (1987) 91-112.**

Ott, S. and Mann, J., (2000). **An experimental investigation of the relative, turbulent diffusion of particle pairs in three dimensional turbulent flow. Under consideration for publication in J. Fluid Mech. (Receive 9th June 2000).**

Peters, F. and Redondo, J.M. (1997). **Turbulent generation and measurement: application to studies on plankton. Lectures on Plankton and Turbulence, C. Marrasé, E Saiz and J.M. Redondo (eds). Scientia Marina, 61(Supl. 1): 205-228.**

Redondo, J. M., Sánchez, M.A., (1999). **Laboratory measurements of sediment lift-off threshholds and vertical fluxes in the Gulf of Lyons. Advances in Turbulence. Editors Redondo J.M. and A. Babiano.**

Redondo, J. M., Sánchez, M.A., (2000). **Laboratory measurements of sediment lift-off threshholds and vertical fluxes in the Gulf of Lyons. Advances in Turbulence. Redondo J.M. and A. Babiano (eds).**

Redondo, J.M., (1987). **Difusión turbulenta en fluidos estratificados. Ph.D. Thesis, University of Barcelona.**

Redondo, J.M., Sánchez, M.A., Castilla, R., (1995). **Lift Off and Entrainment of Sediments.- Coastal Dynamics '95. Proceedings of the International Conference on Coastal Research in Terms of Large Scale Experiments (1995, Gdansk, Poland). Edited by William R. Dally and Ryszard B. Zeidler.**

Rouse, H. and Dodu, J., (1955). **Turbulent diffusion across a density discontinuity. La Houille Blanch 10, pp. 314-321.**

Sánchez, M.A. and Redondo, J.M., (1998). **Observations from grid stirred turbulence. Applied Scientific Research 59: 243-254.**

Schraven, A., (2001). **Comparing ADV and visual measurements. Technical Report. UPC-Erasmus. Barcelona**

Shaaff, E., (1999). **Remise en suspension des sédiments du Golfe du Lion: Expériences et modélisation. D.E.A. Sciences de l'Environnement Marin. Université de la Méditerranée. U.F.R. Sciences.**

Shields, A., (1936). **Anwendung der Aehnlichkeitsmechanik und Turbulenzforchung auf die Geschiebebewegung. Mitt Preuss Versuchsanstalt fur Wasserbau und Schiffbau, No 26. Berlin.**

Silvester, R. and Hsu, J.R.C., (1993). **Coastal stabilization: Innovative concepts. Prentice Hall , Inc., Englewood Cliffs, New Jersey.**

Swart, D.H., (1974). **Offshore sediment transport and equilibrium beach profiles. Delft Hydr. Lab. Publ., No 131.**

Tennnekes, H. and Lumley, J.L., (1990). **A first course in turbulence. The MIT Press. U.S.A.**

Thompson, S.M. and Turner, J.S., (1975). **Mixing across an interface due to turbulence generated by an oscillating grid. J. Fluid Mech., vol. 67, part 2, pp. 349-368.**

Thorpe, (1966). **Internal gravity waves. PhD Thesis Cambridge University.**

Tsai, C. H. and Lick, W. (1986). **A portable device for measuring sediment resuspension. J. Great Lakes Res. 12(4) 314 - 321.**

Turner, J.S., (1968). **The influence of molecular diffusivity on turbulent entrainment across a density interface. J. Fluid Mech., vol. 33, part4, pp. 639-656**

Turner, J.S., (1973). **Buoyancy Effects in Fluids. Cambridge University Press.**

Virto, L., (1991). **Mecánica de Fluids. Fonaments I. Edicions Universitat Politechinca Catalunya.**

Xuequan, E. and Hopfinger, E.J., (1987). **Stratification by solid particle suspensions. Proc. IUTAM symposium. USC USA. pp. 1-8.**